Structure and Dynamics of highly charged colloidal suspensions

Dissertation
zur Erlangung des Doktorgrades
des Department Physik
der Universität Hamburg

vorgelegt von

Fabian Westermeier

aus Bremen

Hamburg
2010

Gutachter der Dissertation:
Prof. Dr. W. Wurth
Prof. Dr. G. Nägele

Gutachter der Disputation:
Prof. Dr. W. Wurth
Dr. G. Grübel

Datum der Disputation:
6. Dezember 2010

Vorsitzender des Prüfungsausschusses:
Priv.-Doz. Dr. M. Martins

Vorsitzender des Promotionsausschusses:
Prof. Dr. J. Bartels

Leiterin des Departments Physik:
Prof. Dr. D. Pfannkuche

Dekan Fakultät für Mathematik,
Informatik und Naturwissenschaften:
Prof. Dr. H. Graener

Abstract

Two colloidal model systems consisting of highly-charged poly-acrylate particles of low polydispersity and two different particle radii were synthesized. Their static (time-averaged) and dynamic behavior was studied for a broad range of particle concentrations and added electrolyte by scattering methods using either visible light or X-rays.

The static behavior revealed increasing direct particle interactions with increasing particle concentration. The direct particle interactions were decreasing with increasing electrolyte concentration, as expected for an enhanced screening of the direct particle interactions, thus allowing a tuning of the direct particle interactions from strongly interacting towards strongly screened systems. The extracted static structure factors were in good agreement with the rescaled mean spherical approximation (RMSA), which describes the interparticle interactions in terms of a screened Coulomb potential.

The characterization of the dynamics of the samples allowed the determination of the normalized inverse diffusion coefficient $D_0/D(Q)$, which indicated a slowing down of particle dynamics on length scales corresponding to the next neighbor distance. The short-time self diffusion coefficient $D^{\mathrm{s,short}}$ is decreasing with increasing particle concentration. Furthermore $D_0/D(Q) \neq S(Q)$ as expected for the presence of hydrodynamic interactions. The collective short-time diffusion coefficient D_C indicated enhanced collective dynamics with increasing direct interparticle interactions.

The peak values of the hydrodynamic functions $H(Q_{max})$ were found to be within the theoretical limits given on the one hand by the hydrodynamic behavior of a hard sphere system and on the other hand by the theoretical maximum of the hydrodynamic functions for a charge-stabilized system within the $\delta\gamma$-expansion. For small volume fractions ($\phi < 0.02$), $H(Q_{max})$ is larger than unity and decreasing with decreasing direct particle interactions. The hydrodynamic functions of these samples are well described within the pairwise additive approximation, which takes into account only two particle stationary hydrodynamic interactions. For samples of volume fraction $\phi > 0.06$ the maximum of the hydrodynamic function was smaller than unity. This slowing down of the particle dynamics was more pronounced in more concentrated systems. At the highest concentration $\phi \approx 0.33$ the hydrodynamic functions are well characterized by the $\delta\gamma$-expansion (originally developed for hard-sphere systems) using the measured static properties as input. In the intermediate concentration range $0.06 \leq \phi \leq 0.18$ a quantitative description of the hydrodynamic functions was achieved by the small-Q approximation of the $\delta\gamma$-expansion. The

hydrodynamic functions showed an enhanced mobility in this intermediate volume fraction range when compared to hard-sphere theory.

Zusammenfassung

Das statische und dynamische Verhalten von zwei kolloidalen Modellsystemen bestehend aus hochgeladenen Polyacrylat-Kolloidteilchen dispergiert in Wasser wurde mittels Streuung von sichtbarem Licht und Röntgenstrahlung als Funktion der Kolloid- und Salzkonzentration untersucht.

Die statischen (zeitgemittelten) Messungen zeigten mit zunehmender Konzentration der kolloidalen Teilchen eine Zunahme der direkten Partikelwechselwirkungen (höhere $S(Q)$ Werte). Weiterhin wurde beobachtet, dass die direkte Wechselwirkung wie erwartet mit steigender Salzkonzentration abnimmt. Dies zeigt, dass mittels kontrollierter Zugabe von Salz die direkte Wechselwirkung zwischen den Partikeln gezielt eingestellt werden kann. Die gemessenen statischen Strukturfaktoren konnten durch die Rescaled Mean Spherical Approximation (RMSA), die direkte Wechselwirkungen der Teilchen mittels eines abgeschirmten Coulomb Potentials beschreibt, gut angepasst werden.

Die dynamischen Messungen erlaubten eine Bestimmung des dynamischen Strukturfaktors $D_0/D(Q)$, der eine verlangsamte Dynamik auf genau den Längenskalen zeigte, die dem mittleren Abstand der kolloidalen Teilchen entspricht. Der Kurzzeit-Selbstdiffusionskoeffizient $D^{\mathrm{s,short}}$ nimmt mit zunehmender Partikelkonzentration ab. Weiterhin weicht der dynamische Strukturfaktor $D_0/D(Q)$ vom statischen Strukturfaktor $S(Q)$ ab, was auf die Existenz hydrodynamischer Wechselwirkungen hinweist. Der kollektive Kurzzeitdiffusions-Koeffizient D_C zeigte eine Zunahme der kollektiven Dynamik mit zunehmender direkter Wechselwirkung.

Die Maximalwerte der extrahierten hydrodynamischen Funktionen $H(Q_{max})$ lagen zwischen den theoretisch erwarteten Werten eines Hart-Kugel-Systems einerseits und eines elektrostatisch wechselwirkenden Systems andererseits. Für kleine Volumenbrüche ($\phi < 0.02$) war $H(Q_{max}) > 1$ und nahm mit zunehmender Abschirmung der direkten Wechselwirkungen ab. Die hydrodynamischen Funktionen dieser Proben konnten innerhalb der Pairwise Additive Approximation, die nur Zweikörperwechselwirkungen in Betracht zieht, beschrieben werden. Das Maximum der hydrodynamischen Funktionen $H(Q_{max})$ der Proben höheren Volumenbruchs ($\phi > 0.06$) war kleiner als 1. Mit steigender Kolloidkonzentration wurde eine geringere Dynamik beobachtet. Die hydrodynamischen Funktionen der Proben mit den höchsten Kolloidkonzentrationen $\phi \approx 0.33$ konnten innerhalb der $\delta\gamma$-Expansion, mit den gemessenen Probenparametern als Eingabeparameter, gut beschrieben werden. Die Probensysteme im mittleren Konzentrationsbereich $0.06 \leq \phi \leq 0.18$ konnten innerhalb der Small-Q Approximation der $\delta\gamma$-Expansion beschrieben wer-

den. Hier zeigen die kolloidalen Teilchen eine im Vergleich zum Hart-Kugelfall erhöhte Mobilität.

Contents

1. Introduction

Colloidal systems have been a field of increasing scientific activity in both, fundamental and applied research during the last decades. Colloidal systems consist out of particles with typical length scales from a few nanometers up to a millimeter which are finely dispersed in a homogeneous molecular phase. These systems have a broad appearance in daily live - micellar liquids such as milk, sun lotion with fine particles that scatter or absorb ultraviolet light or paints where small dissolved particles stick to a surface after the evaporation of the solvent are well known examples. Here the continuous improvement of the products is the aim of applied research. Even a living cell with it's thousands of proteins, nucleotide strands and different cellular compartments can be seen as a colloidal system - a system which is, although heavily studied and of great biological and medical interest, still far from being understood.

The availability of well characterized colloidal model systems has been one of the driving forces for fundamental research during the last decades. Due to their mesoscopic length scales and the associated time scales, colloidal systems are often easier accessible by a variety of experimental methods than atomic or molecular systems. A particularity of colloidal systems is their interparticle interactions, which allow self organization of the colloidal particles and the formation of fluid-like, glassy or crystalline structures. Furthermore, the strength of the interparticle interactions can be experimentally varied, allowing one to investigate systems in a wide range from virtually none interacting systems to systems with very strong interparticle correlations. The structures can be highly symmetric and can therefore be seen as model systems for condensed matter physics. In 1991 the French physicist Pierre-Gilles de Gennes received the Nobel price in physics for his work in the field of condensed matter, especially on his research on ordering phenomena in simple systems such as colloidal suspensions and their generalization towards more complex systems (de Gennes, 1979).

An important aspect of colloidal suspensions is the dynamics of the system. As the particles are small and in the ideal case stabilized against aggregation, the motion of a colloidal system is nearly solely driven by the thermal excitation of the suspension. While the particles are diffusing freely in the case of strongly diluted colloidal suspensions, the dynamics are affected by the presence and the interactions of other particles in more concentrated systems. Besides the influence of direct particle interactions on the motion of the particles, hydrodynamic interactions are affecting the dynamics of the particles. These indirect interactions, which are mediated by the solvent, are generated by the motions of the particles in the suspension and can be regarded as acting instantaneously on all colloidal particles present. Due to the many-body character of the hydrodynamic interactions, the theoretical description and experimental evaluation is complicated and controversially discussed in literature especially in the case of colloidal particles interacting via a long-range interaction potential. For these systems, a *speeding up* (Härtl *et al.*, 1999) as well as a *slowing down* (Grübel *et al.*, 2000) of the particle dynamics due to hydrodynamic interactions has been reported.

The aim of this thesis work is the synthesis and subsequent analysis of the structure, the dynamics and hydrodynamic interactions of a colloidal system interacting via a long-range interaction potential. Of particular interest are the static and dynamic properties as a function of the strength of the direct particle interaction potential for a broad range of concentrations ranging from dilute to strongly concentrated systems.

The static and the dynamic behavior of colloidal systems can be experimentally accessed by scattering methods. These experimental techniques offer the advantage to probe an ensemble of colloidal particles in the scattering volume. In the case of dilute to moderately concentrated suspensions, the scattering experiments can be performed with visible light. In the case of more concentrated suspensions, which are often optically opaque to visible light, the scattering experiments can be conducted with X-rays which in addition offer the capability to probe the systems on smaller length scales when compared to visible light. Here the availability of partially coherent X-rays from third generation synchrotron sources offers the possibility not only to perform static, but also dynamic measurements on mesoscopic systems of high turbidity. Such experiments have been performed in the framework of this thesis.

The outline of the thesis is as follows

Chapter 2 gives an introduction into the world of *Colloidal Systems* treating their stabilization and resulting interactions including the structure and dynamical behavior of nano-particles suspended in a fluid.

In chapter 3 *Scattering Theory* and its application to colloidal systems is introduced. In addition models describing the static and dynamic behavior of colloidal systems are explained.

Chapter 4 describes the *Experimental Techniques* and methods used to get insight into the behavior of colloidal systems.

The outcome of the performed scattering experiments applied to colloidal suspensions is presented in Chapter 5 *Experimental Results and Discussion*, together with a discussion of the results.

Chapter 6 comprises a *Summary and Outlook* of the work.

2. Colloidal Systems

2.1. Interparticle forces

Colloidal systems have attracted increasing scientific, but also economic attention during the last 30 years. The main characteristics of a colloidal system is their mesoscopic nature: The typical length scale of a colloidal system ranges from a few nanometers to a micrometer and is therefore situated between atomic systems and macroscopic systems. This mesoscopic nature offers the advantage that it can be probed by methods not applicable to atomic systems and that it can be often described within the framework of classical physics.

A colloidal system is made out of two different phases - a dispersed phase, which is evenly distributed in a second phase, the dispersion medium. Both phases can be of different or of the same state of matter, so that typical natural colloidal systems include fog (small water droplets in air), milk (micelles made out of amphiphilic molecules dispersed in water) or ink (small pigments in a solvent). The colloidal systems of particular interest for this work are made out of small solid state particles dispersed in a fluid dispersion medium.

For the theoretical description of a colloidal system often a coarse-grained viewpoint is used, in which the liquid dispersion medium is considered as an inert continuum defined by its macroscopic properties. The colloidal particles dispersed in this continuum interact with each other, and their hydrodynamic properties are formally the same as those of an assembly of atoms making it possible to use colloidal particles as a model system for atomic systems to study phenomena such as structuring or the phase behavior on mesoscopic length scales.

A particular characteristic of a colloidal system are the interparticle interactions, which permit self-organization of the colloidal particles and the formation of fluid-like or crystalline structures. Regarding the complex multi-component colloidal dispersions as a one component system of particles in which only the interparticle potentials are required is justified by the solution theory (William G. McMillan and Mayer, 1945; Kirkwood and Buff, 1951) and leads to the potential of mean force $U(\boldsymbol{r}^N)$, which depends on the center-of-mass positions of all particles in a suspension of N colloidal particles $\boldsymbol{r}^N = (\boldsymbol{r}_1, \boldsymbol{r}_2, \ldots, \boldsymbol{r}_N)$. It is usually assumed that the potential of mean force is the sum of the pair potentials between two particles $V(\boldsymbol{r}_j - \boldsymbol{r}_i)$, which, in the case of spherical particles, are spherically symmetric. The effective pair potential V is the sum of the attractive and repulsive forces acting on the particle.

The van-der-Waals force is an attractive force between bodies caused by interactions between the fluctuating electromagnetic fields. Between two spherical particles of radius R and a center-to-center distance r the resulting potential is given by

$$V_A(r) = -\frac{H}{6}\left[\frac{2R^2}{r^2 - 4R^2} + \frac{2R^2}{r^2} + \ln\left(1 - \frac{4R^2}{r^2}\right)\right]. \tag{2.1}$$

The Hamaker constant H is depending on material properties of the colloidal particles and the suspending fluid, in particular on their polarisability. If the attractive van-der-Waals force would be the only acting force in a colloidal system, the nano-particles would irreversibly aggregate over time. Therefore the colloidal particles have to be stabilized against agglomeration, which can be achieved by introducing a repelling force. This can be achieved in two different ways - either by steric stabilization or by electrostatic stabilization.

2.1.1. Steric stabilization

Sterically stabilized colloidal particles have a surface which is covered by polymer molecules, which may be chemically bonded or physically absorbed on the surface of the nano-particles. In the simplest case these polymers are alkyl chains, but they can also consist of more complex structures. If two colloidal particles come close two each other, the interpenetrating polymers are compressed leading to a repulsive force between the particles. The effective pair potential of two particles at contact distance is infinite, while it is vanishing fast with increasing particle distance and can be therefore approximated by

$$V_{HS}(r) = \begin{cases} \infty & r \leq 2R \\ 0 & r > 2R. \end{cases} \tag{2.2}$$

Due to this short-range interaction potential such systems are called hard-sphere systems, as illustrated in fig. 2.1.

The short-range nature of the particle interactions in a hard sphere system leads to an universal phase behavior of hard spheres which is only depending on the volume fraction ϕ of the colloidal particles, given by

$$\phi = \frac{4}{3}\pi R^3 n \tag{2.3}$$

where n is the number density of colloidal particles. Below a volume fraction of $\phi = 0.494$ the system is liquid, while the system is fully crystalline above a volume fraction of $\phi = 0.545$ (Hoover and Ree, 1968). Between these two limits a coexistence of poly-crystalline and fluid phases can be observed (Pusey and van Megen, 1986). Moreover, above a volume fraction of $\phi \approx 0.58$, hard sphere systems may form a glassy state.

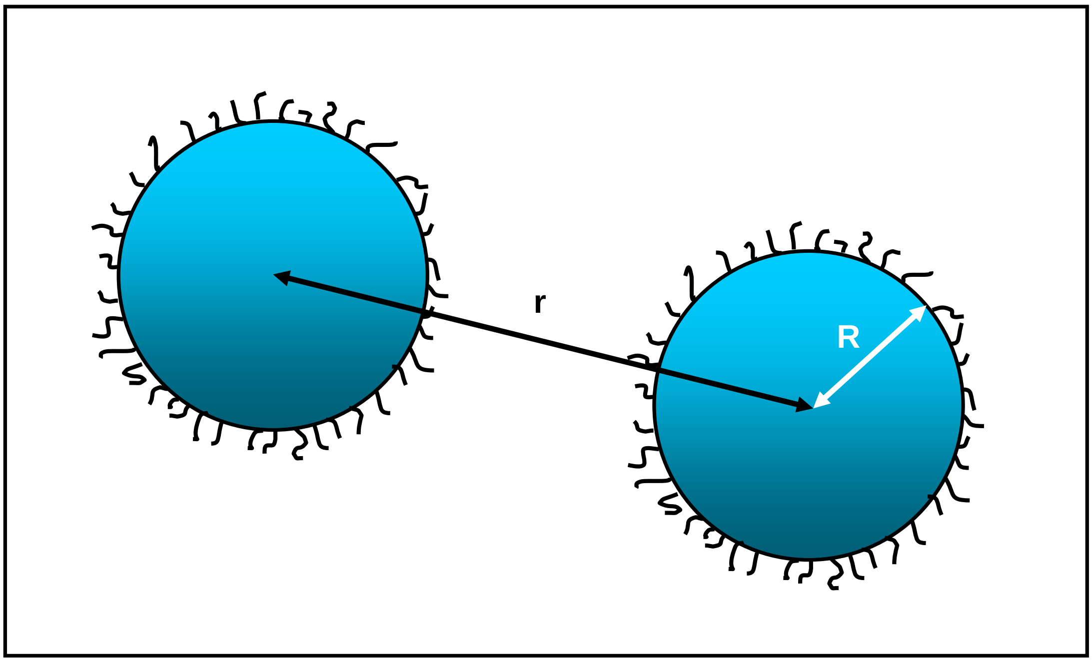

Figure 2.1.: Schematic drawing of a sterically stabilized (hard sphere) system. R is the radius of the colloidal particles and r is the interparticle distance.

Already in the liquid state, at colloidal particle concentrations below the transition to a crystalline state, the particles start to get ordered. This ordering can be described by the radial distribution function $g(r)$, which is described in more detail in section 2.2.

2.1.2. Electrostatic stabilization

In an electrostatically stabilized system the colloidal nanoparticles carry ionisable groups on their surface. At least some of these groups dissociate in a polar solvent such as water, resulting in charged colloidal nanoparticles which can be regarded as *macroions*. The dissociated counter ions released into the dispersion medium remain in the field of force of the colloidal particle and form an *ionic cloud* around the particle, resulting in an electrical double layer. The overlap of these electrical double layers surrounding two colloidal nanoparticles approaching each other is causing a repelling force, which leads to a stabilization of the colloidal system. A sketch of an electrostatical stabilized system can be seen in fig. 2.2.

A detailed description of the electric double layer is given by the Derjaguin-Landau-Verwey-Overbeek (DLVO) theory (Verwey and Overbeek, 1948). The small counter ions, regarded as point charges, move rapidly enough due to Brownian motion that their average spatial distribution can be assumed to be the equilibrium Boltzmann distribution. The resulting Poisson-Boltzmann equation is linearized

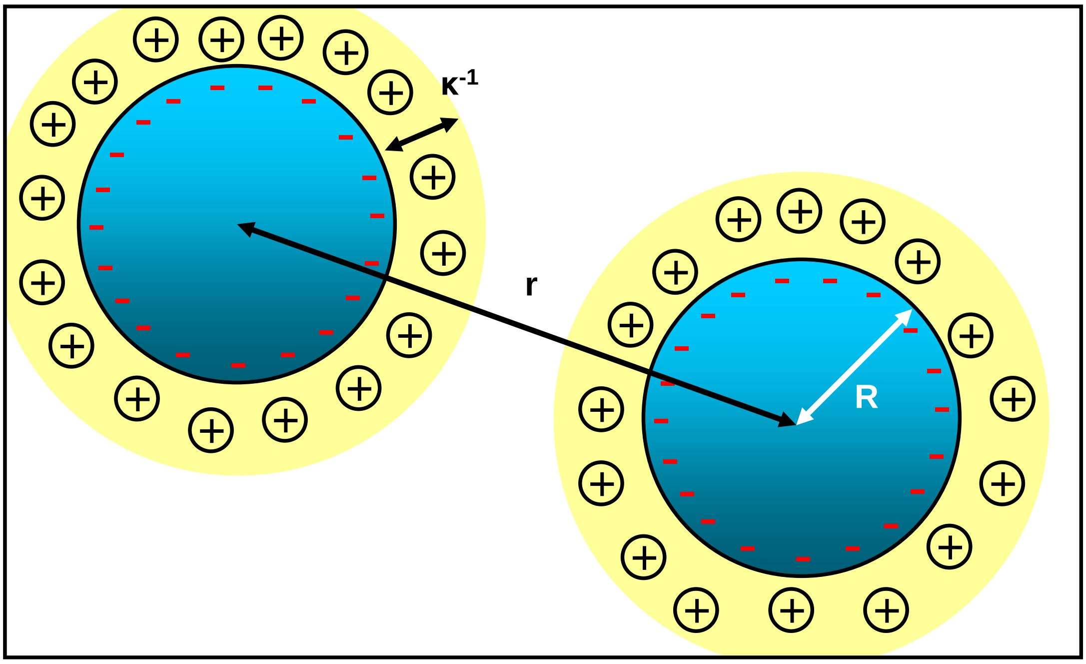

Figure 2.2.: Schematic drawing of an electrostatically stabilized colloidal system including counter ions. r is the interparticle distance, R is the radius of the particles and κ^{-1} is the Debye-Hückel screening length.

according to the theory of Debye and Hückel (Hückel, 1925) for simple electrolytes. The approach leads to the DLVO expression for the interactions of two isolated macroions suspended in a bath of electrolyte and can be described by a screened Coulomb (*Yukawa*) potential (Nägele, 1996)

$$\frac{V_{CS}}{k_B T}(r) = \begin{cases} \infty & r \leq 2R \\ \frac{e_0^2 Z_{\text{eff}}^2}{\epsilon k_B T} \left(\frac{\exp(\kappa R)}{1+\kappa R}\right)^2 \frac{\exp(-\kappa r)}{r} & r > 2R. \end{cases} \tag{2.4}$$

Here k_B is the Boltzmann constant, T is the absolute temperature, e_0 is the elementary charge, Z_{eff} is effective charge of the colloidal nanoparticle and r is the distance between two colloidal particles of radius R. The permittivity of the suspending medium $\epsilon = \epsilon_0 \epsilon_r$ is given by the permittivity of vacuum ϵ_0 and the dimensionless relative permittivity of the medium ϵ_r.

The parameter κ is the inverse of the Debye-Hückel screening length which is depending on the total amount of charges present in the colloidal solution and is described by

$$\kappa^2 = \frac{4\pi e_0^2 2 N_A}{\epsilon k_B T} I \frac{1}{1-\phi}. \tag{2.5}$$

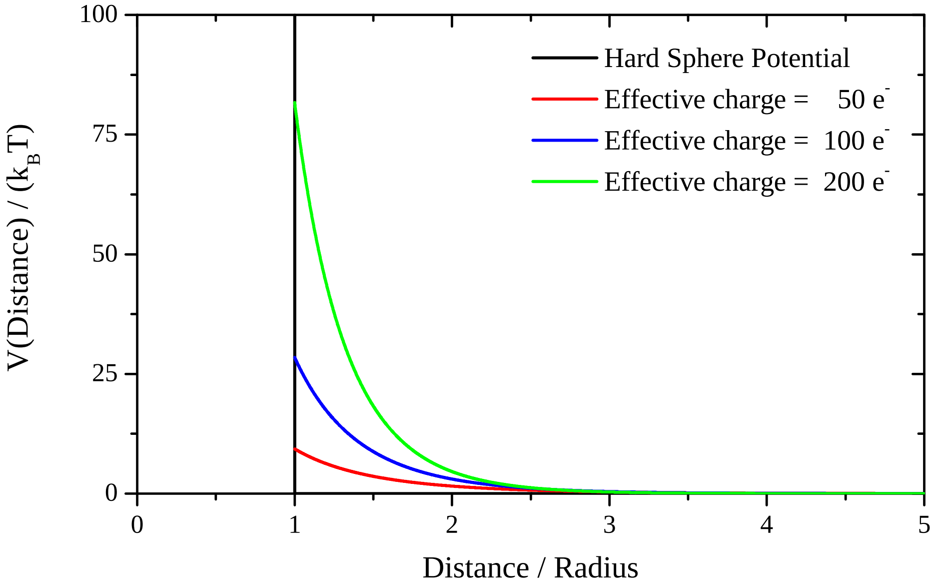

Figure 2.3.: Particle interaction potential as a function of the normalized interparticle distance (distance/particle radius). The black line shows the interaction potential of a sterically stabilized system, the red, blue and green lines show the interaction potential of electrostatically stabilized colloidal particles in a deionized medium with an effective charge Z_{eff} of 50, 100 and 200 e^{-} respectively. The volume fraction for all colloidal systems is $\phi = 0.1$ and the relative permittivity of the dispersion medium $\epsilon_r = 80.1$.

Here ϕ is the volume fraction of colloidal particles and N_A is the Avogadro constant. I is the ionic strength of the suspending medium and is given by

$$I = \frac{1}{2} \sum_j c_j q_j^2 \tag{2.6}$$

where c_j is the concentration of ions j having a charge of q_j. Thus the ionic strength of the medium is depending both on the amount of counter-ions released by the macroions and the concentration of additionally added electrolyte increasing the ionic strength of the suspending fluid.

The Yukawa potential is long-range in the $\kappa R \rightarrow 0$ limit and the particles of the system are strongly interacting with each other, even in a dilute suspension. In the $\kappa R \rightarrow \infty$ limit the particle interactions are becoming increasingly screened and the system is adopting hard sphere properties. The particle interactions of a hard sphere system and three electrostatically screened systems with increasing effective charge Z_{eff} at the same concentration and no additional electrolyte present in the solution are shown in fig. 2.3. As can be seen in the graph, the interaction potential is increasing with increasing effective charge Z_{eff} and is long-range, especially when compared to the hard-sphere case.

The effective charge Z_{eff} of the colloidal particles is depending on the number of ionisable groups on the surface of the colloidal particles and the dispersion medium, and is thus not identical to the absolute number of ionisable surface groups.

As the interactions of an electrostatically stabilized system are long-range, the phase behavior of such systems is not only depending on the volume fraction ϕ of the colloidal particles but also on the strength of the interaction potential. Therefore the liquid-solid transition can occur already at much smaller concentrations as compared to a hard sphere system (Robbins *et al.*, 1988).

2.2. Static behavior of colloidal systems

In an ensemble of N particles the correlations between two particles at a distance r is usually described by means of the pair distribution function $g(r)$. For completely uncorrelated systems, the pair distribution function of spherical particles $g(r) = 1$ at distances $r > R$. With increasing ordering of the system, the value of $g(r)$ starts to deviate from unity. In a fluid or glassy systems, where short-range ordering of the particles can be observed, the pair distribution function is converging to unity for large distances. In crystalline systems with long-range ordering of the system, the pair correlation function is always different from unity.

If the system is made out of spherical particles, the pair correlation function is just depending on the modulus of the distance vector of two particles $|\boldsymbol{r}| = |\boldsymbol{r_i} - \boldsymbol{r_j}| = r$. If the positions $\mathbf{r^i}$ of all N particles of the ensemble in a volume V are known, the pair correlation function can be written as the mean value

$$g(r) = \frac{1}{n^2} \left\langle \left(\sum_{\substack{i,j=1 \\ i \neq j}}^{N} \right) \frac{1}{V} \delta(\boldsymbol{r} - \boldsymbol{r^i} + \boldsymbol{r^j}) \right\rangle \tag{2.7}$$

where $n = N/V$. The pair correlation function $g(r)$ describes thus the relative conditional probability of finding a particle a distance r apart from another particle. The average number of particles which can be found in a spherical shell of the width dr and a distance r around a particle located at its center is given by $4\pi r^2 n g(r) \mathrm{d}r$.

2.3. Dynamics of colloidal systems

2.3.1. Free diffusion

In a colloidal system, the nanoparticles are dispersed in a solvent consisting of small molecules. Due to the thermal energy inherent to the system at a temperature above absolute zero, these small molecules are moving constantly in a diffusive, random fashion. By collisions with the mesoscopic colloidal particles these particles are also moving in a stochastic way, they perform a random walk in three dimensions. These movements, which have first been described by Brown on pollen moving in water, are called after their discoverer "Brownian" motion. As the time to cover a certain distance by Brownian motion is proportional to the square of the distance, it is an important way of transport in microscopic to mesoscopic systems while on longer distances other means of transport such as convection are more important.

When the interactions between neighboring particles are small compared to the thermal energy of the system, the particle is able to move freely in the surrounding fluid which can be regarded as a thermal bath for the colloidal particles. The translation of the particle can be described by the free diffusion coefficient, which is depending on the thermal energy of the system and the mobility μ of the particles and is given by the Einstein–Smoluchowski relation

$$D_0 = \mu k_B T. \tag{2.8}$$

The mobility $\mu = v/F$ is the ratio of the particles drift velocity to an applied force. In a fluid the friction force F of a spherical particle of the radius R and the velocity v moving in fluid of the viscosity η is after Stokes

$$F = 6\pi\eta R v. \tag{2.9}$$

The free diffusion coefficient D_0 of a spherical particle is thus given by the Stokes-Einstein relation

$$D_0 = \frac{k_B T}{6\pi\eta R}. \tag{2.10}$$

On very short time-scales, the colloidal particles can be seen to be essentially stationary. The motion of the particles can be described in this regime as a random ballistic flight. The Brownian relaxation time τ_B is the typical relaxation time of the particle velocity due to solvent friction given by (Nägele, 1996)

$$\tau_B = \frac{m}{\zeta} \tag{2.11}$$

where m is the mass of the colloidal particle and $\zeta = 6\pi\eta R$ is the friction coefficient. For colloidal particles the Brownian relaxation time τ_B is typical in the order of $10^{-10} - 10^{-8}$ s (Pusey, 1991). The mean-square displacement of a free diffusing particle is given by (Berne and Pecora, 1976)

$$\langle [r_i(0) - r_i(t)]^2 \rangle = 6D_0 t, \qquad t \gg \tau_B \tag{2.12}$$

where the particle motion is just influenced by collisions with the solvent molecules.

2.3.2. Diffusion of interacting colloidal particles

In an ensemble of interacting colloidal particles, the motion of the colloidal particles are influenced not only by collisions with solvent molecules, but also by the presence of other colloidal particles. Two additional factors are thus influencing the particles motion: On the one hand the direct particle interactions, which induce *drift* velocities in the particles, and on the other hand hydrodynamic interactions, which are transmitted through the suspending medium and couple both Brownian motions and drift velocities between the particles.

On short time intervals, the mean-square displacement of the particles is small, thus that the structure of the ensemble of colloidal particles in the system has essentially not changed. The direct interaction forces experienced by one particle can hence be assumed to be constant. The structural relaxation time τ_R is a measure of the time of a perceptible change of the configuration of particles due to many-body diffusion and is given by

$$\tau_R = \frac{R^2}{D_0}. \tag{2.13}$$

The structural relaxation time τ_R is the time in which a spherical particle is moving a distance roughly equal to its radius R. For typical colloidal suspensions, this time interval is usually in the order of $10^{-4} - 10^{-2}$ s.

On time intervals between the structural relaxation time and the Brownian relaxation time, where the configuration of the particles has nearly not changed, the mean square displacement of a particle is given by the short-time self diffusion coefficient $D^{\mathrm{s,short}}$

$$\langle [r_i(0) - r_i(t)]^2 \rangle = 6D^{\mathrm{s,short}} t, \qquad \tau_R \gg t \gg \tau_B. \tag{2.14}$$

On time scales $t \approx \tau_R$ the motion of the particles becomes retarded due to the direct and indirect interactions with the other particles of the system. On longer time scales, where the particles have experienced many direct and indirect interactions during their random walk, the mean square displacement yields the long-time self diffusion coefficient $D^{\mathrm{s,long}}$

$$\langle [r_i(0) - r_i(t)]^2 \rangle = 6D^{\mathrm{s,long}} t, \qquad t \gg \tau_R. \tag{2.15}$$

Typically, in suspensions of interacting spheres, the long-time self diffusion coefficient $D^{\mathrm{s,long}}$ is smaller than the short-time self diffusion coefficient $D^{\mathrm{s,short}}$, which can be attributed to the hindrance of the particle motions by direct forces (Nägele, 1996). This thesis will concentrate on the short-time dynamics.

Neglecting indirect hydrodynamic interactions, the second component which contributes to the particles motion are the direct particle interactions inducing a velocity drift of the particles. The interaction component to the velocity is given by

$$v_{In}(t) = \frac{F_{I,i}(t)}{\zeta} \tag{2.16}$$

where $F_{I,i}$ is the interaction force effecting the particle i. For small time intervals Δt, which are larger than the Brownian relaxation time τ_B but smaller than the structural relaxation time τ_R the location of the particle ensemble has essentially not changed thus that $F_{I,i}(t) \approx F_{I,i}(0)$. The displacement of a particle $\Delta r_i(\Delta t)$ is then given by

$$\Delta r_i(\Delta t) = \Delta r_{B,i}(\Delta t) + \frac{1}{\zeta} F_{I,i}(0)\Delta t, \qquad \tau_R \gg \Delta t \gg \tau_B. \tag{2.17}$$

$\Delta r_{B,i}(t)$ is the displacement due to Brownian motion of the particles. The equation describes the dynamics of a suspension of interacting spheres neglecting hydrodynamic interactions where the moments and the positions of solvent molecules do not appear explicitly. The effect of the suspending medium is to generate Brownian motion and to provide friction.

Apart from the direct interactions, the presence of the suspending medium leads to additional hydrodynamic interactions. A particle moving in the surrounding medium will create a velocity field in the medium due to the coupling of the velocity of the fluid to the velocity of the particle at the particles surface. The resulting indirect hydrodynamic interactions between the particles can physically be interpreted as shear waves traveling throughout the suspension and can be assumed to act instantaneously throughout the colloidal system at times $t \gg \tau_S \approx 10^{-12}\,\mathrm{s}$ where τ_S is the mean collision time of solvent molecules (Nägele, 1996). The displacement of a particle is then given by (Ermak and McCammon, 1978)

$$\Delta r_i(\Delta t) = \Delta r_{B,i}(\Delta t) + \sum_{j=1}^{3N} \left[-\frac{1}{k_B T} D_{ij}[\boldsymbol{r}^N(0)] \frac{\partial U[\boldsymbol{r}^N(0)]}{\partial r_j} + \frac{\partial D_{ij}[\boldsymbol{r}^N(0)]}{\partial r_j} \right] \Delta t \tag{2.18}$$

where $D_{ij}[\boldsymbol{r}^N(t)]$ is the configuration-dependent diffusion tensor with symmetry property $D_{ij} = D_{ji}$ and r^N denotes the spatial configuration of N particles. The dynamics of a particle is thus depending on the overall configuration and motions of the system.

2.4. Model system

For the analysis of the direct and indirect interactions of colloidal particles a model system was required - as the particles should be investigated both by visible and X-ray scattering methods, the particles should fulfill the following characteristics:

- High monodispersity
- High surface charge allowing to tune the particle interactions
- Good scattering properties for visible as well as X-ray scattering methods

The model system of choice is a polymer-system made out of functionalized poly-methyl methacrylate, where the sidegroups of the poly-methyl methacrylate backbone of the polymer contain elements of higher electron density than the polymer backbone to enhance the scattering intensity in X-ray scattering experiments.

3. Scattering Methods

3.1. Scattering introduction

If light, an electromagnetic wave, is impinging on a sample with a spatially inhomogeneous refractive index or electron density, such as a random assembly of colloidal particles suspended in a fluid, it is scattered by these inhomogeneities, which can lead to a change of the direction of propagation (or of the momentum) of the incident wave. Depending on whether or not the energy of the scattered light changes during the scattering process, it can be differentiated between elastic and inelastic scattering. In the following just the elastic or quasi-elastic case, where the energy of the scattered light is not or just changed marginally, will be discussed. A typical scattering process is sketched in fig. 3.1. An electromagnetic wave is impinging on a sample and subsequently scattered. The scattered light is detected under a chosen scattering angle θ relative to the incident beam.

The incoming electric field E_i is given by

$$E_i(\boldsymbol{r},t) = \boldsymbol{n_i} E_0 \exp(i[\boldsymbol{k_i} \cdot \boldsymbol{r} - \omega_i \cdot t]) \tag{3.1}$$

where E_0 is the amplitude of the electric field, $\boldsymbol{n_i}$ is the polarization and ω_i the frequency of the incoming wave. The wave vector $\boldsymbol{k_i}$ is inversely proportional to the wave length λ_i of the incoming wave with the modulus

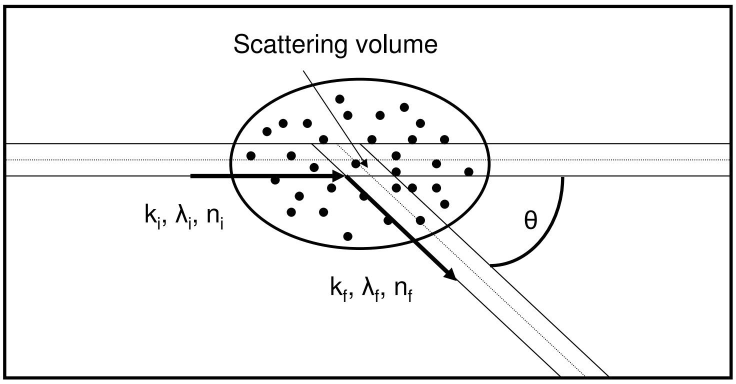

Figure 3.1.: Schematic sketch of a scattering experiment.

$$|\boldsymbol{k_i}| = \frac{2\pi n}{\lambda_i} \tag{3.2}$$

where $n = c_0/c$ is the index of refraction of the medium. The modulus of the momentum transfer **Q** is given by

$$|\boldsymbol{Q}| = |\boldsymbol{k_i} - \boldsymbol{k_f}|. \tag{3.3}$$

Here $\boldsymbol{k_i}$ and $\boldsymbol{k_f}$ are the wave vectors of the incoming (index $i = incoming$) and the scattered (index $f = final$) light. In an elastic scattering process $|\boldsymbol{k_i}| = |\boldsymbol{k_f}|$. The momentum transfer can thus be calculated depending on the scattering geometry

$$\begin{aligned} |\boldsymbol{Q}^2| = |\boldsymbol{k_i} - \boldsymbol{k_f}|^2 = \boldsymbol{k_i}^2 + \boldsymbol{k_f}^2 - 2\boldsymbol{k_i}\boldsymbol{k_f} \\ = 2\boldsymbol{k_i}^2 - 2\boldsymbol{k_i}^2\cos(\theta/2) = 4\boldsymbol{k_i}^2\sin^2(\theta/2) \end{aligned} \tag{3.4}$$

$$Q = \frac{4\pi n}{\lambda_i} \cdot \sin\frac{\theta}{2}. \tag{3.5}$$

3.2. Static scattering

If an electro-magnetic wave is scattered by N scatterers, the amplitude of the scattered wave can be seen as a superposition of the concentric waves originating from the N scatterers. In the far-field, where the resulting wave is essentially a flat wavefront, the instantaneous amplitude $E(\mathbf{Q}, t)$ of the field of the scattered light may be described by

$$E(\boldsymbol{Q}, t) = E_0 \sum_{i=1}^{N} a_i(\boldsymbol{Q}) \exp(i\boldsymbol{Q}\boldsymbol{r_i} - i\omega t). \tag{3.6}$$

Here $a_i(\boldsymbol{Q})$ is the scattering amplitude of the ith scatterer at the position $\boldsymbol{r}_i$ and ω is the frequency of the scattered light. The scattered intensity $I(\boldsymbol{Q}, t)$ at a given point in the far-field can be written as the square modulus of the scattered field $E(\boldsymbol{Q}, t)$

$$I(\boldsymbol{Q}, t) = |E(\boldsymbol{Q}, t)|^2 \tag{3.7}$$

and is given in the temporal average by

$$\langle I(\boldsymbol{Q})\rangle = E_0^2 \sum_{i=1}^{N}\sum_{j=1}^{N} \langle a_i(\boldsymbol{Q}) a_j(\boldsymbol{Q}) \exp(i\boldsymbol{Q}[\boldsymbol{r_i} - \boldsymbol{r_j}])\rangle. \tag{3.8}$$

In the case of identical scatterers the equation can be simplified to

$$\langle I(\boldsymbol{Q})\rangle = E_0^2 N^2 [a(\boldsymbol{Q})]^2 \sum_{i=1}^{N}\sum_{j=1}^{N} \langle \exp(i\boldsymbol{Q}[\boldsymbol{r_i} - \boldsymbol{r_j}])\rangle. \tag{3.9}$$

3.2.1. Scattering of a single particle

From eq. (3.9) the scattering intensity of a single particle can be derived, given by

$$\langle I(\boldsymbol{Q})\rangle = |E(\boldsymbol{Q})|^2 = |a(\boldsymbol{Q})|^2 = a(\boldsymbol{Q}) \cdot a^*(\boldsymbol{Q}) \tag{3.10}$$

where a^* is the complex conjugate of a. The scattering amplitude $a(\boldsymbol{Q})$ is the Fourier transform of the electron charge density $\rho(\mathbf{r})$

$$a(\mathbf{Q}) = \int d\boldsymbol{r}\rho(\boldsymbol{r})\exp(i\boldsymbol{Q}\boldsymbol{r}). \tag{3.11}$$

If the scatterer is a homogeneous sphere with radius R and an uniform electron density contrast $\Delta\rho$, the charge density $\rho(\boldsymbol{r})$ is given by

$$\rho(\mathbf{r}) = \begin{cases} \Delta\rho, & \|\mathbf{r}\| \leq R \\ 0, & \|\mathbf{r}\| > R. \end{cases} \tag{3.12}$$

If the electron charge density $\rho(\boldsymbol{r})$ is inserted in eq. (3.11) and a Fourier Bessel transformation is performed, the scattered intensity of a single sphere of volume V is derived

$$I(\boldsymbol{Q}) = 9(\Delta\rho)^2 V^2 \left(\frac{\sin(QR) - QR\cos(QR)}{(QR)^2}\right)^2. \tag{3.13}$$

The normalized scattered intensity is referred to as the single particle formfactor $P(Q)$, given by (Pusey, 1991):

$$P(\boldsymbol{Q}) = P(Q) = \frac{I(\boldsymbol{Q})}{I(\boldsymbol{0})} = \left[\frac{a(\boldsymbol{Q})}{a(\boldsymbol{0})}\right]^2 = 9\left[\frac{\sin(QR) - QR\cos(QR)}{(QR)^3}\right]^2. \tag{3.14}$$

For large momentum transfers $QR \gg 1$, known as the Porod regime, $P(Q)$ falls off $\sim Q^{-4}$.

In fig. 3.2 the single particle form factor of a spherical particle as a function of the normalized momentum transfer QR is shown. The position of the consecutive maxima and minima are characteristic for the size of the particle and the first minimum can be found at approximately $QR \approx 4.49$.

3.2.2. Scattering of an ensemble of polydisperse spherical particles

For colloidal suspensions made out of many nano-particles, the size of each particle may be slightly different. The effect of the polydispersity can be taken into account by assuming an appropriate size distribution $f(R)$ for the ensemble of particles, which describes the relative frequency of a given size. The polydispersity of a colloidal

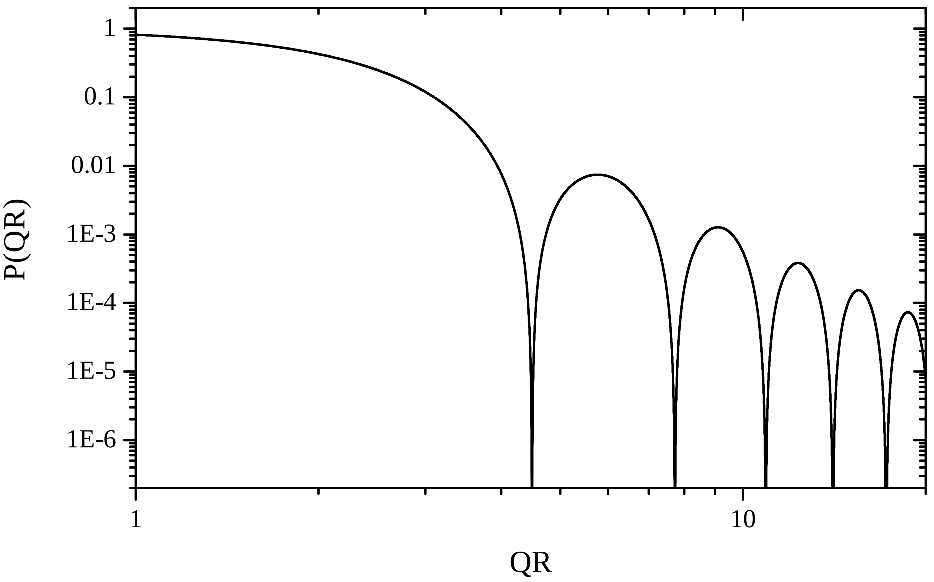

Figure 3.2.: Particle form factor $P(QR)$ of a single spherical particle as a function of QR.

suspension can then be described by means of the average size R_0 and the width ΔR of the size distribution. For colloidal suspensions, the *Schulz-Flory* distribution is often used

$$f(R,R_0,Z) = \frac{1}{(Z+1)!}\left(\frac{Z+1}{R_0}\right)^{Z+1} R^Z \exp\left(-\frac{Z+1}{R_0}R\right) \tag{3.15}$$

where R_0 denotes the number averaged size of the particles. The polydispersity P of the colloidal system can be obtained via

$$P = \frac{\Delta R}{R_0} = \sqrt{\frac{1}{Z+1}}. \tag{3.16}$$

By employing this size distribution, weighted by $(R/R_0)^6$, with a single particle spherical form factor an average polydisperse form factor can be obtained

$$P(\mathbf{Q}) = \int_0^\infty \mathrm{d}R\, f(R,R_0,Z)\, P(\mathbf{Q}R)\left(\frac{R}{R_0}\right)^6. \tag{3.17}$$

The intensity of X-rays scattered by N particles of electron density contrast $\Delta\rho$ is

$$I(\mathbf{Q}) = 9N(\Delta\rho)^2 V^2 P(\mathbf{Q}) \tag{3.18}$$

where $V = \frac{4}{3}\pi R_0^3$ is the volume of a sphere.

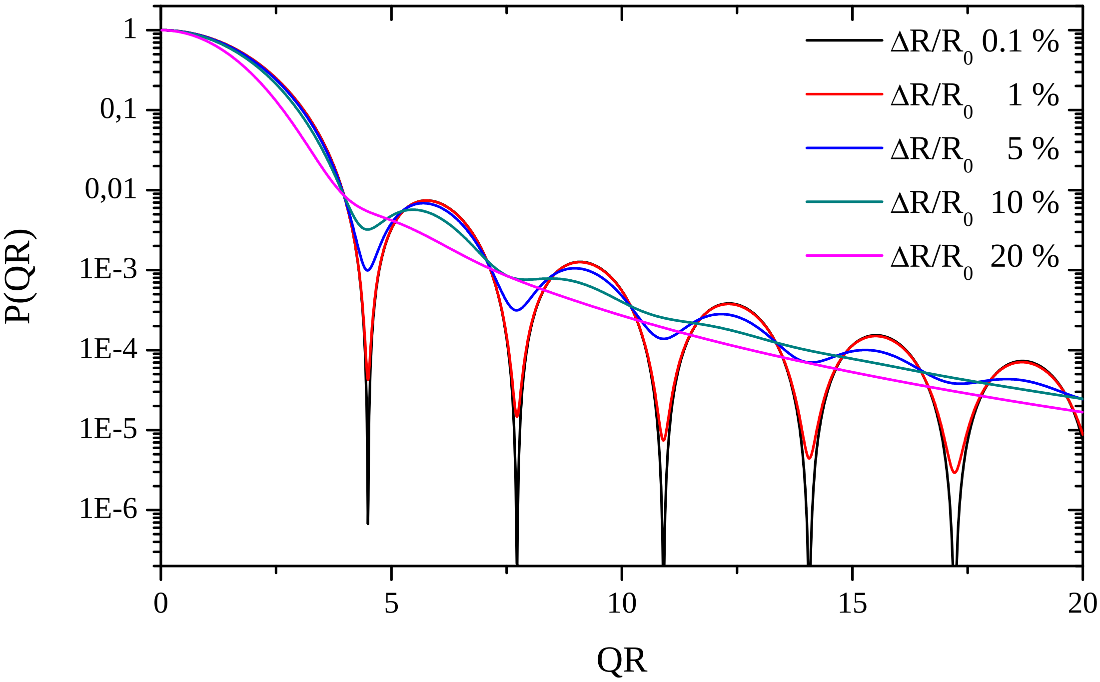

Figure 3.3.: Polydisperse sphere form factor $P(QR)$ as a function of QR. The polydispersity was varied between 0.1 % and 20 %, which corresponds to $Z = 999999$ and to $Z = 24$ respectively.

Fig. 3.3 shows the evolution of the sphere form factor of an ensemble of increasingly polydisperse spheres. For small polydispersities, the function resembles the form factor of a single sphere (3.2). With increasing polydispersity the minima are smeared out, a behavior which is more prominent for the oscillations at large momentum transfers Q.

3.2.3. Scattering of interacting particles

For a system of monodisperse particles, as assumed in eq. (3.9), the scattered intensity can be written as:

$$\langle I(\mathbf{Q})\rangle = N[a(\mathbf{0})]^2 P(\mathbf{Q}) S(\mathbf{Q}) \tag{3.19}$$

where $P(\mathbf{Q})$ is the single particle formfactor as described in eq. (3.14). The static structure factor $S(\mathbf{Q})$ describes the inter-particle structure of an ensemble of colloidal particles given by

$$S(\mathbf{Q}) = \frac{1}{N}\sum_{i=1}^{N}\sum_{j=1}^{N}\langle \exp(i\mathbf{Q}[\boldsymbol{r}_i - \boldsymbol{r}_j])\rangle. \tag{3.20}$$

For the limit of large momentum transfers, the structure factor $S(Q)$ oscillates around unity ($\lim_{Q\to\infty} S(Q) = 1$), as on these small length scales (smaller than the particle radius R) no inter-particle correlations are observable. In the limit of small momentum transfers ($\lim_{Q\to 0}$) the static structure factor can be related to macroscopic thermodynamical properties and gives access to the isothermal compressibility χ_T of a colloidal suspension via

$$S(0) = nk_B T \chi_T \tag{3.21}$$

where $n = N/V$ is the particle number density. Expansion of eq. (3.20) yields

$$S(\boldsymbol{Q}) = S(0) + \mathcal{O}(Q^2) \tag{3.22}$$

so that $S(0)$ can be estimated by an extrapolation of $S(Q)$ versus Q^2 towards $Q = 0$ (Donev *et al.*, 2005). The $S(Q \to 0)$ limit yields qualitative information about the interaction properties of the sample, with $S(0) < 1$ for repulsive interactions.

$S(Q)$ is related to the pair distribution function $g(r)$, which describes the relative conditional probability of finding a particle a distance r apart from another particle. The static structure factor can be written as:

$$S(Q) = 1 + 4\pi n \int_0^\infty \mathrm{d}r\, r^2 \left[g(r) - 1\right] \frac{\sin Qr}{Qr} \tag{3.23}$$

The inverse relation resulting in $g(x = r/[2R])$ from $S(Q)$ is

$$g(x) = 1 + \frac{1}{12\pi\phi x} \int_0^\infty \mathrm{d}(2RQ) \left[S(2RQ) - 1\right] 2RQ \sin(2RQx) \tag{3.24}$$

where $\phi = 4/3\pi R^3 n$ is the volume fraction of the particles.

3.2.4. Static structure factors of colloidal systems

The static structure factor $S(Q)$ depends on the direct particle interactions described by the pair potential $V(r)$. The evaluation of the static structure factor for a given pair potential is not straightforward and requires the determination of the pair distribution function $g(r)$ which is directly related to the potential of mean force between two spherical particles $U(r)$ via (Philipse and Vrij, 1988)

$$g(r) = \exp\left(-\frac{U(r)}{k_B T}\right). \tag{3.25}$$

For very dilute colloidal suspensions the potential of mean force equals the interaction pair potential $V(r)$. This is no longer valid for concentrated suspensions. The derivation of the static structure factor for a given interaction pair potential $V(r)$ can be achieved by using the Ornstein-Zernike equation, which provides a connection between the total correlation function $h(r)$ and the direct two-particle correlation function $c(r)$ and appropriate closure relations

$$h(r) = c(r) + n \int \mathrm{d}(\boldsymbol{r}')\, c(|\boldsymbol{r} - \boldsymbol{r}'|)\, h(|\boldsymbol{r}'|). \tag{3.26}$$

In a many-body system the total correlation function results from the direct correlation between two particles and many indirect contributions which are transferred between the two particles by chains of other particles. The total correlation function $h(r)$ can be described by means of the pair correlation function

$$h(r) = g(r) - 1. \tag{3.27}$$

In the case of colloidal particles interacting via a hard sphere interaction potential, the Percus-Yevick approximation (Percus and Yevick, 1958) has been used as a closure relation

$$g(r) = \exp\left(\frac{V(r)}{k_B T}\right)[g(r) - c(r)] \tag{3.28}$$

and an analytical solution has been derived by *Ashcroft* and *Lekner* (Ashcroft and Lekner, 1966) for a hard sphere model (see eq. (2.2)). The static structure factor of a hard sphere system as a function of the momentum transfer Q normalized to the radius of the particles R is only depending on the volume fraction. Fig. 3.4 shows the evolution of the static structure factor $S(QR)$ as a function of the volume fraction ϕ.

In the limit of dilute suspensions ($\lim_{\phi \to 0}$), the static structure factor equals unity for all momentum transfers, displaying thus a complete absence of interparticle interactions and subsequent ordering of the suspension of colloidal particles. For higher concentrations of colloidal particles, the static structure factor evolves into an oscillating function which displays a pronounced first maximum which can be related to a mean interparticle distance. With increasing volume fractions ϕ the height of the maximum increases, which corresponds to an increased ordering of the sample, and the position of the peak is shifted towards bigger momentum transfers Q, corresponding to a decrease of the mean interparticle distance.

For electrostatically stabilized systems, the evaluation of $S(Q)$ has been performed by *Hayter* and *Penfold* (Hayter and Penfold, 1981), using the closure relations of the mean spherical approximation (MSA):

$$\begin{aligned} h(r) &= \quad -1 & \quad r < 2R \\ c(r) &= \quad -\tfrac{V(r)}{k_B T} & \quad r > 2R \end{aligned} \tag{3.29}$$

where $V(r)$ for an electrostatical interacting system is given by a screened Coulomb potential given by eq. (2.4), which is depending on the volume fraction ϕ, the effective charge Z_{eff} of the colloidal particles, the permittivity of the suspending medium ϵ and the concentration of added electrolyte which increases the ionic strength of the suspension.

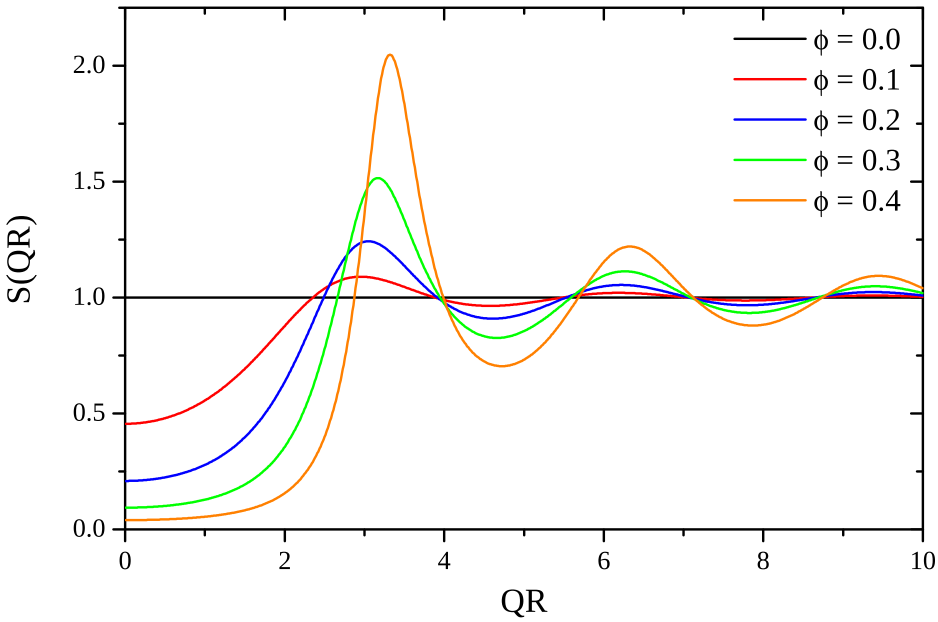

Figure 3.4.: Evolution of the static structure factor $S(QR)$ as a function of QR with increasing volume fraction ϕ calculated for a hard sphere interaction potential.

For charge stabilized systems, the MSA yields good agreement with medium to fairly concentrated suspensions, while it is less accurate to predict the structure of a dilute but still interacting system. Because of the long-range interactions the MSA calculates negative contact distances in these cases. To circumvent these unphysical results, a rescaling of the MSA is applied which results in the rescaled mean spherical approximation (RMSA) (Hansen and Hayter, 1982). For this procedure the screened Coulomb-interactions between the particles is reduced by scaling the radius of the particles to a radius according to a hard sphere potential. After the calculation of the static structure factor the radius is scaled back to the initial value.

In fig. 3.5 (top) the evolution of the static structure factor $S(QR)$ for a charge stabilized dispersion of colloidal particles as a function of the effective charge Z_{eff} of the particles is shown. The particles with a volume fraction $\phi = 0.1$ are dispersed in a deionized medium with the relative dielectric permittivity $\epsilon_R = 80.1$ at room temperature. It can be seen that the maximum of the static structure factor is increasing and narrowing with increasing charge.

In fig. 3.5 (middle) the effect of additional electrolyte in the medium is shown which is screening the electrostatic interactions between the colloidal particles. The effective charge $Z_{\text{eff}} = 300\,e^-$ while the other parameters are the same as in fig. 3.5 (top). The addition of electrolyte reduces the height of the maxima of the static structure factor as the electrostatic interactions are more and more screened by additional ions in the medium. The effect on the height and the shape of the peak

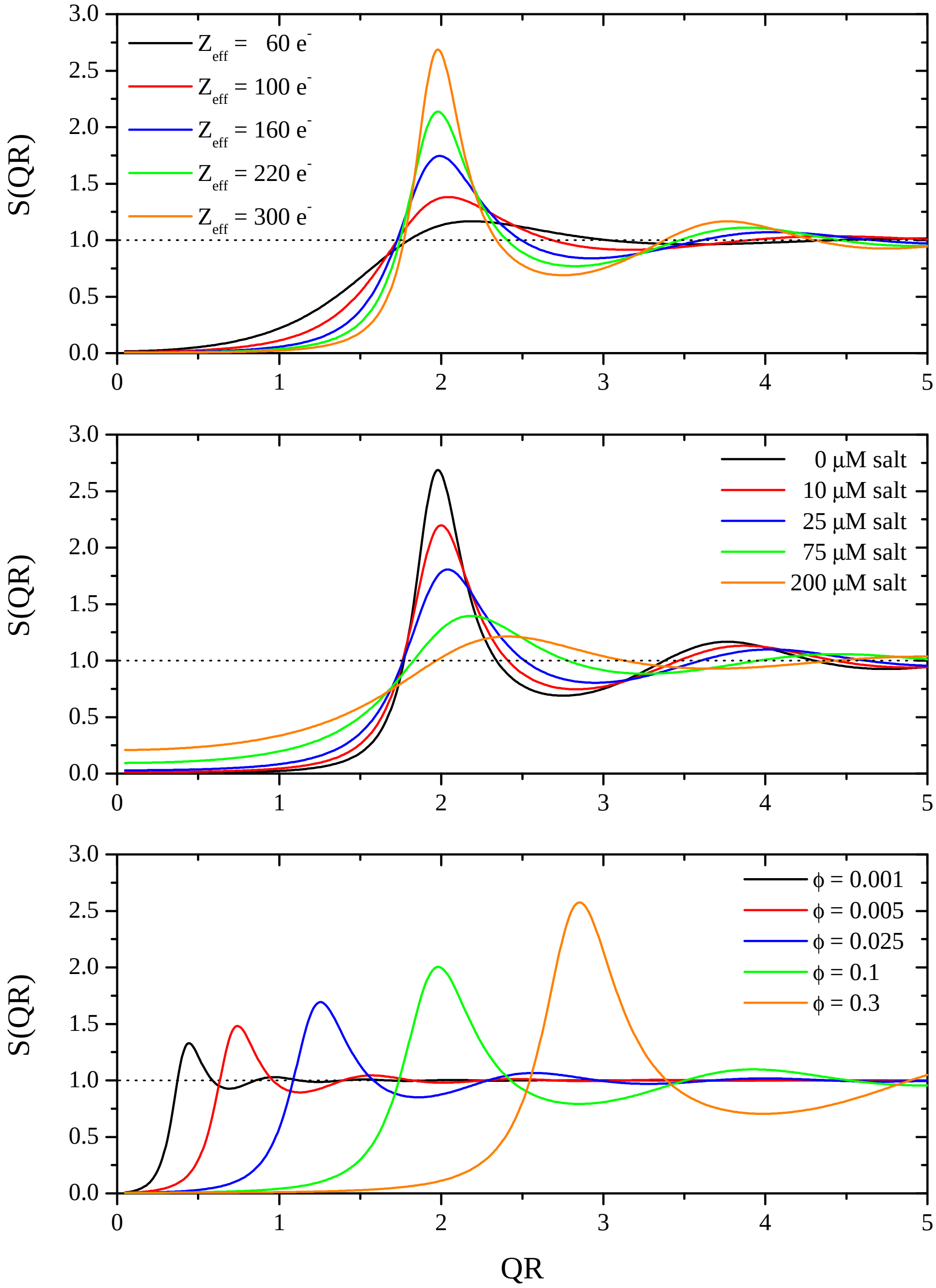

Figure 3.5.: Static structure factors calculated within the rescaled mean spherical approximation as a function of QR. The colloidal particles are dispersed in a medium at room temperature $T = 293.15\,\mathrm{K}$ and a relative dielectric permittivity of $\epsilon_R = 80.1$. Top: Evolution of the static structure factor as a function of the effective charge Z_{eff} of a deionized solution at a volume fraction $\phi = 0.1$. Middle: Evolution of the static structure factor as a function of the concentration of added electrolyte in the suspension. The other parameters are $Z_{\mathrm{eff}} = 300\,\mathrm{e}^-$ and $\phi = 0.1$. Bottom: Evolution of the static structure factor as a function of the volume fraction in a deionized solution. The effective charge of the colloidal particles is $Z_{\mathrm{eff}} = 200\,\mathrm{e}^-$.

of the static structure factor resembles the effect of a decreasing effective charge displayed in fig. 3.5 (top). However, small deviations can be seen – on the one hand, the isothermal compressibility of systems with higher amounts of added electrolyte is increasing indicated by higher values of $S(0)$ at similar peak values of $S(Q)$. On the other hand, a more pronounced shift towards higher QR values with decreasing peak values of $S(Q)$ can be noted for the addition of electrolyte as compared to decreasing values of Z_{eff}.

Fig. 3.5 (bottom) shows the effect of the concentration of colloidal particles on the static structure factor $S(QR)$. While the dispersion medium has the same characteristics as in fig. 3.5 (top), the effective charge is $Z_{\text{eff}} = 200\,\text{e}^-$. While the first peak of $S(QR)$ is shifted to higher momentum transfers Q with increasing volume fraction, the peak height is also increasing as the inter-particle interactions increase with decreasing distance between the particles. This shift of the peak towards higher momentum transfers Q with increasing volume fraction is much more pronounced in an electrostatically stabilized system as compared to a hard sphere system (fig. 3.4 on page 22). This is due to the different spatial arrangements of the colloidal particles. While in charge stabilized systems the colloidal particles are well separated and thus maximizing the interparticle distance due to the long-range interactions, the probability to find particles close to each other is higher in a hard sphere system. These long-range interactions are also resulting in a lower isothermal compressibility and corresponding lower $S(0)$ values of electrostatic interacting systems as compared to the hard sphere case.

3.3. Dynamic Scattering

If a sample with disordered scatterers is illuminated with coherent light, the electric field amplitudes scattered by different regions of the sample interfere and thus create an intensity distribution pattern in the far-field. This pattern, made out of patches of spatially or temporally fluctuating intensity, is called a "speckle" pattern, which reflects the instantaneous configuration of the scatterers. If the spatial arrangement of the scatterers in the sample is changing with time, (e.g. due to Brownian motion), the corresponding speckle pattern is also changing such that dark regions of low scattered intensity will become brighter and vice versa. At a given point of detection with the size of a typical speckle, these changes of the speckle pattern are therefore recorded as intensity fluctuations. These temporal fluctuations of the intensity are related to the dynamics of the scatterers in the sample.

By analyzing the temporal intensity fluctuations it is thus possible to get information about the underlying dynamics. At times short compared to the typical time scales of configurational changes in the sample, the intensity at a given point of detection will be correlated with the initial intensity. At long times, the configuration of the scatterers has changed and the resulting speckle pattern bears no resemblance to the initial speckle pattern and the intensity correlation will be thus lost. By recoding the intensity fluctuations in a time interval between t and τ this property can be quantified by the time correlation function

$$\langle I(0)I(\tau)\rangle = \lim_{T\to\infty}\frac{1}{T}\int_0^T \mathrm{d}t I(t)I(t+\tau). \tag{3.30}$$

For long times compared to the intensity changes the correlation between $I(0)$ and $I(\tau)$ are zero. The temporal evolution of the time correlation function drops from $\langle I^2\rangle$ at $t=0$ to the value $\langle I\rangle^2$ at large times

$$\lim_{T\to\infty}\langle I(0)I(\tau)\rangle = \langle I(0)\rangle\langle I(\tau)\rangle = \langle I\rangle^2. \tag{3.31}$$

In a photon correlation spectroscopy experiment, a detector with an aperture roughly the size of a single speckle of the sample is placed in the far-field region of the scattering pattern. The fluctuating signal recorded by the detector is proportional to the fluctuating scattered intensity $I(Q,t)$. This allows the calculation of the normalized intensity autocorrelation function $g_2(Q,t)$ at a given momentum transfer Q:

$$g_2(Q,\tau) = \frac{\langle I(Q,0)I(Q,\tau)\rangle}{\langle I(Q)\rangle^2}. \tag{3.32}$$

If the conditions i) that the scattering volume V contains a large number of particles, ii) that the range of spatial correlation is much smaller than $V^{1/3}$ and iii) that, given enough time, the particles can diffuse throughout the suspension are fulfilled, the electric field amplitude $E(Q,t)$ is a zero-mean complex variable.

This allows to relate the second order correlation function $g_2(Q,\tau)$ to the first order correlation function $g_1(Q,\tau)$ by the Siegert relation (Berne and Pecora, 1976):

$$g_2(Q,\tau) = 1 + \beta(Q)\frac{\langle \boldsymbol{E}^*(Q,0)\cdot \boldsymbol{E}(Q,\tau)\rangle^2}{\langle I(Q)\rangle^2} = 1 + \beta(Q)[g_1(Q,\tau)]^2. \tag{3.33}$$

The contrast $\beta(Q)$ is mainly depending on the coherence properties of the beam and on the ratio of detector area to speckle size. For completely incoherent radiation, $\beta(Q) = 0$ and $g_2(Q,\tau) = 1$ for all timescales. For fully coherent radiation, $\beta(Q) = 1$. In an experiment using visible light, the contrast is usually close to the ideal value of unity, while in a X-ray experiment the trade-off of between photon flux and coherence usually leads to a contrast of 5 - 10 %.

The normalized field auto-correlation function $g_1(Q,\tau)$ is also called normalized intermediate scattering function $f(Q,\tau)$, defined by

$$f(Q,\tau) = \frac{F(Q,\tau)}{F(Q,0)} \tag{3.34}$$

where $F(Q,\tau)$ is the intermediate scattering function given for N identical particles by

$$F(Q,\tau) = \frac{1}{N}\sum_{i=1}^{N}\sum_{j=1}^{N}\langle \exp(i\boldsymbol{Q}[\boldsymbol{r}_i(0) - \boldsymbol{r}_j(\tau)])\rangle \tag{3.35}$$

while $F(Q,0)$ can be identified with the static structure factor $S(Q)$.

3.3.1. Dynamics of colloidal suspensions

In a suspension of colloidal nano-particles with no inter-particle interactions the displacement of the particles is just due to Brownian motion. The intermediate scattering function $F(Q,\tau)$ equals the normalized intermediate scattering function $f(Q,\tau)$ as $F(Q,0) = S(Q) = 1$ due to the absence of inter-particle interactions and is given by

$$f(Q,\tau) = F(Q,\tau) = \frac{1}{N}\sum_{i=1}^{N}\langle \exp(i\boldsymbol{Q}[\boldsymbol{r}_i(0) - \boldsymbol{r}_i(\tau)])\rangle \tag{3.36}$$

where the cross-terms $i \neq j$ average out, so that it is simultaneously the self-part of the intermediate scattering function in eq. (3.35).

The displacement of a free diffusing particle is a Gaussian random variable $r_i(0) - r_i(\tau)$ of mean zero and with mean square value $\langle [r_i(0) - r_i(\tau)]^2\rangle$ (Pusey, 1991). Thus eq. (3.36) can be simplified to

$$f(Q,\tau) = \exp\left(-\frac{Q^2}{6}\langle [\boldsymbol{r}_i(0) - \boldsymbol{r}_i(\tau)]^2\rangle\right). \tag{3.37}$$

The mean square displacement for a free moving Brownian particle is given by eq. (2.12) $\langle [r_i(0) - r_i(\tau)]^2 \rangle = 6D_0\tau$ where D_0 is the free particle diffusion constant of a particle. The intermediate scattering function of non-interacting, Brownian particles is a simple exponential function and

$$f(Q,\tau) = \exp(-\Gamma\tau) \tag{3.38}$$

where the relaxation rate $\Gamma = D_0 Q^2$.

In the presence of interparticle interactions, the decay of the intermediate scattering function $F(Q,\tau)$ is generally non-exponential. The normalized intermediate scattering function $f(Q,\tau)$ is then usually analyzed in terms of a cumulant expansion

$$f(Q,\tau) = \exp(-\Gamma_1(Q)\tau + \Gamma_2(Q)\tau^2 - \Gamma_3(Q)\tau^3 + \ldots). \tag{3.39}$$

Here, $\Gamma_1(Q) = \Gamma(Q)$ is the first cumulant. The initial decay of the normalized intermediate scattering function $f(Q,\tau)$ yields the effective short-time diffusion coefficient $D(Q)$ of a colloidal suspension, according to *Snook et al.* (Snook *et al.*, 1983)

$$\lim_{\tau\to 0} -\frac{\mathrm{d}\ln f(Q,\tau)}{\mathrm{d}\tau} = \Gamma(Q) = D(Q)Q^2. \tag{3.40}$$

The dynamics probed by the effective short-time diffusion coefficient $D(Q)$ depends on the length scale $(2\pi/Q)$. Neglecting hydrodynamic interactions and just taking into account the direct particle interactions, the effective short-time diffusion coefficient is given by (De Gennes, 1959)

$$D(Q) = \frac{D_0}{S(Q)} \tag{3.41}$$

where D_0 is the free diffusion coefficient (eq. (2.10)) and $S(Q)$ is the static structure factor. The expression is sometimes referred to as the "De Gennes" narrowing, according to which the most likely density fluctuations decay the slowest. This effect, in ω-space, leads to a narrowing of the quasi-elastic line-width. This was experimentally observed for many systems, especially for diluted systems of interacting spheres such as by *Brown et al.* (Brown *et al.*, 1975).

With the inclusion of hydrodynamic interactions, the effective short-time diffusion coefficient can be written as

$$D(Q) = D_0\frac{H(Q)}{S(Q)} \tag{3.42}$$

where $H(Q)$ is the hydrodynamic function describing the effects of indirect particle interactions mediated by the dispersion medium. The hydrodynamic function can be expressed by (Nägele, 1996)

$$H(Q) = \frac{1}{ND_0Q^2}\sum_{i,j=1}^{N}\langle \hat{\boldsymbol{Q}} \cdot \boldsymbol{D}_{ij}(\boldsymbol{r}^N) \cdot \hat{\boldsymbol{Q}} \exp(i\boldsymbol{Q}[\boldsymbol{r}_i - \boldsymbol{r}_j])\rangle. \tag{3.43}$$

Here $\boldsymbol{r}^N$ denotes the spatial configuration of N particles, $\hat{\boldsymbol{Q}}$ is the unit vector in the direction of the momentum transfer $\boldsymbol{Q}$. $\boldsymbol{D}_{ij}$ denotes the many body diffusion tensor. The hydrodynamic function contains the configuration-averaged effect of the hydrodynamic interactions on the short-time dynamics.

Eq. (3.42) can relatively easily be understood in the limiting cases of $Q \rightarrow \infty$, $Q \rightarrow 0$ and $Q \approx Q_{max}$, the position of the first maximum of the static structure factor. On long length scales $Q \rightarrow 0$ the collective short-time diffusion of the system is probed. $D(Q)$ is frequently observed to be substantially larger than the free particle diffusion coefficient D_0 (Nägele, 1996), especially for systems with strong repulsive interaction forces.

With increasing momentum transfer Q, the dynamics on shorter length scales are probed. On length scales corresponding to mean interparticle distance, the static structure factor displays a first maximum while the dynamics of the system are substantially slowed down. This phenomenon can be interpreted as a "caging" of the particles by the neighboring particles, being thus not able to move freely at these specific length scales ("De Gennes" narrowing).

At large momentum transfers $Q \rightarrow \infty$, the dynamics on length scales significantly smaller than any interparticle distance are probed. The effective short-time diffusion constant $D(Q)$ reduces to the short-time self diffusion coefficient $D^{\mathrm{s,short}}$ (eq. (2.14)) of a single particle, which, in the absence of hydrodynamic interactions reduces to D_0

$$D(Q \rightarrow \infty) = D^{\mathrm{s,short}} = D_0 \cdot H(\infty). \tag{3.44}$$

3.3.2. Hydrodynamic functions

Intuitively, it might be expected that the hydrodynamic interactions in an suspensions of colloidal particles act as an additional friction force experienced by the particles causing a slowing down of the particles. This behavior should be even more pronounced when the concentration of the colloidal particles increases.

Indeed, this behavior has been reported experimentally for systems interacting via a hard-sphere potential (van Megen *et al.*, 1985; Segrè *et al.*, 1995; Fijnaut *et al.*, 1978), where the effective short-time diffusion coefficient $D(Q)$ was measured in the range covering in particular the region of the first peak of the static structure factor. The hydrodynamic functions show a relaxation of the hydrodynamic resistance in these systems at momentum transfers around the position of the maximum of the static structure factor Q_{max}, but are still smaller than unity.

To derive a theoretical description of the hydrodynamic functions, *Beenaker* and *Mazur* (Beenakker and Mazur, 1983, 1984) followed an approach were the mobility tensors $\boldsymbol{\mu}_{ij}(\boldsymbol{r}^N)$, which depend on the configuration of all particles $\boldsymbol{r}^N$, were calculated (the $\delta\gamma$-expansion). The mobility tensors $\boldsymbol{\mu}_{ij}(\boldsymbol{r}^N)$ relate the velocity $\boldsymbol{v}_i$ of a particle to the forces $\boldsymbol{F}_j$ exerted on each particle by the suspending fluid

$$\boldsymbol{v}_i = -\sum_{j=1}^{N} \boldsymbol{\mu}_{ij}\boldsymbol{F}_j. \tag{3.45}$$

While in the case of a dilute suspension the problem can be approximated by only taking into account two-sphere hydrodynamic interactions, for concentrated suspensions also many-body interactions have to be taken into account. By a resummation of all hydrodynamic contributions through an expansion of correlation functions of increasing order, *Beenaker* and *Mazur* derived an expression in terms of an ensemble average of the spatial configurations of the particles.

The resulting hydrodynamic function of the $\delta\gamma$-expansion depends on the radius R, volume fraction ϕ and the static structure factor $S(Q)$ of the sample and is given by

$$\begin{aligned} H(Q) = \frac{D_s(\phi)}{D_0} + \frac{3}{2\pi}\int_0^\infty \mathrm{d}(RQ')\left(\frac{\sin(RQ')}{RQ'}\right)^2 [1+\phi S_{\gamma 0}(RQ')]^{-1} \\ \times \int_{-1}^{1} \mathrm{d}x\,(1-x^2)(S|\boldsymbol{Q}-\boldsymbol{Q}'|-1) \end{aligned} \tag{3.46}$$

where the integration variable x is defined as $x = \cos(\widehat{\boldsymbol{Q},\boldsymbol{Q}'})$. The first part is the normalized short-time self diffusion coefficient $D_s(\phi)/D_0$, which is the Q-independent self-part of the hydrodynamic function and is depending on the volume fraction ϕ of the system via

$$\frac{D_s(\phi)}{D_0} = \frac{2}{\pi}\int_0^\infty \mathrm{d}x\left(\frac{\sin x}{x}\right)^2 [1+\phi S_{\gamma 0}(x)]^{-1}. \tag{3.47}$$

The function $S_{\gamma 0}$ is described in appendix A.

For ($Q \to \infty$) the hydrodynamic function equals $D_s(\phi)/D_0$, as the second term in eq. (3.46), containing the static structure factor, vanishes as $S(Q \to \infty) - 1 = 0$.

Fig. 3.6 displays the evolution of the hydrodynamic functions $H(QR)$ as a function of the volume fraction ϕ using the $\delta\gamma$-expansion to zeroth order for colloidal systems interacting via a hard sphere interaction potential.

The hydrodynamic functions show a pronounced Q-dependence, in particular a peaking behavior at positions close to the peak of the static structure factors, thus displaying a reduction of the hydrodynamic effects at length scales corresponding to the mean interparticle distance. It can be also seen that the effect of hydrodynamic interactions is more pronounced at small momentum transfer values $Q \to 0$ than at large $Q \to \infty$, thus displaying a stronger effect on the collective diffusion than on the

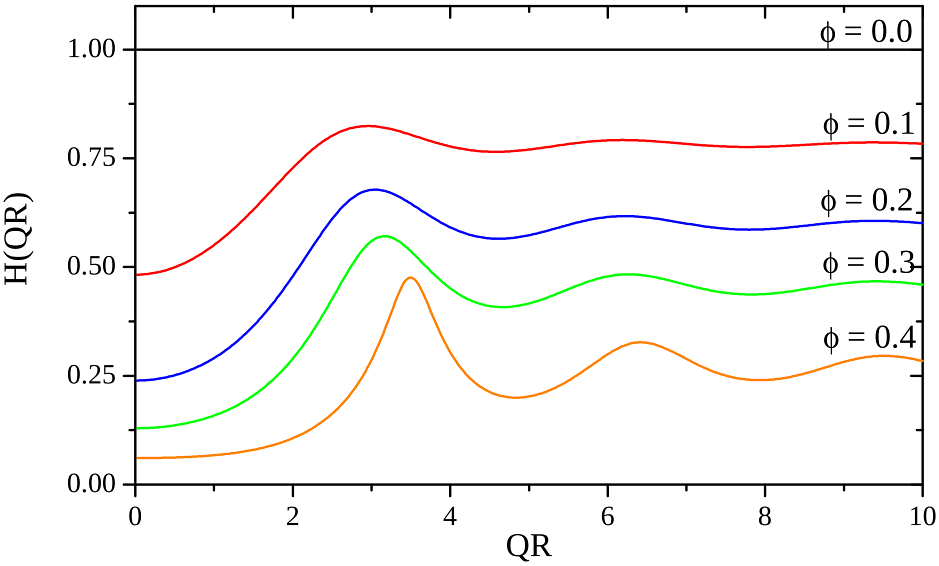

Figure 3.6.: Hydrodynamic functions $H(QR)$ as a function of on the volume fraction ϕ of hard-sphere colloidal systems, calculated using the $\delta\gamma$-expansion to zeroth order. The volume fractions are $\phi = 0, 0.1, 0.2, 0.3$ and 0.4.

short-time self diffusion of the colloidal particles. The effect of the hydrodynamic interactions increase with increasing volume fraction ϕ, which can be interpreted as increasing near-field effects of the hydrodynamic interactions acting as additional lubrication forces slowing down the dynamics of the system. For $\phi = 0$ the hydrodynamic function $H(Q) = 1$ at all momentum transfers. Note that the hydrodynamic functions do not display values above unity.

For small wavevector transfers Q, *Riese et al.* (Riese, 2000; Riese *et al.*, 2000b) derived an expression for the $\delta\gamma$-expansion making use of *Beenakkers* approximation of the fluctuation-expansion for small Q (Beenakker, 1984) that yields

$$\begin{aligned} H(Q) = \tilde{D}\Bigg\{1 + \frac{3}{2\pi}\int \mathrm{d}(RQ')\left[\frac{1}{(RQ')^2} - \frac{1}{3} + \mathcal{O}(Q'^2)\right] \\ \times \int \mathrm{d}x(1 - x^2)(S|Q - Q'| - 1)\Bigg\}. \end{aligned} \tag{3.48}$$

Here, the prefactor $\tilde{D} = \mu^* 6\pi\eta R$ where η is the viscosity of the suspending solvent and μ^* is the prefactor of the effective mobility tensor $\tilde{\mu}_{ij}^{eff}$ in the small wavevector Q limit.The prefactor $\tilde{D}$ affects not only the Q-independent self-part of the hydrodynamic function, but also acts on the Q-dependent part allowing thus a scaling of the whole hydrodynamic function. The first part in square brackets in eq. (3.48) represents the Oseen term, while the following terms represent the dipole contribution.

For a hard-sphere system with short-range interparticle interactions $\tilde{D}_{HS}$ is given by

$$\tilde{D}_{HS} = \mu^* 6\pi\eta R = \frac{\eta}{\eta^*} \tag{3.49}$$

where η is the viscosity of the solvent and η^* is to linear order in the volume fraction identical to the effective viscosity of the suspension given by (Beenakker, 1984)

$$\eta^* = \eta \left(1 + \frac{5/2\phi\gamma_0^{(2)}}{n} \right). \tag{3.50}$$

Here n is the number density of the colloidal particles, the calculation of $\gamma_0^{(2)}$ is explained in appendix A.

In charge stabilized systems, the interparticle interactions can act on long distances and are thus leading to ordered structures already at low particle concentrations. Although the interparticle distances can be relatively large, hydrodynamic interactions can play a decisive role in these systems. Contrary to the assumption that hydrodynamic interactions always causes a delay of the particle dynamics, it has been found in electrostatically interacting systems that the peak value of the hydrodynamic function can exceed unity $H(Q_{max}) > 1$ (Philipse and Vrij, 1988; Härtl *et al.*, 1999). This corresponds to a "speeding up" of the particle dynamics caused by hydrodynamic interactions. It is claimed that the movement of a particle induces a backflow of the displaced fluid, which can support the motion of a neighboring particle into the opposite direction. The effect of this backflow is more pronounced in suspensions of well separated particles, as it is the case for charge stabilized systems.

As a description of the hydrodynamic function in dilute to moderately concentrated electrostatically interacting colloidal suspensions, the pairwise additive approximation has been developed (Nägele *et al.*, 1993; Nägele *et al.*, 1994; Nägele and Baur, 1997). In this model, the hydrodynamic interactions are accounted for by a far-field expansion of the two-body hydrodynamic mobility tensors, in terms of the reciprocal interparticle distance r^{-1}, including terms up to the power of r^{-8}. The resulting hydrodynamic function is split into a self-part $H^i(g(r))$ and a distinct, Q-dependent part $H^d(Q, g(r))$:

$$H(Q) = H^i(g(r)) + H^d(Q, g(r)). \tag{3.51}$$

The calculation of the pairwise additive approximation depends on the volume fraction ϕ and the pair distribution function $g(r)$ of the system and is given by

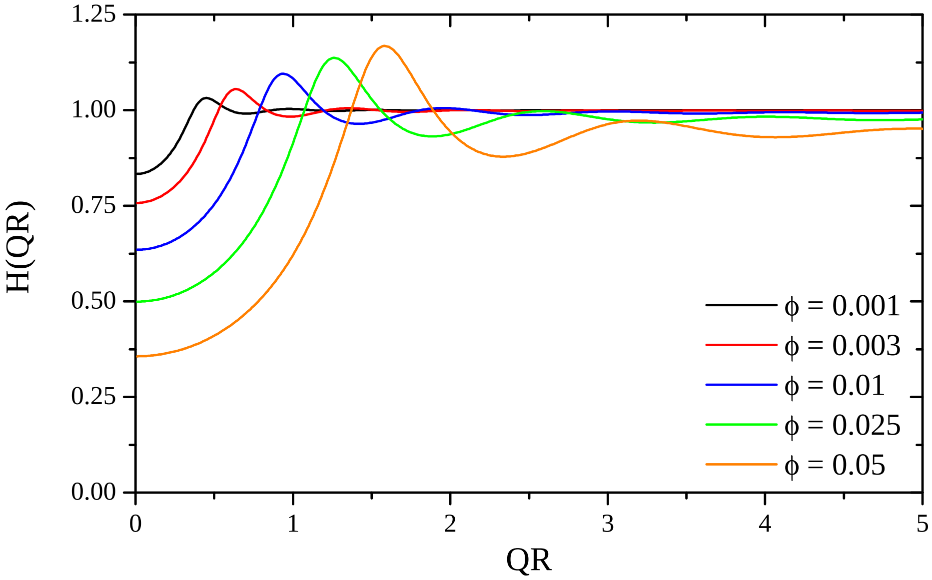

Figure 3.7.: Hydrodynamic functions $H(QR)$ as a function of the volume fraction ϕ of electrostatically interacting deionized colloidal systems, calculated using the pairwise additive approximation. The parameters used for the calculation were an effective charge of 200 e^-, a temperature of 293.15 K, and a relative permittivity ϵ_r of 80.1.

$$\begin{aligned} H^i(g(r)) = 1 + \phi \Bigg(&-\frac{15}{8}\int_1^\infty \mathrm{d}x \frac{g(x)}{x^2} + \frac{17}{64}\int_1^\infty \mathrm{d}x \frac{g(x)}{x^4} \\ &+ \frac{253}{1024}\int_1^\infty \mathrm{d}x \frac{g(x)}{x^6} - \frac{737}{1024}\int_1^\infty \mathrm{d}x \frac{g(x)}{x^8} \Bigg) \end{aligned} \tag{3.52}$$

$$H^d(y, g(r)) = -15\phi \frac{j_1(y)}{y} + 18\phi \int_1^\infty \mathrm{d}x [g(x) - 1] x \left(j_0(xy) - \frac{j_1(xy)}{xy} + \frac{j_2(xy)}{6x^2} \right) \tag{3.53}$$

where j_n are the spherical Bessel functions of order n. The self-part, $H^i(g(r))$, is again identical to the short-time self-diffusion coefficient $D^{\mathrm{s,short}}$. A deficiency of the pairwise additive approximation is the prediction of unphysical negative values at larger volume fractions for wave-vectors Q smaller or bigger than the position of the static structure peak Q_{max} (Nägele, 1996). The validity of the pairwise additive approximation has thus to be restricted to systems below a volume fraction $\phi \approx 0.1$, where the particles are still considerably separated from each other.

Fig. 3.7 shows the evolution of the hydrodynamic functions $H(QR)$ with increasing volume fraction ϕ calculated using the pairwise additive approximation. In agreement with the $\delta\gamma$-expansion, the hydrodynamic functions show a strong decrease of the dynamics of the particles at small momentum transfers Q, where the hydrodynamic interactions lead to a slowing down of the collective motions of the particles.

At large wavevector transfers Q, the hydrodynamic functions oscillate around the short-time self diffusion coefficient, which is approaching unity with decreasing volume fraction. Contrary to the $\delta\gamma$-expansion results for a hard sphere model, at values around the peak of the static structure factor $H(Q_{max}R)$ is larger than unity, indicating thus an increase of the particles' dynamics due to hydrodynamic interactions. This increase of particle mobility is more pronounced with increasing volume fraction ϕ for the modeled interaction potential and can be attributed to the dominant role of far-field effects in the hydrodynamic interactions in the case of low volume fractions and electrostatically interacting systems. These are usually interpreted as a backflow of displaced solvent by the motions of neighboring particles on length scales of the mean interparticle spacing.

3.3.3. Experiments under flow

When performing scattering experiments with X-rays, the interaction of the photons with the sample might cause damage to the sample due to the high energy of the X-ray photons. To avoid beam damage of the colloidal samples, the X-ray scattering experiments were performed on flowing samples to minimize the time the sample was exposed to an X-ray beam.

In the case of a fluid in laminar flow the autocorrelation functions are determined by three independent factors: The diffusive motion of the scatterers due to thermal fluctuations in the sample and the direct and indirect particle interactions, the transit time of the particles moving through the scattering volume and a shear induced oscillatory decorrelation depending on the velocity gradient of the particles in the scattering volume.

The contribution of diffusive motions of a sample undergoing shear flow with a uniform shear rate $\dot{\gamma}$ to the normalized intermediate scattering function is described by (Ackerson and Clark, 1981)

$$|f_D(\boldsymbol{Q},\tau,\dot{\gamma})|^2 = \exp\left[-2\Gamma(Q)\tau\left(1-\frac{Q_{\parallel}Q_{\perp}}{Q^2}\dot{\gamma}\tau+\frac{1}{3}\frac{Q_{\parallel}^2}{Q^2}(\dot{\gamma}\tau)^2\right)\right] \tag{3.54}$$

where $\boldsymbol{Q}$ is the momentum transfer with the components $Q_{\parallel}$ parallel and $Q_{\perp}$ perpendicular to the direction of the flow and $\Gamma(Q)$ is the relaxation rate which is related to the effective diffusion coefficient $D(Q)$. In a scattering geometry perpendicular to the flow direction $Q_{\parallel} = 0$ and $\Gamma(Q)$ is thus independent of the the uniform shear rate $\dot{\gamma}$.

The second contribution to the intermediate scattering function arises from the constant flow of particles through the scattering volume, where particles enter the scattering volume replacing other particles that leave the scattering volume on the other side. This results in a second relevant time scale, the transit frequency $\nu_{tr} \propto v_0/h$. The transit frequency is depending on the size of the scattering volume h and the average velocity of the particles v_0. The effect of the transit frequency on the normalized intermediate scattering function is given by (Busch *et al.*, 2008)

$$|f_T(\tau)|^2 \propto \exp[-(\nu_{tr}\tau)^2]. \tag{3.55}$$

The third contribution to the normalized intermediate scattering function is due to shear induced effects, caused by particles moving with different average velocities. It can be written as a double integral over the scattering volume which can be approximated by a line of length R (Narayanan *et al.*, 1997)

$$|f_S(\boldsymbol{Q},\tau)|^2 = \frac{1}{4R^2}\int_{-R}^{R}\int_{-R}^{R}\cos(\boldsymbol{Q}\tau\delta\boldsymbol{v}(r_1,r_2))\mathrm{d}r_1\mathrm{d}r_2 \tag{3.56}$$

where δv is the velocity difference between two particles separated by the distance $r = r_1 - r_2$. The integral has been solved analytically for a uniform shear rate

$$|f_S(\boldsymbol{Q},\tau)|^2 = \left[\frac{\sin(\Gamma_s\tau)}{\Gamma_s\tau}\right]^2. \tag{3.57}$$

Here, Γ_s is the shear relaxation rate and depends on the momentum transfer Q and the flow velocity v via $\Gamma_s = Q_{||}v$. If the scattering geometry is perfectly transverse, $Q_{||} = 0$ and thus the intermediate scattering function is not effected by shear induced effects. As the three factors contributing to the normalized intensity autocorrelation function g_2 depend on the scattering geometry, they lead to (Busch *et al.*, 2008)

$$g_{2,\perp}(Q,\tau) = \beta(Q)\cdot\exp[-2\Gamma(Q)\tau]\cdot\exp[-(\nu_{tr}\tau)^2] + 1 \tag{3.58}$$

and

$$g_{2,||}(Q,\tau) = \beta(Q)\cdot\exp\left[-2\Gamma(Q)\tau\left(1+\frac{(\gamma\tau)^2}{3}\right)\right]\cdot\exp[-(\nu_{tr}\tau)^2]\cdot\left[\frac{\sin(\Gamma_s\tau)}{\Gamma_s\tau}\right]^2 + 1. \tag{3.59}$$

$g_{2,\perp}$ is the normalized intensity autocorrelation function at momentum transfers perpendicular and $g_{2,||}$ is the normalized intensity autocorrelation function at momentum transfers parallel to the flow direction while $\beta(Q)$ denotes the speckle contrast. During the experiment, the dynamic behavior of the sample was measured just in the perpendicular direction to the flow to get the best access to the diffusion depending relaxation rate $\Gamma(Q)$.

3.4. Multiple scattering

The expressions for the scattered intensity and the intermediate scattering function only hold for "single scattering" of light. In order to be able to measure the statics and dynamics of a colloidal system, it has to be ensured that the measurements are performed in the single scattering limit. This limit is characterized by the condition

$$L \ll l_S \tag{3.60}$$

where L is the sample size and l_S is the mean distance between two scattering events, given in the dilute limit by

$$l_S = \frac{1}{n\sigma}. \tag{3.61}$$

Here n is the number density of the colloidal particles and σ is the scattering cross section. The scattering cross section of colloidal particles of refractive index n_1 in a dispersion medium of refractive index n_0 is given by the Rayleigh-Gans approximation (van de Hulst, 1981)

$$\sigma \propto \pi R^2 \left| \frac{n_1}{n_0} - 1 \right| \tag{3.62}$$

under the condition that the refractive index contrast is small $|n_1/n_0 - 1| \ll 1$ and $4\pi\, n_0 R |n_1/n_0 - 1| / \lambda \ll 1$ where λ is the wavelength of the scattered light in vacuum.

The single scattering limit can thus be fulfilled by either working in the dilute limit ($n \to 0$), which excludes the interesting case of concentrated samples exhibiting strong particle interactions, or by ensuring that the refractive index of the scatterers nearly matches the refractive index of the medium $n_1/n_0 \to 1$.

By using X-rays the latter condition is always fulfilled, as the refractive index for X-rays is always close to unity, so that multiple scattering is nearly absent. In the case of visible light, this is not true. The necessity to match the index of refraction of particles and surrounding medium restricts the choice of possible dispersion mediums, which puts severe limits to the possibility to tune the direct particle interactions in the case of electrostatically interacting systems which depend sensitively on the properties of the suspending fluid.

Therefore the measurements of concentrated systems were performed using X-rays. However, the concentration range of light scattering methods was enhanced by employing cross-correlation dynamic light scattering which enables the detection of the single scattering component of the total fraction of scattered light (Urban and Schurtenberger, 1998).

4. Experimental Details

4.1. Synthesis of colloidal model systems

A standard method for the preparation of polymeric colloids is radical emulsion polymerization. A radical emulsion process, schematically shown in fig. 4.1, is in the simplest case a polymerization of a monomer of low water solubility in a reaction vessel in an aqueous phase, where the polymerization process is initiated by a water-soluble initiator (Thickett and Gilbert, 2007). The reaction can be divided into three main phases: The particle formation, further propagational growth and the termination process. In the first phase the nucleation of particles takes place. As the reaction vessel is agitated during the synthesis process, the monomers form small droplets in water which act as monomer reservoirs during the synthesis process. The reactions starts when the monomers are being turned into radicals by the reaction initiator. These radical monomers have a higher solubility in water which allow them to enter the aqueous phase where they start to grow into small chains of oligomers which still have a radical center on one end of the growing chain. Depending on whether or not the reaction is taking place above or below the critical micelle concentration (CMC), (Hergeth *et al.*, 1992) two mechanisms of precursor particle formation may occur: Above the CMC, the growing oligomers which reach the chain length z become amphiphilic and are thus able to form micelles together with other oligomers having reached the chain length z. These small micelles grow by chain propagation into mature particles. Below the CMC, the first created oligomers continues to grow until they reach the critical chain length j_{crit} where the growing oligomer is no longer soluble in the aqueous phase and undergoes a coil-to-globule transition forming a precursor particle which either continues growth or coagulates with other precursor particles until a stable mature particle is formed, a process known as homogeneous nucleation (Priest, 1952).

In the second phase, the particles grow by propagation of the polymer-chains in the presence of monomers. In this phase no new precursor particles are formed, as the probability for newly formed oligomers of chain length z to enter a mature particle is much bigger than to form a new precursor particle. In the third phase, when the monomer is exhausted, the remaining monomer contained within the particles is polymerized until the reaction finally stops at the exhaustion of either monomers or radicals.

While it is possible to stabilize also polymeric colloids both sterically (the hard sphere case) and via electrostatic interactions, just the latter stabilization mechanism

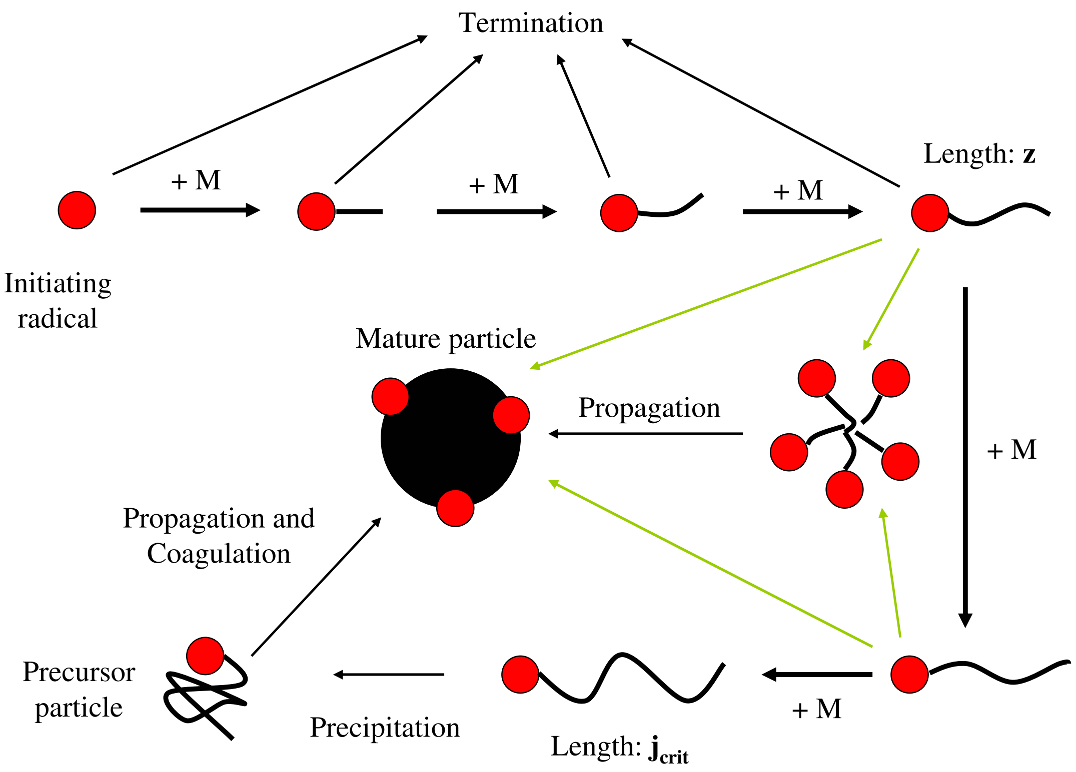

Figure 4.1.: Schematic representation of a radical emulsion polymerization above and below the critical micelle concentration (CMC). M stands for monomer, j_{crit} for the critical chain length of the formed oligomers and z for an oligomer made out of z monomers. The green arrows show the entry points of the formed oligomers into the formed micelle respectively precursor particle (modified from (Thickett and Gilbert, 2007)).

was used. The polymeric system of choice was a system made out of poly-methyl methacrylate (PMMA). This system offers the advantage of a high surface charge by the internalization of sulfate groups at the end of the propagating polymer chains. To enhance the scattering properties of the polymer, two different functionalized monomers were used for the radical polymerization containing either fluorine or silicon atoms to enhance the electron density of the colloidal particles. A typical reaction, as described by Härtl (Härtl and Zhang-Heider, 1997) took place in a 2.5-liter three-neck flask equipped with a reflux condenser with a water cooling temperature of about 281 K, a nitrogen inlet tube, and a magnetic stirrer set to a stirring speed of 700 rpm (rpm = revolutions per minute) during the whole synthesis process. The reaction temperature was varied between 47.5 K and 65 K and held constant by immersing the reaction vessel in a temperature bath. 1.5 l of water was added to the flask, and saturated with nitrogen to remove the oxygen in the water. A mixture (molar ratio 1:1) of the two monomers 1H,1H,5H-Octafluoropentylmethacrylate (abcr GmbH & Co.KG, Karlsruhe, Germany) and Methacryloxymethyltrimethylsilane (abcr GmbH & Co.KG, Karlsruhe, Germany) was added. In addition, a cross-linker, 2,2,3,3,4,4,5,5-Octafluorohexanediol-1,6-dimethacrylate (abcr GmbH & Co.KG, Karlsruhe, Germany), was added to allow cross-linking of the propagating chains to stabilize the formed nano-particles. As a redox-system a solution of $NaSO_3$ (Fluka, Buchs, Switzerland) and $(NH_4)_2Fe(SO_4)_2$ (Fluka, Buchs, Switzerland) in deionized water was added. The reaction was initialized by adding a solution of the initiator $K_2S_2O_8$ (Merck, Darmstadt, Germany) in deionised water.

To increase the charge of the colloidal particles, for some syntheses a subsequent second synthesis step (Synthesis step B) was carried out, resulting in a further growth of the colloidal particles accompanied by a higher surface charge. This second synthesis step was carried out 24 h after the first synthesis step at the same synthesis conditions. Therefore, a solution of the radical iniator $K_2S_2O_8$ in water and a monomer mixture of 1H,1H,5H-Octafluoropentylmethacrylate (abcr GmbH & Co.KG, Karlsruhe, Germany) and Methacryloxymethyltrimethylsilane (abcr GmbH & Co.KG, Karlsruhe, Germany) (molar ratio 1:1) was prepared. Every 30 min 0.5 ml of the initiator solution and 0.5 ml of the monomer mixture were pumped by a peristaltic pump system into the reaction mixture. The reaction vessel was continuously stirred and kept under nitrogen atmosphere. The newly formed oligomers were incorporated in the colloidal particles, and due to the enhanced presence of initiator resulting in sulfate groups at the surface of the colloids the effective charge of the particles could be enhanced.

After the synthesis had finished, the remaining products of the reaction, like remaining monomer or free oligomers of low molecular weight, were removed by dialysis against deionized water for 10 to 12 days. Afterwards, the colloidal suspensions were concentrated by vacuum distillation, and remaining stray ions were removed by the addition of a mixed bed ion exchanger (Merck, Darmstadt, Germany).

For the experiments, the ion exchanger was removed by filtering and the final concentration of the colloidal particles was adjusted either by dilution with deionised water or by gentle centrifugation for 24 h resulting in soft sediment of colloidal particles which is easily redissolved in water. If electrolyte was added to the samples, small volumes of different concentrations of dissolved potassium-chloride KCl (Merck, Darmstadt, Germany) in deionized water were added instead of the same volume of deionized water.

For the experiments two systems of different particle size and effective charge were synthesized and used for investigation. One of these systems was already purified after the first synthesis step, while for the other system the second synthesis step B has been performed.

4.2. Static and dynamic light scattering

The static and dynamic light scattering experiments have been performed using the spectrometer-goniometer-system *3D LS Spectrometer* (LS Instruments AG, Fribourg, Switzerland), which is schematically sketched in fig. 4.2 and enables cross-correlation experiments by performing two scattering experiments simultaneously.

As light source, a helium-neon-laser with a wavelength $\lambda = 632.8\,\mathrm{nm}$ was used. The emitted light with an intensity I_0 is deflected by two mirrors and can be adjusted in intensity by an absorber system with filters of an optical density (OD) between 0.3 and 5.3, where the optical density is the negative decadic logarithm of the absorption

$$I_{\mathrm{trans}} = I_0 \cdot 10^{-OD}. \tag{4.1}$$

The transmitted intensity I_{trans} is monitored by a photo diode, which is situated behind a semitransparent mirror which partially deflects the laser light. The beam is afterwards split into two beams of equal intensity by a prism system, the resulting two beams are focused by a lens on the same scattering volume in the sample cell. The scattered light is defocused by a lens and subsequently detected by two avalanche photo diodes placed on a goniometer arm which enables to detect the scattered light at angles θ between 30° and 150°. The resulting signal of the avalanche photo diodes is fed into two hardware multitau-correlators, which compute the time autocorrelation functions.

The round sample cell of a diameter of 10 mm consists out of quartz glass and is placed in a temperature-controlled bath of cis/trans-decalin which is index-matched to the refractive index of the sample cell to suppress scattering of the sample cell wall.

The set-up enables cross-correlation experiments by using a so called 3D set-up, expanding thus the possible range of concentrations which can be probed using light scattering methods by isolating single scattering events from contributions of multiple scattering. For this purpose, two scattering experiments are performed simultaneously on the same scattering volume and at the same wavevector transfer Q and the signals detected by two detectors are cross correlated

$$G_{12}(\tau) = \langle I_1(0) I_2(\tau) \rangle \tag{4.2}$$

where I_1 and I_2 denote the intensity detected by detectors 1 and 2 respectively. In the 3D set-up, both detectors detect the scattered light from both incident beams and thus both scattering experiments. The cross-correlation function can be thus written as (Urban, 1999)

$$G_{12}(\tau) = \langle I_1^I(0) I_2^I(\tau) \rangle + \langle I_1^I(0) I_2^{II}(\tau) \rangle + \langle I_1^{II}(0) I_2^I(\tau) \rangle + \langle I_1^{II}(0) I_2^{II}(\tau) \rangle \tag{4.3}$$

where arabic numbers denote again the detector and roman numbers denote the incident beam. The undesired contributions of the "wrong" incident beams are

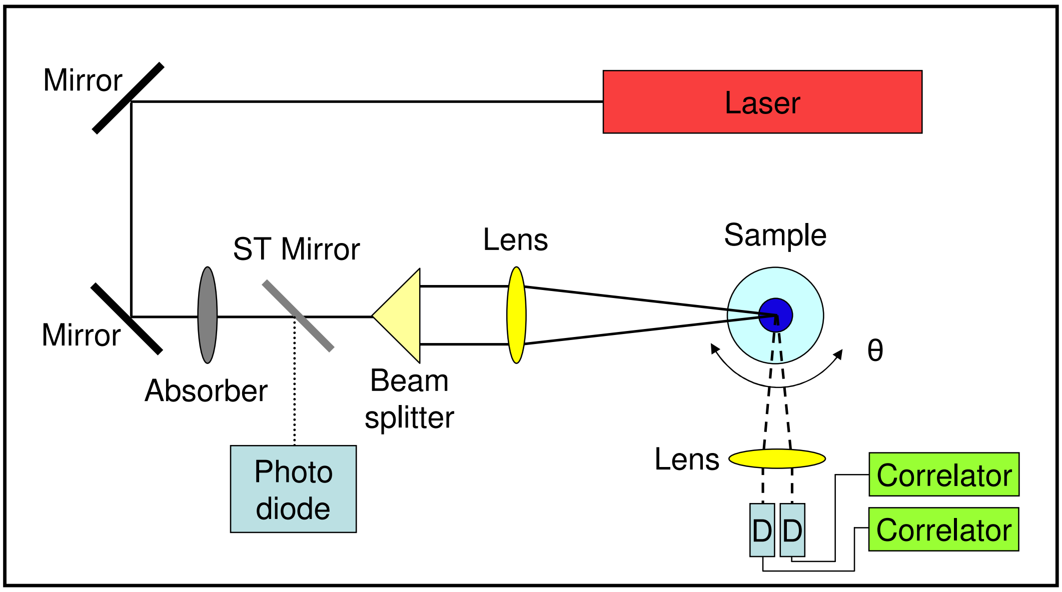

Figure 4.2.: Sketch of the light scattering set-up. The light emitted by the laser is deflected by two mirrors and split into two beams which are focused on the same scattering volume in the sample. This splitting of the beam enables cross-correlation experiments in a so called 3D set-up. The scattered light is detected by two detectors (D) at a scattering angle θ, the resulting signals are fed into two hardware multitau-correlators. The intensity of the laser beam can be adjusted by an absorber system and is monitored by a photo diode.

detected by the detectors, but as they scatter at different momentum transfers due to the geometry of the experimental set-up ($Q_1 \neq Q_2$), they are completely uncorrelated (Schätzel, 1991). In eq. (4.3) just the second term gives correlated contributions to $G_{12}(\tau)$, resulting in the normalized intensity correlation function (Urban, 1999)

$$g_{2,12}(\tau) = \frac{3\langle I_1\rangle\langle I_2\rangle + \langle I_1^I(0) I_2^{II}(\tau)\rangle}{\langle I_1^I + I_1^{II}\rangle\langle I_2^I + I_2^{II}\rangle}. \tag{4.4}$$

The possible maximal contrast of the normalized intensity correlation function in a 3D cross correlation experiment is thus $\beta_{12} = 0.25$.

4.3. X-ray scattering experiments

While coherent visible light is easily available since the invention of lasers, even partially coherent light sources in the X-ray regime have become available just recently. In addition, the flux of X-rays at third-generation synchrotron sources is several orders of magnitude more intense than previously available. By using just the partially coherent part of this X-ray beam it is possible to conduct coherent scattering experiments also with X-rays. The advantage of X-rays lies in their large penetration depth, making it possible to also analyze opaque samples (Riese *et al.*, 2000a), the absence of multiple scattering and in the extended wavevector transfer range accessible (Grübel *et al.*, 2000).

Two wavefronts are coherent if their phase difference is temporarily constant, allowing thus for constructive and destructive interference. The coherence time can then be defined as the maximum time interval during which the phase differences between all waves interfering at a certain point in space differ less than 2π. Analogous, a wave field is spatially coherent if the phase difference of any partial wave changes by less than 2π during a certain observation period. Since a real X-ray beam is no perfectly coherent source as it is not completely monochromatic and does not propagate perfectly into one direction, the coherence of the beam can be described by coherence lengths.

The longitudinal or temporal coherence length ξ_l, which arises due to the not perfect monochromaticity of the X-ray beam, depends on the wavelength λ and the bandwidth $\Delta\lambda/\lambda$ of the beam and is given by (Als-Nielsen and McMorrows, 2001)

$$\xi_l = \frac{\lambda}{2}\frac{\Delta\lambda}{\lambda}. \tag{4.5}$$

The transverse coherence length is caused by the finite source d_S of the X-ray beam, which causes slightly different directions of propagation for the emitted waves at a distances R_S from the source. The transverse coherence length ξ_t can be defined as (Als-Nielsen and McMorrows, 2001)

$$\xi_t = \frac{\lambda}{2}\frac{R_S}{d_s}. \tag{4.6}$$

In order to conduct experiments with partially coherent X-rays, the bandwidth of the X-rays is monochromatized to typically $\Delta\lambda/\lambda \approx 10^{-4}$ and the beam size is adjusted to a size which is comparable to the transverse coherence length.

The X-ray scattering experiments have been performed at the beamline ID10A at the European Synchrotron Radiation Facility (ESRF) in Grenoble, France (Grübel *et al.*, 1994; Abernathy *et al.*, 1998). A layout of the beamline and the experimental set-up is schematically sketched in fig. 4.3.

The X-rays emitted by a set of three undulator segments are vertically focused by a beryllium compound refractive lens, which is possible due to the smaller vertical than horizontal source size and subsequently bigger transverse coherence length ξ_t in the vertical than in the horizontal, and pass through a system of primary slits. The X-ray beam is subsequently monochromatized by a silicon(111) crystal to a photon energy of 8 keV, corresponding to a wavelength of $\lambda = 1.55\,\text{Å}$. The bandwidth provided by the monochromator $\Delta\lambda/\lambda \approx 1.4 \times 10^{-4}$ which corresponds to a longitudinal coherence length of $\xi_l \approx 1\,\mu\text{m}$.

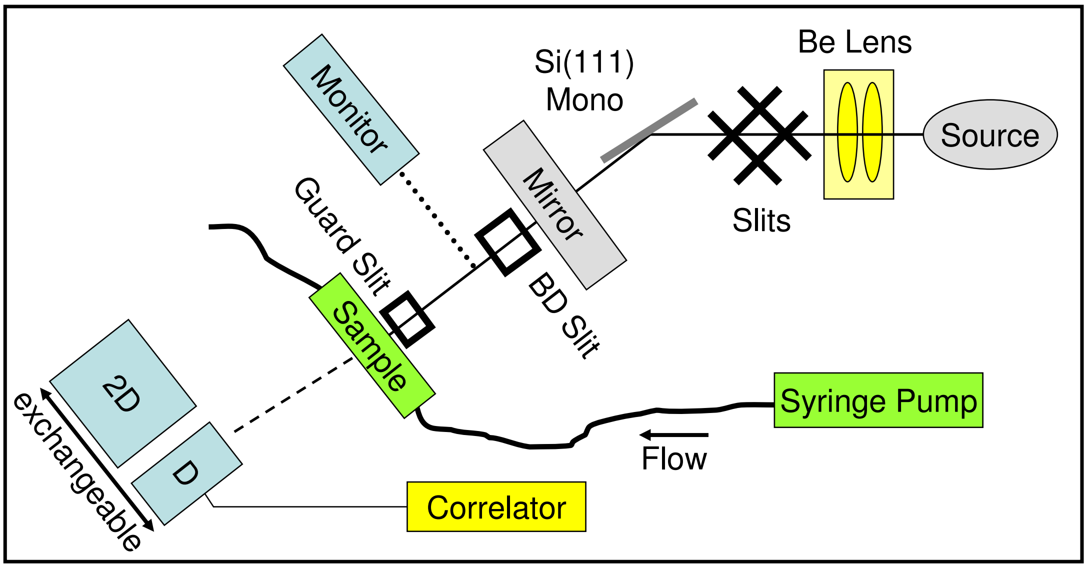

Figure 4.3.: Sketch of the beamline ID10A. The X-rays emitted by the source can be focused by a set of beryllium lenses before passing through several slit systems. The X-rays are monochromatized by a Si(1 1 1) monochromator and higher harmonics are suppressed by reflection of a mirror placed in vertical reflection geometry. Further downstream the beam size is collimated by a set of beam defining (BD) slits before a fraction of the beam is scattered by a kapton foil and detected by a monitor detector. Finally the beam is scattered by the sample placed behind a guard slit and the scattered intensity is subsequently detected either by a point detector (D) connected to a multitau-correlator or a 2D-detector (2D). The sample is being pumped by a syringe pump through a quartz capillary placed in the X-ray beam.

Further downstream the reflection by a mirror suppresses higher harmonics generated by the undulator and the X-ray beam is collimated to the final size by a set of beam defining slits. During the experiments, the beam size was typically between $10\,\mu m \times 10\,\mu m$ and $20\,\mu m \times 20\,\mu m$. The intensity of the collimated beam was monitored by a point detector which detects the scattering from a polyimid foil placed in the beam path. This allows for the correction of intensity fluctuations in the primary beam, which would cause additional effects in the intensity-autocorrelation functions.

The Fraunhofer fringes resulting from the beam defining slits and additional stray scattering are suppressed by a tantalum guard slit placed directly in front of the sample. Finally the beam impinges on the sample, and the scattered intensity is detected by either a 2D-detector in the case of the performed time-averaged experiments or by a point detector for photon correlation experiments. Both detectors can be interchanged during the experiment, enabling thus the measurement of the static and dynamic behavior of the same sample. To avoid beam damage of the 2D detector, a beam stop was placed directly in front of the detector which blocks the direct beam. The detectors were placed at a distance $\approx 2\,\mathrm{m}$ behind the sample.

The usage of a 2D detector offers enhanced statistics for the time-averaged scattering experiments, especially in the case of high Q-values where the count rate is drastically reduced due to the Q^{-4} dependence of the scattered intensity. As the investigated samples consist of spherical particles, the scattered light by the sample is completely isotropic and can be azimuthally averaged. The used 2D detector was a charge coupled device detector with a total area of 1242×1152 pixels and a pixel size of $22.5\,\mu\mathrm{m} \times 22.5\,\mu\mathrm{m}$. Typically a series of 100 to 200 pictures with a data acquisition time of 0.1 s to 10 s was taken.

Series of 100 to 200 frames were averaged and a dark count value was subtracted from the time averaged data. The dark count value was determined by taking a picture series with the same number of pictures and the same data acquisition time without any illumination of the detector and subsequently averaging of the dark count series. The time-averaged data was normalized to the incident flux on the sample, provided by the monitor detector and to the transmission of the sample. To subtract the scattering of the dispersion medium and additional parasitic scattering, the same experiment was performed on the pure dispersion medium. The background data were afterwards subtracted from the normalized scattering image. Finally the images were azimuthally averaged.

As the short-time dynamics of the colloidal particles investigated in the experiments are on timescales faster than the possible frame-rates for present-day X-ray 2D detectors, an avalanche photo diode was used for the detection of the dynamics of the colloidal samples. The signal created by this point detector was subsequently fed into a multitau-correlator, which calculated the normalized intensity autocorrelation function. The slits directly in front of the point detector were set to a size of $50\,\mu\mathrm{m} \times 50\,\mu\mathrm{m}$ to $100\,\mu\mathrm{m} \times 100\,\mu\mathrm{m}$.

To prevent the colloidal samples from beam damage induced by the X-ray beam, a flow-though device was used where the sample was pumped through a quartz capillary with a diameter of 1 mm as sketched in fig. 4.3. The quartz capillary was placed in a sample holder, which also allowed for the mounting of the tantalum guard slits, and placed in the X-ray beam. The capillary was connected via a flexible tube system to a syringe pump, which permitted constant and small flow-rates. The transition time of the colloids in the beam was varied between 1 s and 0.1 s. Apart from the prevention of beam damage, the use of a flow through device allows the measurement and subsequent subtraction of the scattering arising from the dispersion medium and the capillary itself with high precision. To achieve this, the same capillary used for the static and dynamic behavior of a sample was subsequently operated with water and the time-averaged scattering was detected.

5. Experimental Results and Discussion

The experiments have been performed on two systems of charge-stabilized colloidal particles consisting of poly-methyl methacrylate with different particle radii and effective charge. In both systems, the colloidal particles where dispersed in deionised water. The two systems are labeled system PMMA_{542} and system PMMA_{1117} referring to their different particle radius. In the case of system PMMA_{1117}, just the first synthesis step has been performed, while system PMMA_{542} was synthesized performing an additional synthesis step B, a further growth of the colloidal particles, starting from a radius $R \approx 45\,\mathrm{nm}$. The system PMMA_{542} was investigated using mainly static and dynamic light scattering experiments, while system PMMA_{1117} was investigated using mainly X-ray scattering techniques because of its high concentration. System PMMA_{542} has been investigated at five different nominal concentrations, while system PMMA_{1117} was investigated at three different nominal concentrations, which were achieved by either diluting or concentrating a deionised master suspension of the two systems respectively.

Since both systems are highly monodisperse, the samples start to crystallize into highly ordered arrays of particles in the presence of strong direct particle interactions. For charge stabilized systems, this transition to the "solid" phase is depending on the strength of the interaction potential and can thus be varied by the concentration of particles and the screening of the particle interactions. For a deionised suspension of system PMMA_{542}, the phase transition to the solid phase occurred at a volume fraction $\phi \approx 0.003$, while in the case of system PMMA_{1117} crystallization started in deionised samples at volume fractions $\phi \approx 0.25$. The addition of salt to screen the direct particle interactions was therefore always necessary for higher concentrations than the onset of crystallization.

The amount of added salt screening the direct particle interactions has been varied at all concentrations, the characteristics of the individual samples are listed in table 5.1.

5.1. Statics of colloidal particles in solution

The static behavior of the samples was investigated by using either static light scattering or small angle X-ray scattering. In the static light scattering experiments, the scattered intensity was recorded by a point detector for typically 120 s per

Table 5.1.: Dilution factors, nominal salt concentrations and nominal volume fractions ϕ_{nom} of systems PMMA$_{542}$ and PMMA$_{1117}$.

System	Dilution	ϕ_{nom}	Salt$_{\text{nom}}$ [µM]
PMMA$_{542}$	Factor 20	0.001	0, 10
PMMA$_{542}$	Factor 10	0.002	0, 10, 50, 100
PMMA$_{542}$	Factor 5	0.004	5, 10, 50
PMMA$_{542}$	Factor 3	0.008	5, 10, 20, 50
PMMA$_{542}$	Factor 2	0.012	10, 20, 50
PMMA$_{1117}$	Factor 2	0.08	0, 50, 200, 500, 2000, 5000
PMMA$_{1117}$	Factor 1	0.16	0, 10, 35, 100, 500, 1000, 2000, 3500, 5000
PMMA$_{1117}$	Factor 0.5	0.33	100, 200, 350, 3500, 5000, 10000

momentum transfer Q to measure the time averaged intensity. In the case of small angle X-ray scattering, the experiments were performed using a 2D detector. Usually series of 100 to 200 frames of 0.1 s to 1 s acquisition time per frame were taken, the frames were averaged and a dark count value was subtracted. The static data were normalized to the incident flux and to the transmission of the sample. Afterwards, the scattering of the dispersion medium and additional parasitic scattering were subtracted. Finally the images were azimuthally averaged.

5.1.1. Statics of diluted samples

Dilute samples were studied in the concentration regime $\phi < 0.005$, where the direct particle interaction were additionally screened by the addition of electrolyte solution (200 µM for system PMMA$_{542}$ and 500 µM for system PMMA$_{1117}$) to achieve non-interacting samples. The scattered intensity of these samples depends only on shape, number density and electron density contrast of the colloidal particles. To get information about the shape, size and size distribution of the colloidal particles, the scattered intensity was measured in a static small angle X-ray scattering experiment (SAXS) giving access to an increased range of momentum transfers Q as compared to static light scattering experiments.

Fig. 5.1 shows the SAXS result of a dilute colloidal suspension of system PMMA$_{542}$ with screened direct particle interactions. The scattered intensity falls off with increasing Q and the intensity modulation of the formfactor indicates a relatively monodisperse scattering object. The profile can be modeled by the expression for an extended polydisperse sphere (eq. (3.17))

$$I(Q) = BG + I_0 \int_0^\infty dR f(R, R_0, Z) P(Q) \left(\frac{R}{R_0}\right)^6 \tag{5.1}$$

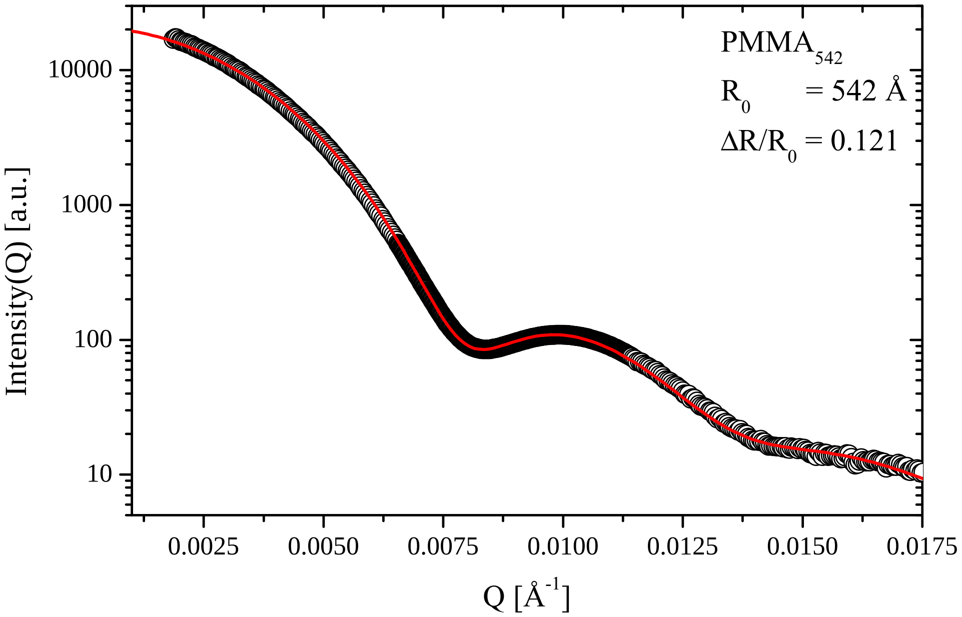

Figure 5.1.: Scattering intensity of a sample of system PMMA$_{542}$ with screened direct particle interactions as a function of the momentum transfer Q. The solid red line is a fit of eq. (5.1) to the data.

Table 5.2.: Average Radius R_0 and polydispersity $\Delta R/R_0$ of the investigated systems.

System	Material	Radius R_0	Polydispersity $\Delta R/R_0$
PMMA$_{542}$	PMMA	542 Å	12.1 %
PMMA$_{1117}$	PMMA	1117 Å	6.7 %

where BG refers to an experimental background, I_0 is an intensity prefactor and $P(Q)$ is the sphere form factor convoluted with the size distribution function $f(R, R_0, Z)$. A fit of eq. (5.1) to the data yields an average radius R_0 of 542 Å and a polydispersity $\Delta R/R_0$ of 12.1 %.

Fig. 5.2 shows the scattering intensity of a non-interacting sample of system PMMA$_{1117}$. In comparison to system PMMA$_{542}$ the positions of the minima are shifted towards smaller momentum transfers, indicating thus that system PMMA$_{1117}$ is made out of bigger particles as compared to system PMMA$_{542}$. A fit of eq. (5.1) to the SAXS data yields a mean radius R_0 of 1117 Å and a polydispersity $\Delta R/R_0$ of 6.7 %. The results are summarized in table 5.2.

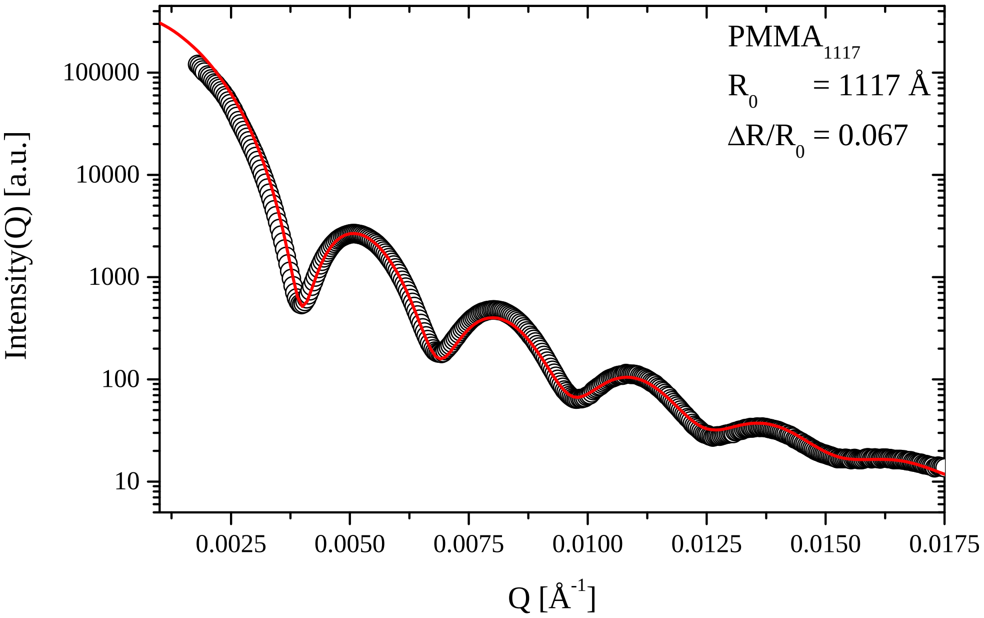

Figure 5.2.: Scattering intensity of sample PMMA$_{1117}$ with screened direct particle interactions as a function of the momentum transfer Q. The solid red line is a fit of eq. (5.1) to the data.

5.1.2. Static description of interacting samples

The scattering intensity is containing information on both the particle form factor $P(Q)$, which describes intra-particle correlations, and the static structure factor $S(Q)$, which describes inter-particle correlations:

$$I(Q) \propto P(Q) \cdot S(Q). \tag{5.2}$$

Fig. 5.3, top panel, shows the scattering intensity of a concentrated sample of system PMMA$_{1117}$ with a nominal volume fraction of $\phi_{\text{nom}} = 0.35$ and a concentration of added electrolyte of 200 µM, where ordering of the colloidal particles in the sample is expected.

The scattered intensity of the sample shows a pronounced peak in the small Q region, not described by the particle form factor. The bottom graph of fig. 5.3 shows the extracted static structure factor of the sample. It was obtained by dividing the scattering intensity of the sample $\langle I(Q)\rangle$ by the scattering intensity of a sample exhibiting no interparticle interactions $\langle I(Q)\rangle_0$ scaled by a prefactor $\alpha \approx N_S/N_0$ where N_S and N_0 are the number of particles in the scattering volumes of the interacting sample and the disordered sample respectively

$$S(Q) = \frac{\langle I(Q)\rangle}{\alpha\langle I(Q)\rangle_0}. \tag{5.3}$$

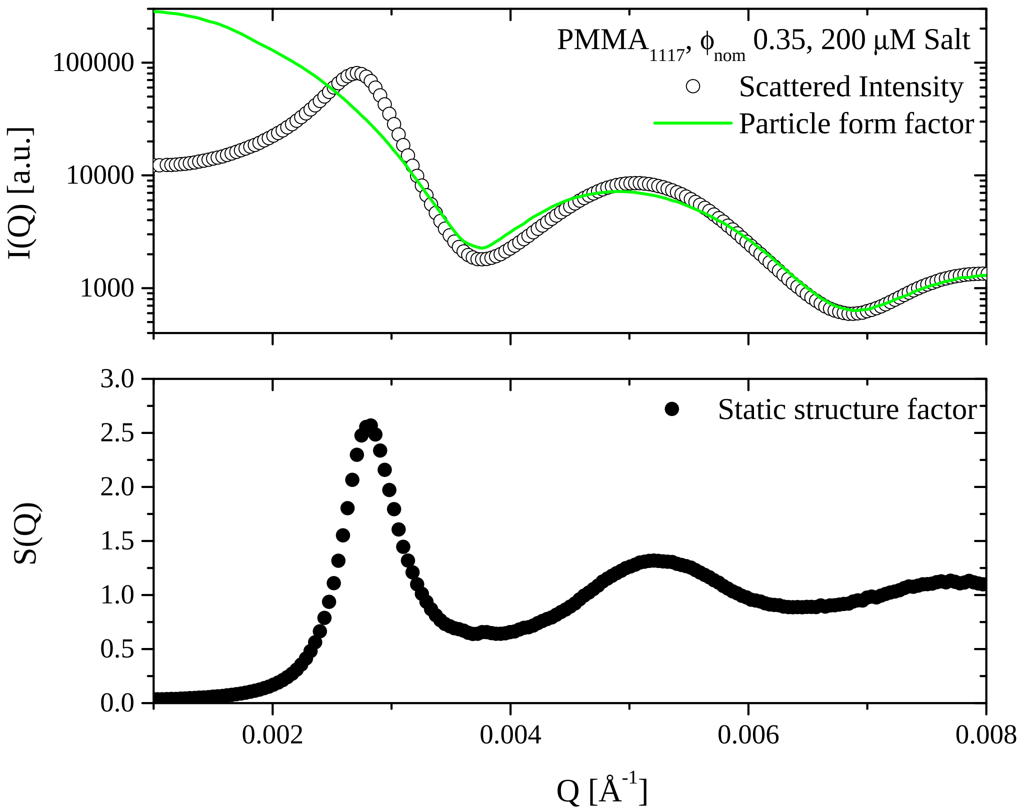

Figure 5.3.: Top: Scattering intensity of an ordered PMMA_{1117} sample with a nominal volume fraction of $\phi_{\text{nom}} = 0.35$ and a concentration of added electrolyte of 200 μM. Bottom: Static structure factor $S(Q)$ as a function of the momentum transfer Q.

The static structure factor shows a pronounced peak at small Q values and oscillates around unity for large momentum transfers.

Fig 5.4 to fig. 5.6 display the extracted static structure factors $S(Q)$ of system PMMA_{542}, measured by static light scattering. The 16 samples were measured at 5 nominal volume fractions $\phi_{\text{nom}} = 0.001$, 0.002, 0.004, 0.008 and 0.012.

The static structure factors for system PMMA_{1117} are shown in fig. 5.7 and fig. 5.8. These are colloidal PMMA particles suspended in water at high volume fractions, measured with small angle X-ray scattering. The nominal volume fractions of the samples ϕ_{nom} were 0.08, 0.16 and 0.33 respectively. To screen direct interparticle interactions, electrolyte solution in different concentrations was added for all of the eight investigated particle concentrations.

The peak of the static structure factor shifts to higher momentum transfers Q with increasing particle concentration, as displayed in fig. 5.9 for the samples with the lowest concentration of added electrolyte at the 5 different nominal volume fractions measured for system PMMA_{542}.

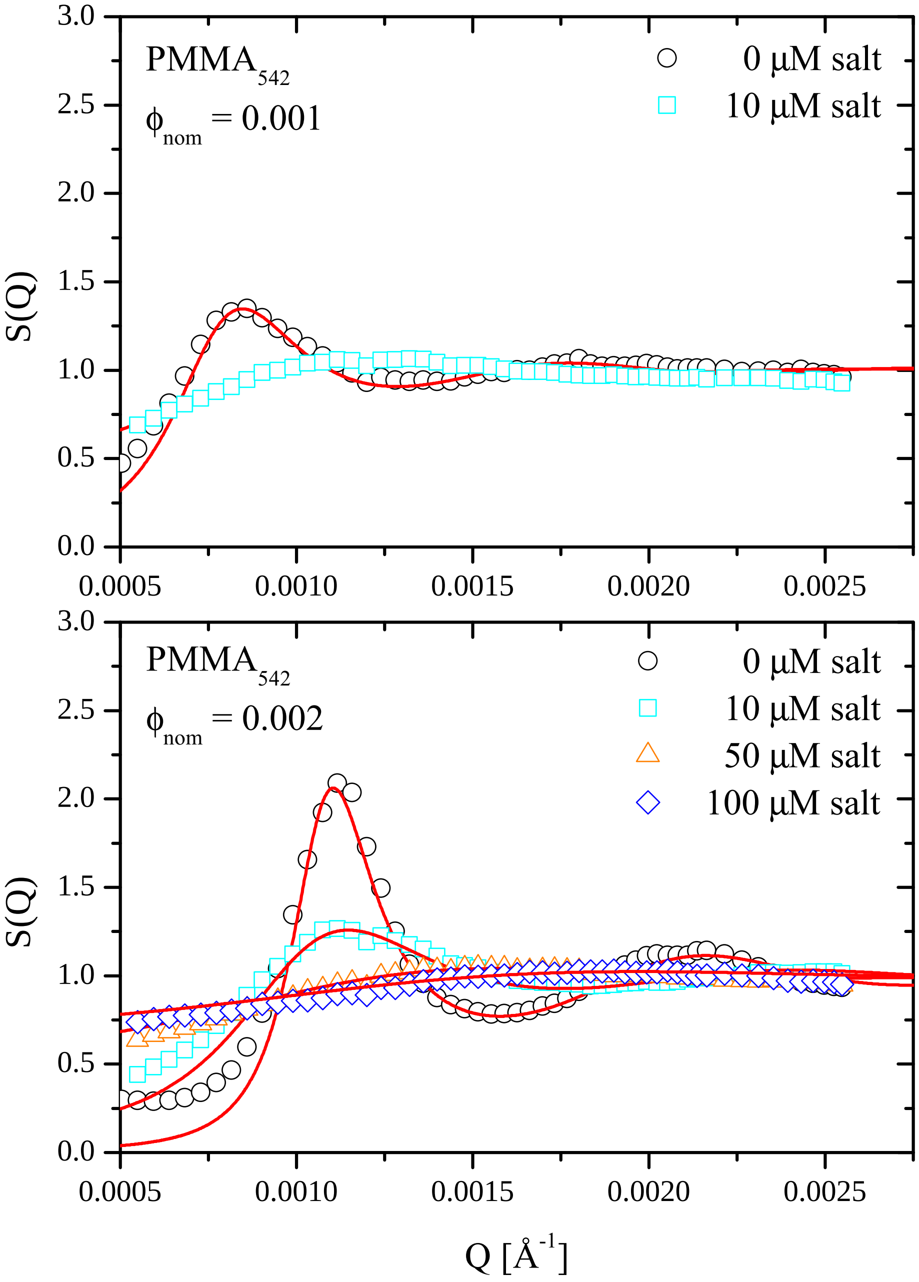

Figure 5.4.: Static structure factors $S(Q)$ of system PMMA$_{542}$ for two nominal volume fractions ϕ_{nom} of 0.001 (top) and 0.002 (bottom). The red lines show RMSA fits with fit parameters ϕ and Z_{eff} to the data.

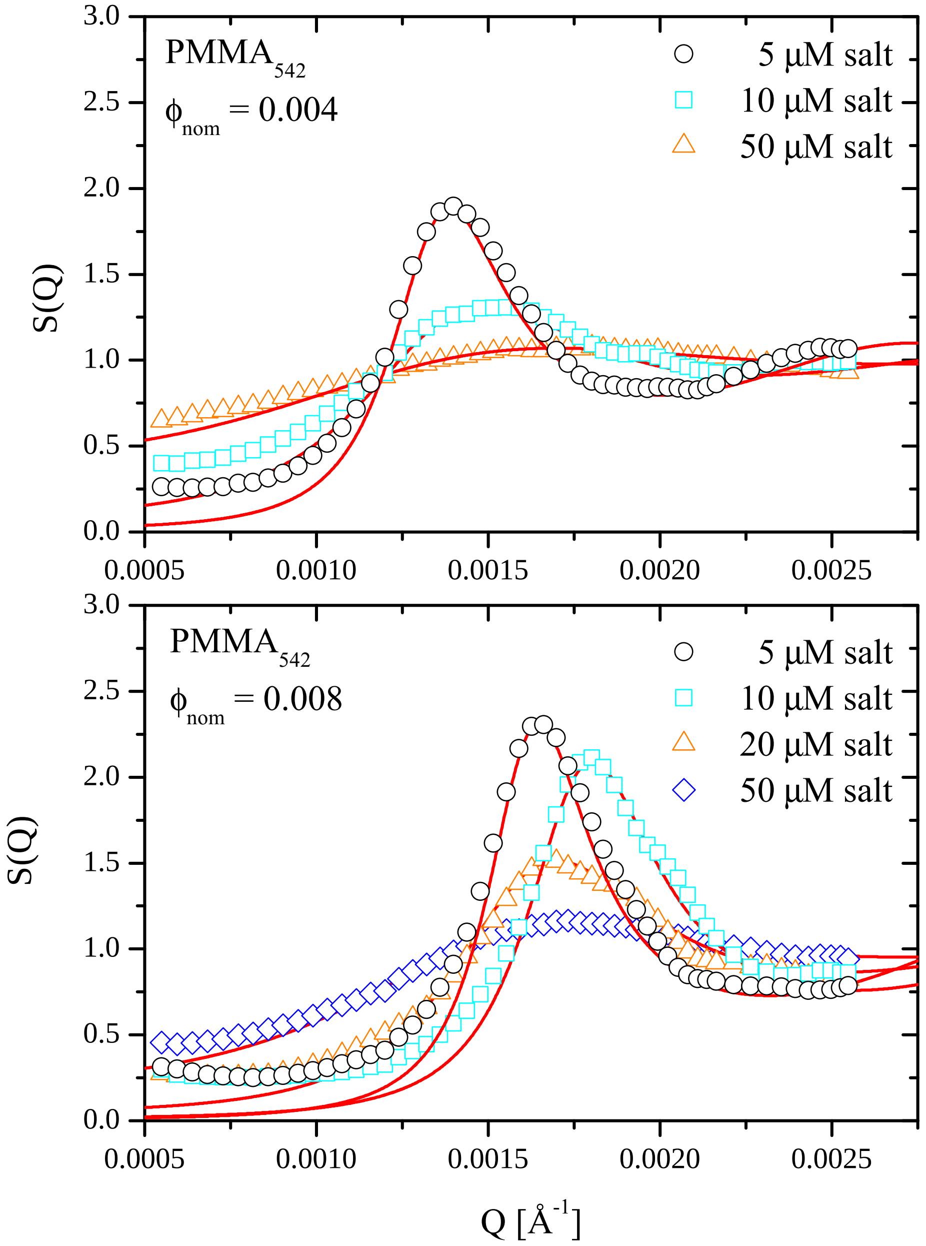

Figure 5.5.: Static structure factors $S(Q)$ of system PMMA$_{542}$ for two nominal volume fractions ϕ_{nom} of 0.004 (top) and 0.008 (bottom). The red lines show RMSA fits with fit parameters ϕ and Z_{eff} to the data.

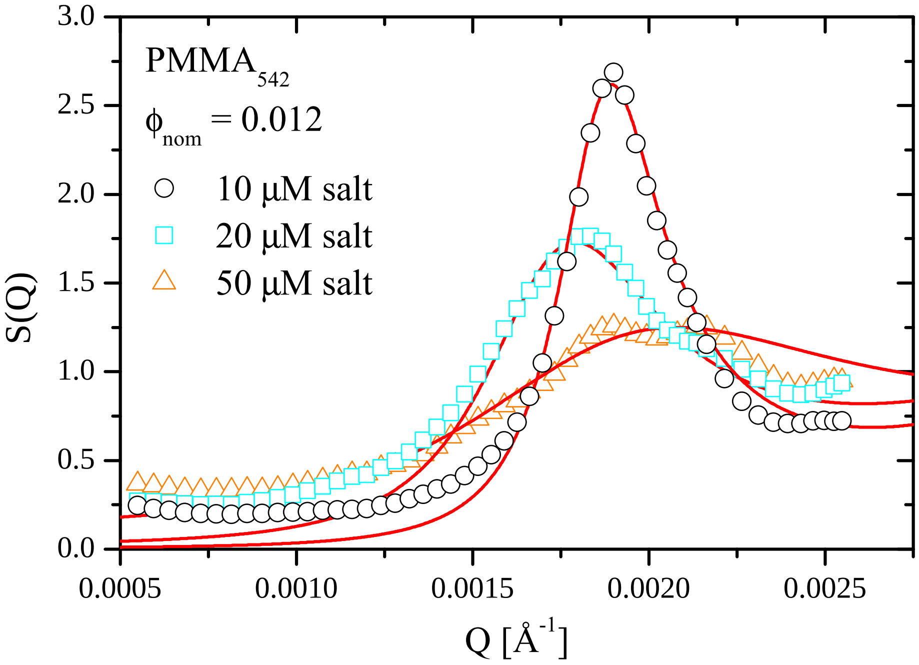

Figure 5.6.: Static structure factors $S(Q)$ of system PMMA$_{542}$ for a nominal volume fraction ϕ_{nom} of 0.012. The red lines show RMSA fits with fit parameters ϕ and Z_{eff} to the data.

This shift of the peak position indicates a compression of the interparticle distance in the suspension with increasing particle concentration, as the position of the first maximum of the static structure factor Q_{max} can be related to the next neighbor distance in the systems via $r_m = 2\pi/Q_{max}$. For sample series measured at the same nominal volume fraction, the position of the peak of the static structure factor Q_{max} shifts to higher Q-values with increasing electrolyte concentration. For the sample series of nominal volume fractions $\phi_{\text{nom}} = 0.008$ (fig. 5.5 (bottom)) and $\phi_{\text{nom}} = 0.012$ (fig. 5.6) deviations from this behavior can be noted, which might be explained by variations of the particle concentration caused by the preparation of the samples.

The height of the static structure peak increases (at a given electrolyte concentration) with increasing volume fraction (see for example the graphs of the two samples at 0 µM and the two samples at 5 µM added salt in fig. 5.9), denoting an increase of the direct interparticle interactions. At a given volume fraction, an increase of the salt concentration is accompanied by a decrease of the peak height of the static structure factor, indicating a screening of the direct particle interactions, as displayed in fig. 5.4 to fig. 5.8. This decrease of the peak height is accompanied by a broadening of the peak shape, indicating a relative relaxation of the particle positions.

The red lines in fig. 5.4 to fig. 5.8 show the corresponding fits of the rescaled mean spherical approximation (RMSA) to the data, which models the direct particle interactions via a screened Coulomb potential (Hayter and Penfold, 1981; Hansen

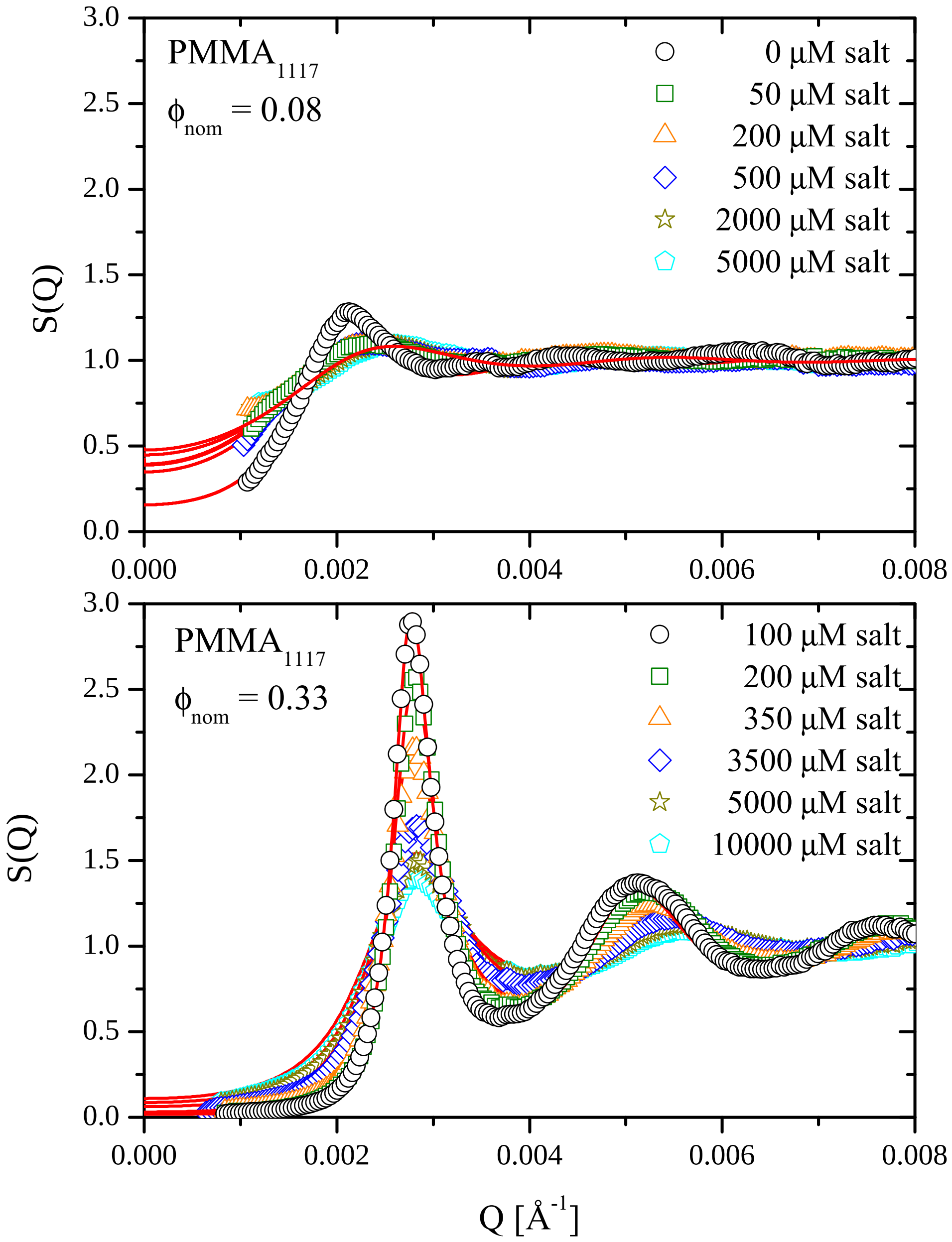

Figure 5.7.: Static structure factors $S(Q)$ of system PMMA$_{1117}$ for two nominal volume fractions ϕ_{nom} of 0.08 (top) and 0.33 (bottom). The red lines show RMSA fits with fit parameters ϕ and Z_{eff} to the data.

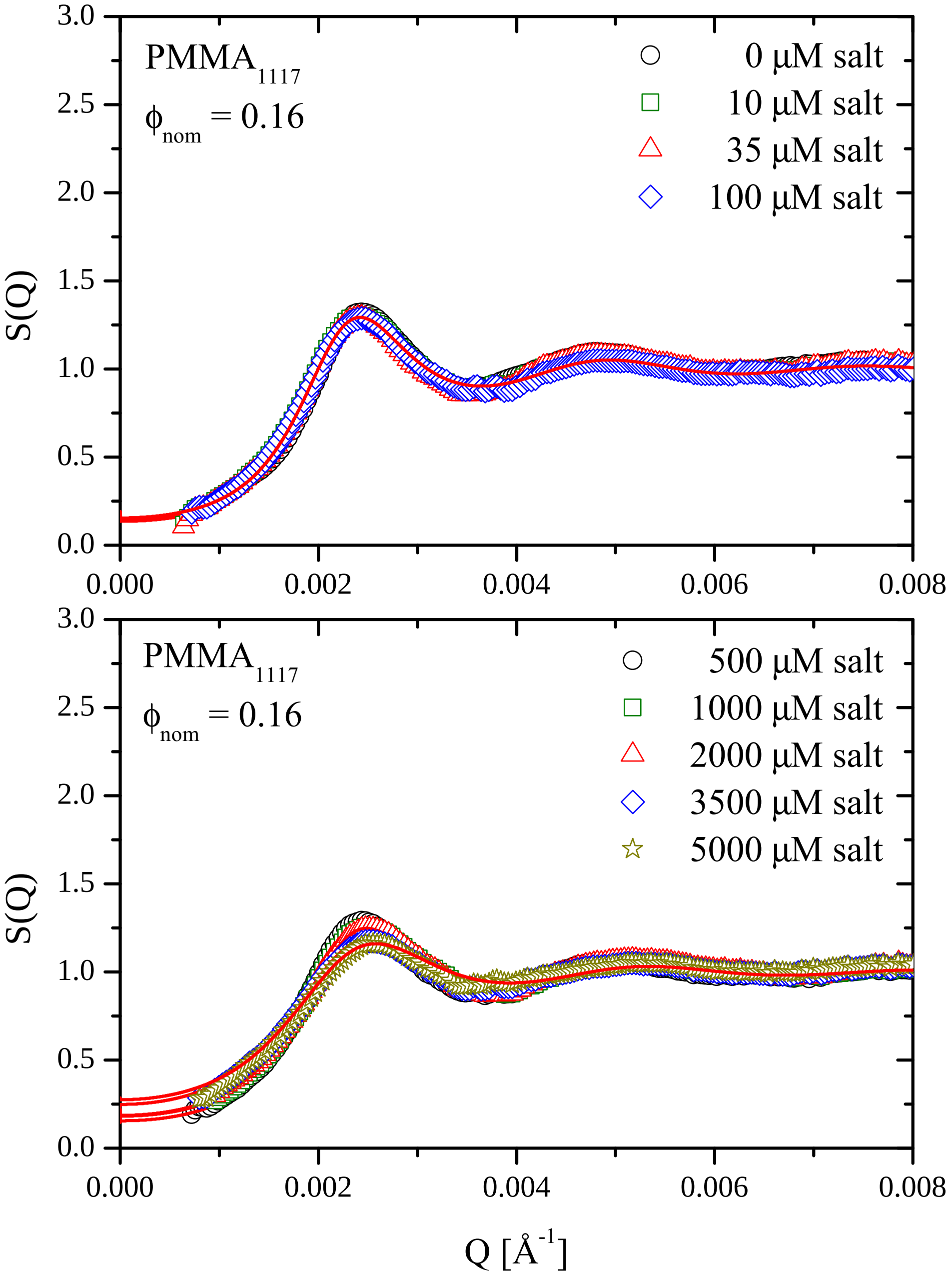

Figure 5.8.: Static structure factors $S(Q)$ of system PMMA$_{1117}$ for a nominal volume fraction ϕ_{nom} of 0.16. The red lines show RMSA fits with fit parameters ϕ and Z_{eff} to the data.

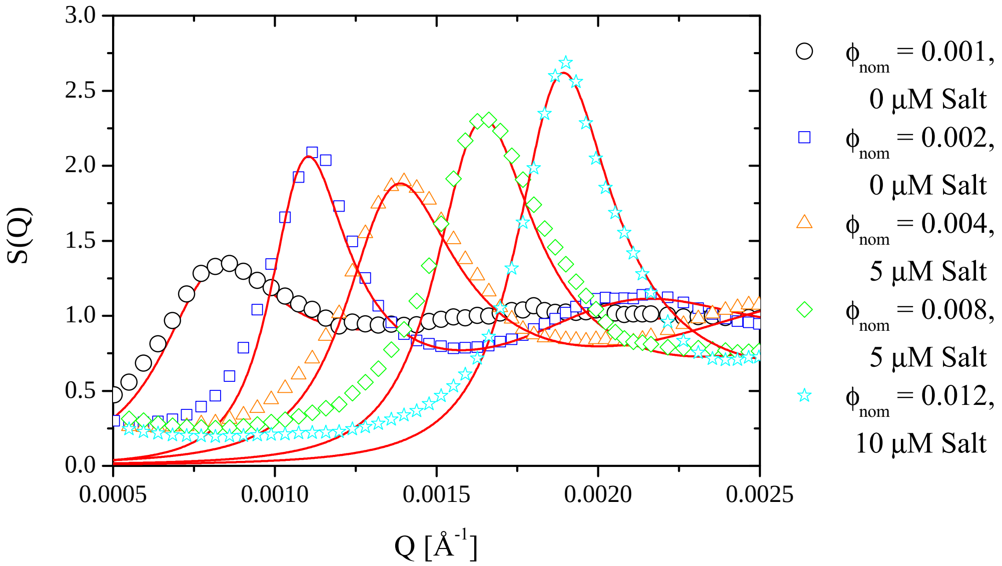

Figure 5.9.: Static structure factors $S(Q)$ of system PMMA$_{542}$ for 5 samples of different nominal volume fractions ϕ_{nom} of 0.001 to 0.012 and the lowest concentration of added salt measured at the respective volume fraction. The red lines show RMSA fits to the data.

and Hayter, 1982). The input parameters for the model were the temperature $T = 293.15\,\text{K}$, the dielectric permittivity of the dispersion medium $\epsilon_r = 80.1$ and the mean radius of the particles with 542 Å and 1117 Å respectively. The model fit evaluates the parameters volume fraction ϕ, concentration of monovalent electrolyte ions and effective charge Z_{eff} of the colloids. As the two parameters electrolyte concentration and effective charge are degenerate and depend on each other (see section 3.2.4), the electrolyte concentrations was also kept constant and set to the value of the nominal salt concentration added to the system. In the case of high salt concentrations, $C_{\text{salt}} \geq 2000\,\mu\text{M}$, the fits were performed using the mean spherical approximation without a rescaling procedure. The results of the model fits to the data are summarized in table 5.3.

In total, the model fits displayed in fig. 5.4 to fig. 5.8 are in good agreement with the measured static structure factors. While the model fits of the static structure factors obtained with small angle X-ray scattering are matching the data points over the whole momentum transfer Q range (fig. 5.7 and fig. 5.8), for the static light scattering data a deviation of the model fit can be seen for small wavevector transfers (fig. 5.4 and fig. 5.5). This might by caused by additional stray light at detector angles close to the directly transmitted laser beam which is not completely removed when subtracting the background scattering. Another reason might be a small amount of impurities of big volume which scatter strongly at small wavevector transfers, causing thus an increase in the background scattering.

Table 5.3.: System, salt concentration, nominal volume fraction ϕ_{nom}, position Q_{max} and height of the static structure factor $S(Q_{max})$ and parameters yielded by a fit of the RMSA model to the static structure factors $S(Q)$. Model parameters were the temperature $T = 293.15\,\text{K}$, the dielectric permittivity of the dispersion medium $\epsilon_r = 80.1$, the salt concentration and the mean radius $R_0 = 542\,\text{Å}$ and $R_0 = 1117\,\text{Å}$ for system PMMA$_{542}$ and PMMA$_{1117}$ respectively.

System	ϕ_{nom}	Salt$_{\text{nom}}$ [µM]	Q$_{\text{max}}$ [Å^{-1}]	S(Q$_{\text{max}}$)	ϕ	Z_{eff} [e^-]
PMMA$_{542}$	0.001	0	0.0009	1.35	0.0010	214
PMMA$_{542}$	0.001	10	0.0012	1.06	0.0010	224
PMMA$_{542}$	0.002	0	0.0011	2.09	0.0027	381
PMMA$_{542}$	0.002	10	0.0011	1.26	0.0021	461
PMMA$_{542}$	0.002	50	0.0015	1.05	0.0016	706
PMMA$_{542}$	0.002	100	0.0019	1.03	0.0018	747
PMMA$_{542}$	0.004	5	0.0014	1.89	0.0052	432
PMMA$_{542}$	0.004	10	0.0016	1.31	0.0052	267
PMMA$_{542}$	0.004	50	0.0017	1.08	0.0030	572
PMMA$_{542}$	0.008	5	0.0017	2.31	0.0089	487
PMMA$_{542}$	0.008	10	0.0018	2.11	0.0115	497
PMMA$_{542}$	0.008	20	0.0017	1.52	0.0084	510
PMMA$_{542}$	0.008	50	0.0017	1.16	0.0053	722
PMMA$_{542}$	0.012	10	0.0019	2.69	0.0135	710
PMMA$_{542}$	0.012	20	0.0018	1.76	0.0106	602
PMMA$_{542}$	0.012	50	0.0021	1.26	0.0112	483
PMMA$_{1117}$	0.08	0	0.00213	1.28	0.142	75
PMMA$_{1117}$	0.08	50	0.00236	1.10	0.087	69
PMMA$_{1117}$	0.08	200	0.00236	1.09	0.077	149
PMMA$_{1117}$	0.08	500	0.00236	1.10	0.080	320
PMMA$_{1117}$	0.08	2000	0.00252	1.09	0.086	403
PMMA$_{1117}$	0.08	5000	0.00263	1.09	0.093	856
PMMA$_{1117}$	0.16	0	0.00244	1.32	0.218	98
PMMA$_{1117}$	0.16	10	0.00244	1.30	0.193	82
PMMA$_{1117}$	0.16	35	0.00244	1.29	0.178	101
PMMA$_{1117}$	0.16	100	0.00244	1.29	0.169	143
PMMA$_{1117}$	0.16	500	0.00244	1.29	0.160	429
PMMA$_{1117}$	0.16	1000	0.00248	1.26	0.158	523
PMMA$_{1117}$	0.16	2000	0.00248	1.25	0.158	644
PMMA$_{1117}$	0.16	3500	0.00255	1.17	0.147	674
PMMA$_{1117}$	0.16	5000	0.00255	1.16	0.145	766
PMMA$_{1117}$	0.33	100	0.00276	2.89	0.360	325
PMMA$_{1117}$	0.33	200	0.00280	2.57	0.365	349
PMMA$_{1117}$	0.33	350	0.00280	2.15	0.341	364
PMMA$_{1117}$	0.33	3500	0.00280	1.70	0.325	864
PMMA$_{1117}$	0.33	5000	0.00280	1.50	0.315	665
PMMA$_{1117}$	0.33	10000	0.00280	1.40	0.298	560

The resulting values for the effective charge Z_{eff} show overall an increase with increasing volume fraction for both systems, while at a given nominal volume fraction an increase with increasing concentration of added electrolyte can be observed. The obtained volume fractions show some deviation from the nominal values, but are in relatively good agreement with the nominal values. For the three nominal volume fractions of system PMMA_{1117} a slight decrease of the extracted volume fraction with increasing salt concentration can be observed.

For all nominal volume fractions, the height of the first maximum of the static structure structure $S(Q_{max})$ is decreasing with increasing electrolyte concentration as expected for an enhanced screening of the direct particle interactions. It is surprising that the peak values $S(Q_{max})$ for the two series at ϕ_{nom} of 0.08 and 0.16 show only small changes upon changes of the salt concentration.

During data evaluation it was found that when the RMSA model was applied to the static structure factors by assuming a constant effective charge Z_{eff} of $496\,\text{e}^-$ (PMMA_{542}) and $221\,\text{e}^-$ (PMMA_{1117}) per colloid good fits were achieved. By keeping the effective charge of the colloidal particles constant, the RMSA model returns the strength of the interaction potential as a function of the amount of added ions screening the interparticle interactions. The obtained fits were of similar quality to the fits shown in fig. 5.4 to fig. 5.8; the obtained parameters are given in appendix B.

For system PMMA_{542}, the obtained values for the concentration of added electrolyte correspond well to the nominal salt concentration. For system PMMA_{1117} the obtained salt concentrations with the RMSA model show discrepancies to the nominal concentrations of additional monovalent salt ions. While the fits display the overall feature of an increasing salt concentration in all of the three series, the absolute values differ. The volume fractions obtained by the fits differ only slightly from the volume fractions shown in table 5.3. The only two exceptions are the two volume fractions $\phi_{\text{nom}} = 0.08$ and $\phi_{\text{nom}} = 0.16$ at $0\,\mu\text{M}$ salt, which are $\approx 20\,\%$ smaller in the case of a constant effective charge Z_{eff}.

Note that the further extraction of the dynamics and hydrodynamics are independent of the modelization of the static structure factor, since the measured static behavior of the system has been used as input for dynamics modeling.

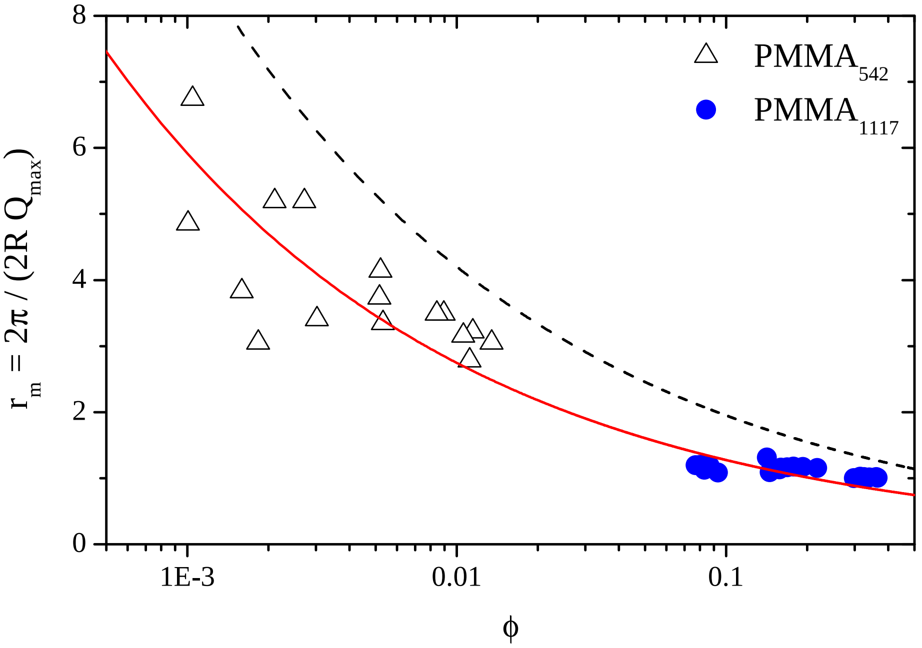

Figure 5.10.: Mean interparticle spacing r_m normalized to the particle diameter $2R$ as a function of the volume fraction ϕ. The dashed line shows the maximal geometrical distance for a system of spheres on the positions of a simple cubic lattice, the solid red line is a fit of the maximal geometrical distance times a constant (0.65) to the data.

5.1.3. Discussion of the static behavior

The time-averaged scattering of ultra-dilute samples of both systems could be modeled by a spherical particle form factor, which yielded a mean radius of 542 Å and 1117 Å and a polydispersity $\Delta R/R_0$ of 0.12 and 0.07 for system PMMA_{542} and system PMMA_{1117} respectively. The higher polydispersity of system PMMA_{542} is correlated to the smaller size of the colloidal particles, since the polydispersity is found to decrease for poly-methyl methacrylate particles with increasing radius of the particles (Pusey, 1991).

At higher concentrations (volume fractions from 0.001 to 0.33) an ordering of the samples was observed and described by a static structure factor $S(Q)$ that deviates from unity. The extracted static structure factors $S(Q)$ were modeled using the rescaled mean spherical approximation (RMSA) giving information on the volume fraction and the effective charge of the particles.

The position of the static structure peak is related to the mean interparticle spacing $r_m \approx 2\pi/Q_{max}$. To compare the two systems, the mean interparticle spacing is divided by the diameter of the colloidal particles $2R$. In fig. 5.10 the normalized mean interparticle spacing r_m is shown as a function of the volume fraction ϕ as determined by a fit of the RMSA model to the data.

The mean interparticle spacing decreases with increasing volume fraction, as expected for the evolution of a more compressed system with increasing volume fraction. For the most concentrated system of $\phi_{\mathrm{nom}} = 0.33$, the mean interparticle distance is getting close to unity. An upper limit for the mean interparticle spacing as a function of the volume fraction is given by the mean geometrical distance between the colloidal particles, which depends on the number density n and is proportional to $n^{-1/3}$. The dashed line in fig. 5.10 is the mean geometrical distance for a system of spheres placed on positions of a simple-cubic lattice. The mean interparticle spacing of all samples is below the mean geometric distance, as expected since the simple-cubic lattice corresponds to a packing factor (or volume fraction) of 0.52. The solid red line is a fit of the maximal geometric distance scaled by a constant factor (× 0.65) to the data. The agreement is reasonable, however deviations are displayed. The mean interparticle spacing of samples of the lowest volume fraction ($\phi_{\mathrm{nom}} = 0.08$) of system PMMA$_{1117}$ are below the mean value, indicating a less dense packing of the particles. In contrast, the mean interparticle distance of samples of the highest nominal volume fraction ($\phi_{\mathrm{nom}} = 0.33$) are all more dense packed than the average value. This observation is in agreement with the strength of the interparticle interactions, displayed by the peak values of the static structure factor $S(Q_{max})$ (table 5.3), which are for all samples of $\phi_{\mathrm{nom}} = 0.33$ higher than for the samples of $\phi_{\mathrm{nom}} = 0.08$, resulting in a denser packing of the spherical particles.

The second factor influencing the mean interparticle distance is the amount of added electrolyte, which screens the interparticle interactions. The evolution of the mean interparticle spacing with increasing concentrations of added electrolyte is shown in fig. 5.11.

The mean interparticle spacing shows a slight decrease with increasing electrolyte concentration for the eight nominal volume fractions. This behavior corresponds to a relaxation of the system with decreasing direct particle interactions, as the positions of particles surrounding another particle start to relax.

The low momentum transfer Q limit $S(Q \to 0)$ is a measure of the isothermal compressibility χ_T as $\chi_T \propto S(0)$ (see eq. (3.21)). The value of $S(0)$ can be extracted by a linear extrapolation of the static structure factor as a function of Q^2 (eq. (3.22)). As the static structure factors measured by static light scattering show a strong influence of stray light at small momentum transfers, this extrapolation has only been performed for the small angle X-ray scattering data. To evaluate the $S(0)$ values of the light scattering data, the corresponding fits of the RMSA model to the data have been extracted for $Q = 0$. The values of $S(0)$ as a function of the volume fraction are plotted in fig. 5.12. For the static structure factors measured with static light scattering, the $S(0)$ values have been extracted from RMSA model fits to the data.

The values of S(0) decrease with increasing volume fraction for both systems, corresponding to an increased compression of the two systems. A similar behavior holds for a hard sphere system, for which the values have been obtained by calculating $S(Q = 0)$ of a theoretical hard sphere structure factor using the Percus Yevick approximation. Apart from two exceptions at the highest salt concentration

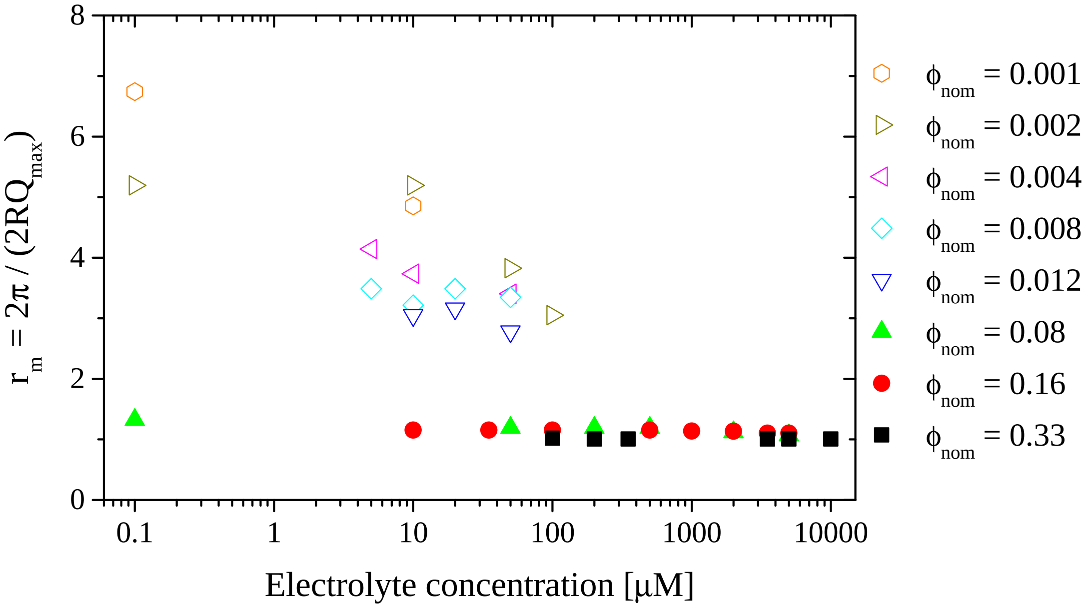

Figure 5.11.: Mean interparticle distance r_m normalized to the particle diameter $2R$ as a function of the electrolyte concentration of the eight nominal volume fractions. Filled symbols refer to system $PMMA_{1117}$, open symbols refer to system $PMMA_{542}$. The samples at a nominal salt concentration of 0 µM have been plotted at 0.1 µM, corresponding to the self dissociation of the dispersion medium water at a neutral pH of 7.

of $\phi_{\text{nom}} = 0.08$, the values obtained from an extrapolation of the data for $S(0)$ are smaller when compared to the hard sphere behavior, indicating a stronger compression of the systems due to the electrostatic interactions. In addition, the samples show an increase of $S(0)$ at a given volume fraction with increasing salt concentration. The S(0) behavior is an indicator of the type of interactions. As repulsive systems have a tendency to withstand compression, the values of S(0) are often rather close to 0. As expected, all values are smaller than unity. Moreover, the interaction strength of the repelling forces are for most samples bigger than expected for a hard sphere system. Just in the case of two samples (at a nominal volume fraction $\phi_{\text{nom}} = 0.08$) the measured $S(0)$ is bigger than for a hard sphere system of corresponding volume fraction ϕ.

The evolution of the peak value of the static structure factor with increasing volume fraction is shown in fig. 5.13 (top). For both systems, a trend towards higher peak values of $S(Q)$ with increasing volume fraction can be seen. The maximum peak height $S(Q_{max})$ is below the onset of crystallization at a peak height of 2.85 for all samples except one sample at $\phi_{\text{nom}} = 0.33$ where $S(Q_{max}) = 2.89$. The onset for crystallization can be shifted up to a peak value of $S(Q_{max}) = 3.1$ in the case of low-salinity systems of strongly interacting charge stabilized systems (Gapinski *et al.*, 2010), which is the case for the respective sample. As the sample showed additionally

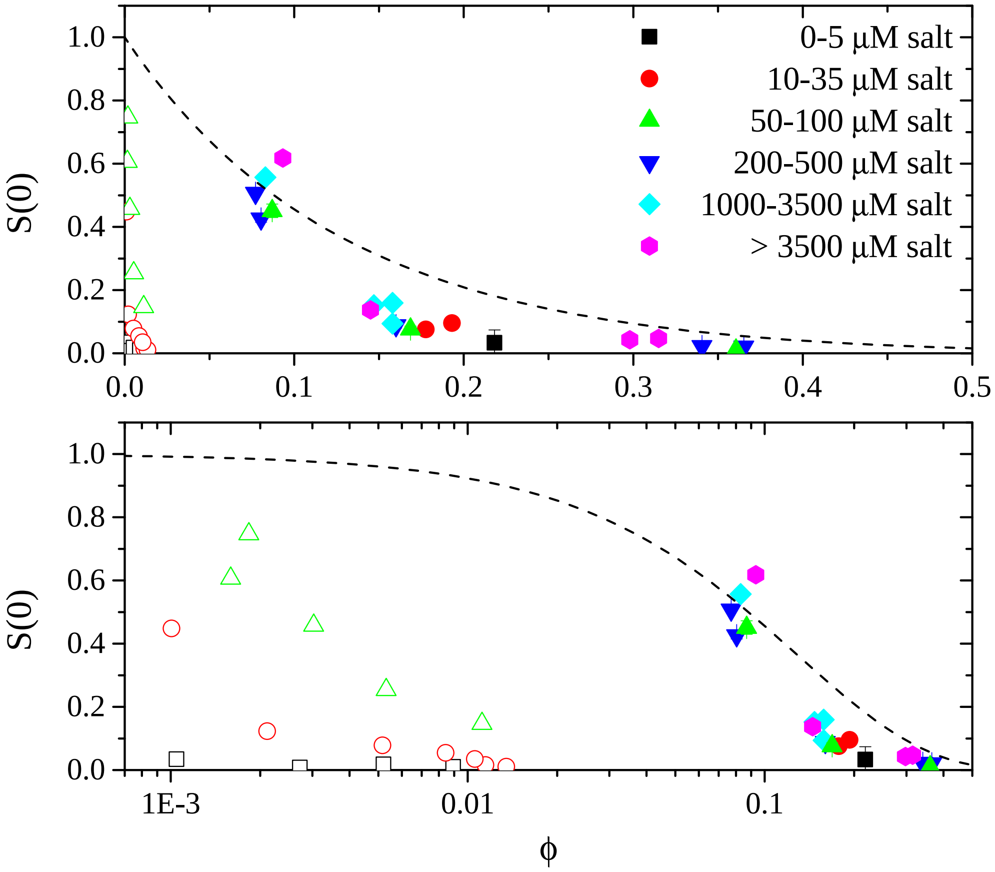

Figure 5.12.: Extrapolated values of the static structure factor $S(0)$ as a function of the volume fraction ϕ. Filled symbols refer to system PMMA_{1117}, open symbols refer to system PMMA_{542}. The volume fraction is plotted on a linear scale in the top graph, and on a logarithmic scale on the bottom graph. The dashed lines represent the behavior of a hard sphere system.

no signs of crystallization in the scattered intensity, all samples can be considered to be in the fluid phase.

Since the peak height is additionally depending on the electrolyte concentration of the system, the middle and bottom part of fig. 5.13 display the evolution of the peak value $S(Q_{max})$ for both systems individually depending on the salt concentrations. A binning of all samples of one nominal volume fraction to the respective mean volume fraction has been performed, the error bars indicate the difference between the individual and the mean volume fraction of the samples.

The static structure factors show a clear decrease with increasing salt concentration, as expected for an enhanced screening of the direct particle interactions with increasing ionic strength of the dispersion medium. This trend can be clearly observed for all sample series investigated, as displayed in fig. 5.14. The decrease of the peak

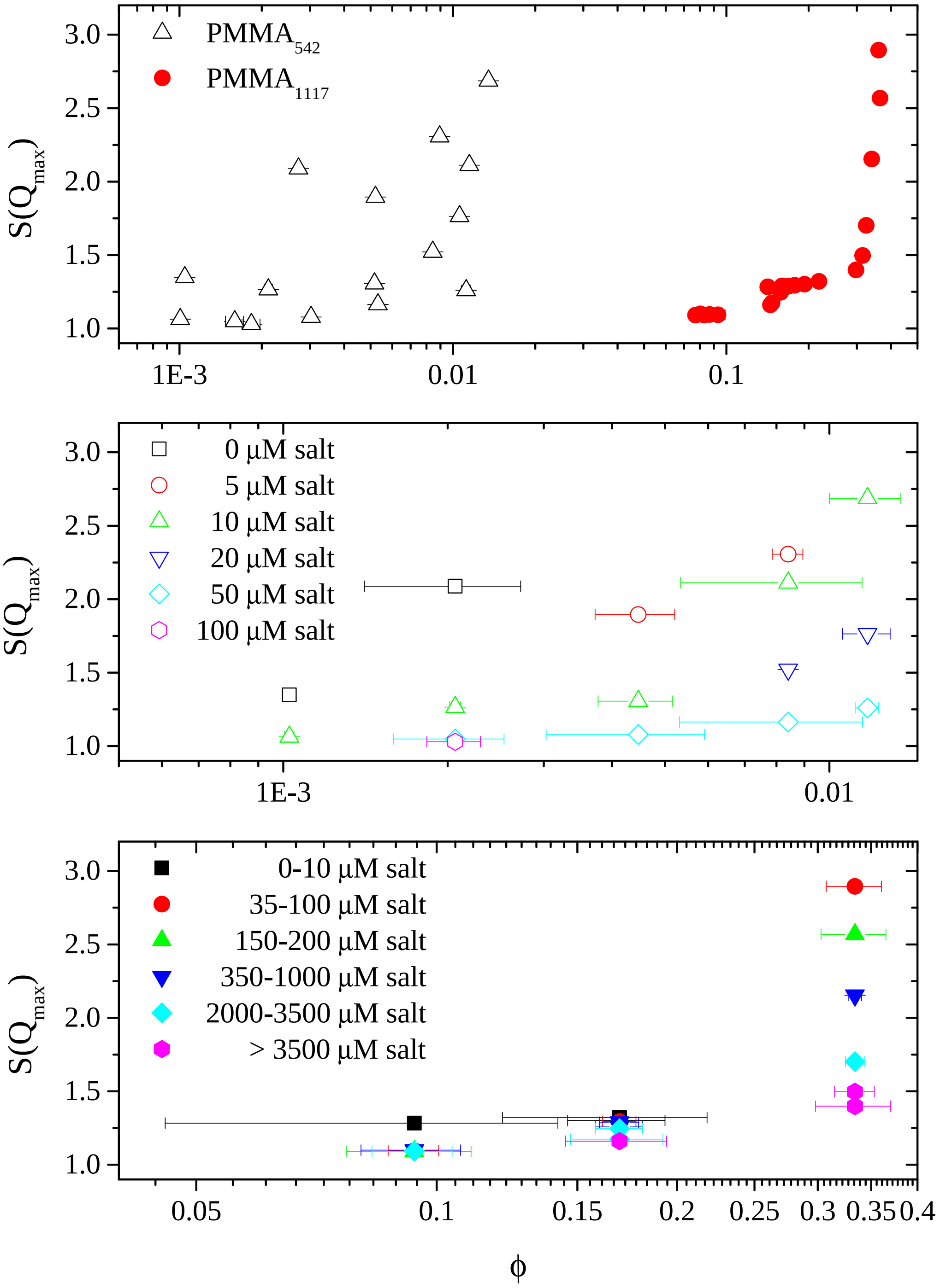

Figure 5.13.: Peak value of the static structure factor $S(Q_{max})$ as a function of the volume fraction. Top: Both System, the volume fraction of the samples is the result from the RMSA fit. Middle: System PMMA$_{542}$, the volume fraction of the samples shown is the average volume fraction of all samples of one nominal volume fraction, the error bars indicate the difference between average and sample volume fraction yielded by RMSA model. Bottom: System PMMA$_{1117}$, the displayed volume fractions are similarly obtained as for system PMMA$_{542}$.

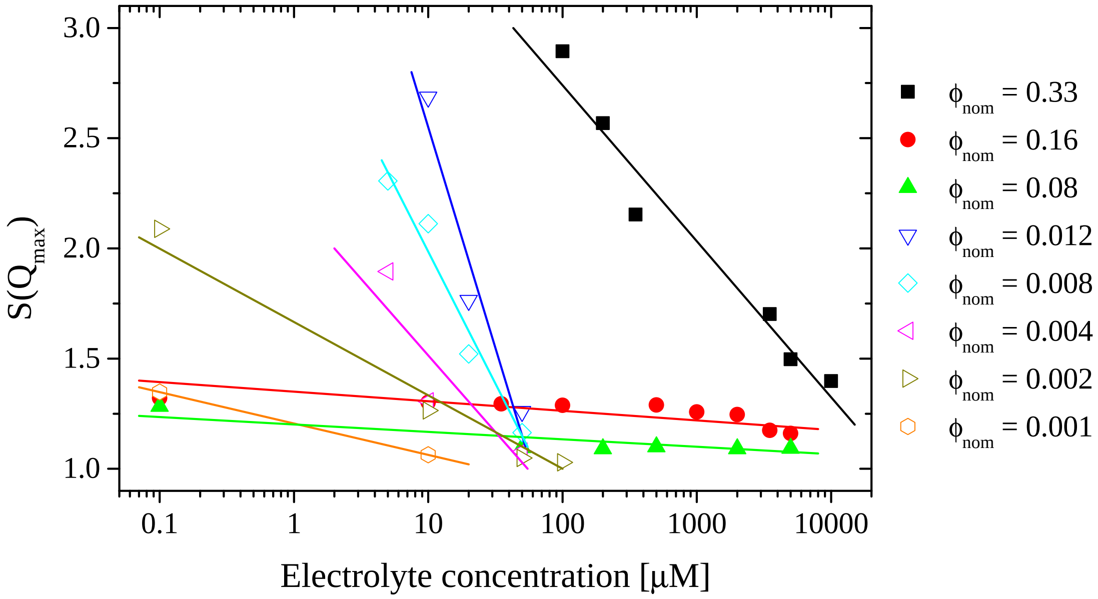

Figure 5.14.: Peak value of the static structure factor $S(Q_{max})$ as a function of the electrolyte concentration. The different colors indicate the 8 different nominal volume fractions, the solid lines are guides to the eye. Filled symbols refer to system PMMA_{1117}, open symbols refer to system PMMA_{542}. The samples at a nominal salt concentration of 0 µM have been plotted at 0.1 µM, corresponding to the self dissociation of the dispersion medium water at a neutral pH-value of 7.

value $S(Q_{max})$ as a function of the salt concentration is more pronounced for the sample series at higher volume fractions for system PMMA_{542} ($0.001 \leq \phi_{\mathrm{nom}} \leq 0.012$). The same trend can be seen for system PMMA_{1117} when comparing the samples of $\phi_{\mathrm{nom}} = 0.33$ to the samples of $0.08 \leq \phi_{\mathrm{nom}} \leq 0.16$.

The RMSA fits to the static structure factor $S(Q)$ yield the effective charge Z_{eff} and the volume fractions of the individual samples. For the two highest concentrations, $\phi_{\mathrm{nom}} = 0.16$ and 0.33, the fit shows a tendency towards lower volume fractions for increasing salt concentrations as listed in table 5.3

The effective charge Z_{eff} as extracted by the RMSA model shows a trend towards higher effective charges with increasing salt concentration as displayed in fig. 5.15.

For both systems PMMA_{542} and PMMA_{1117} a similar behavior can be observed: While the effective charge is increasing slowly at small salt concentrations, the increase becomes steeper for higher concentrations of added electrolyte. For the eight volume fractions investigated here, it can be observed that this transition to a faster increase of the effective charge occurs at smaller concentrations of added electrolyte with decreasing volume fractions. A similar effect has been observed by *Gapinski et al.* (Gapinski *et al.*, 2009), who attribute this behavior to a transition from an counterion dominated to a salt ion dominated screening when the number

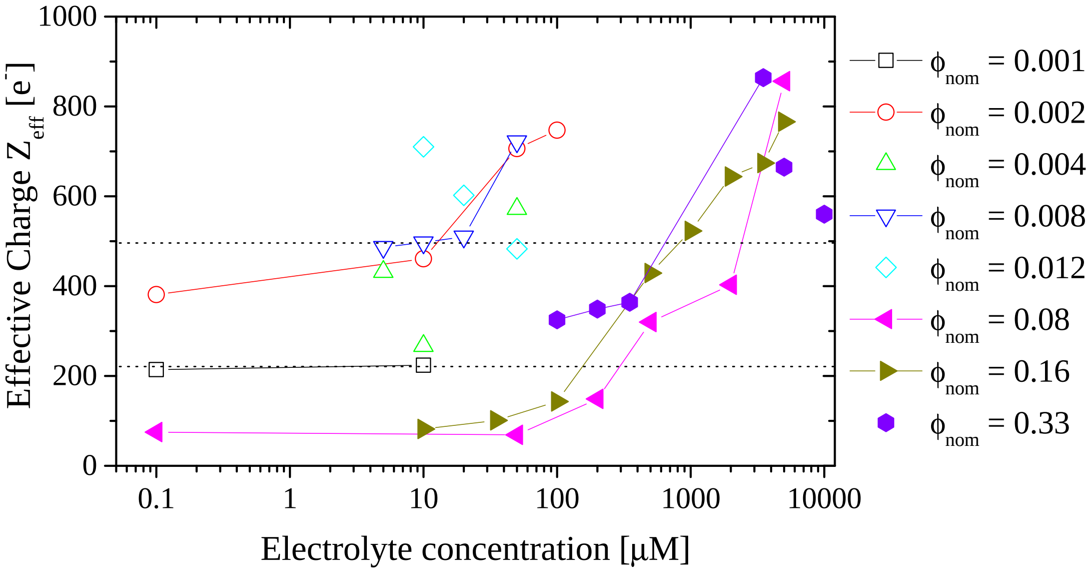

Figure 5.15.: Evolution of the effective charge Z_{eff} yielded by the RMSA model fits to the data as a function of electrolyte concentration. Filled symbols refer to system PMMA_{1117}, open symbols refer to system PMMA_{542}. The samples at a nominal salt concentration of 0 µM have been plotted at 0.1 µM corresponding to the self dissociation of the dispersion medium water at a neutral pH-value of 7. The dotted lines indicate the constant effective charge $Z_{\mathrm{eff}} = 496\,\mathrm{e}^-$ and $221\,\mathrm{e}^-$ for system PMMA_{542} and PMMA_{1117} respectively.

of salt ions exceeds the number of counterions with increasing salt concentration. This change of the screening behavior explains in addition the shift of the transition to smaller amounts of added electrolyte concentrations with decreasing volume fraction, as the concentration of counterions decreases similarly.

5.2. Dynamics of colloidal particles in suspensions

To investigate the dynamics of colloidal particles in solution, photon correlation spectroscopy experiments using coherent light were performed. While it is possible to probe dilute or semi-dilute samples with visible light, more concentrated samples are often opaque. Therefore X-rays with their high penetration depth were used for the determination of the dynamics of moderate to strongly concentrated systems. To deduce the dynamics of a colloidal suspension, the temporal changes of the recorded scattered interference pattern (speckle pattern) are analyzed by means of the normalized intensity autocorrelation function $g_2(Q,\tau)$ as a function of the momentum transfer Q given by

$$g_2(Q,\tau) = \beta(Q)\exp(-2\Gamma(Q)\tau) + 1. \tag{5.4}$$

Here, β denotes the speckle contrast at a given momentum transfer Q and $\Gamma(Q)$ is the momentum transfer dependent relaxation rate related to the effective short-time diffusion coefficient $D(Q)$ by

$$\Gamma(Q) = D(Q) \cdot Q^2. \tag{5.5}$$

5.2.1. Dynamics of non interacting colloidal suspensions

In the absence of interparticle interactions, the diffusive motion of a colloidal particle is unaffected by other particles. Therefore the dynamics is independent of the probed length scale and $D(Q) = D_0$ for all momentum transfers Q.

The normalized intensity autocorrelation functions for six different momentum transfers Q are shown in fig. 5.16. With increasing wavevector transfer Q the exponential decay of the intensity autocorrelation functions is shifting towards smaller lag times τ, corresponding to a faster decay of the correlations in the sample on the corresponding smaller length scales investigated.

To probe the free diffusion coefficient D_0, ultra-dilute samples of volume fraction $\phi < 0.001$, with completely screened interparticle interactions (100 µM for both systems PMMA_{542} and PMMA_{1117}) were measured at different wavevector transfers Q. The short-time regime of the recorded normalized intensity autocorrelation functions were fitted using eq. (5.4). In fig. 5.17 the extracted relaxation rates $\Gamma(Q)$ are shown as a function of the square of the momentum transfer Q^2 for the two systems PMMA_{542} and PMMA_{1117}. The intensity autocorrelations of system PMMA_{542} show a faster decay compared to system PMMA_{1117} at similar momentum transfers Q as can be seen by the higher values of the corresponding relaxation rates $\Gamma(Q)$.

A fit of eq. (5.5) to the data yields the free diffusion coefficient D_0 for the two systems, shown in table 5.4. The hydrodynamic radius of the particles can be

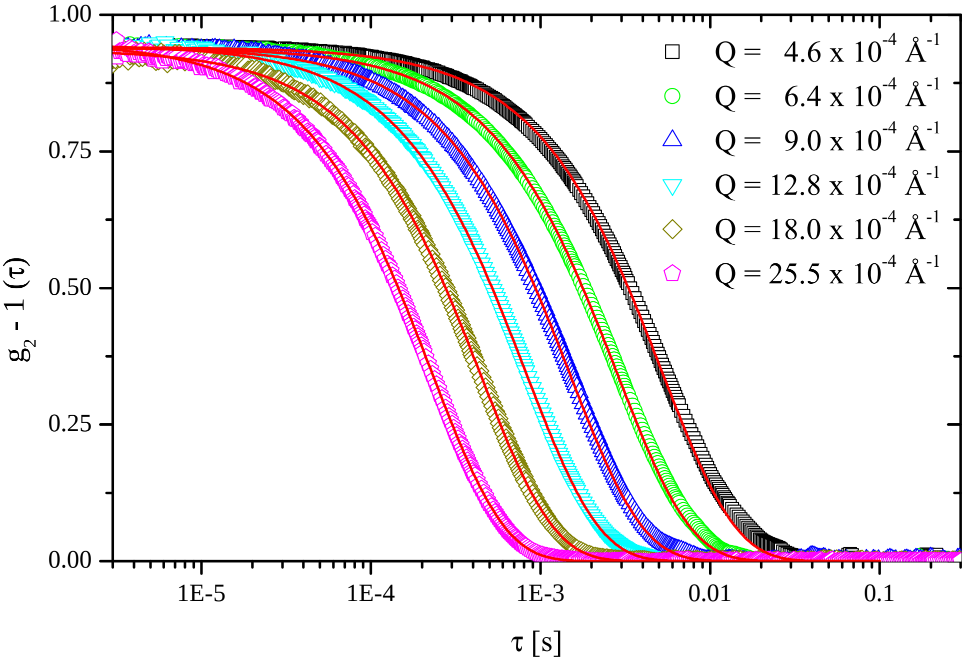

Figure 5.16.: Normalized intensity autocorrelation functions $g_2 - 1(\tau)$ as a function of the lag time τ. The autocorrelation functions have been detected at the wavevector transfers $Q = 4.6 \times 10^{-4}$ Å^{-1}, 6.4×10^{-4} Å^{-1}, 9.0×10^{-4} Å^{-1}, 1.3×10^{-3} Å^{-1}, 1.8×10^{-3} Å^{-1} and 2.5×10^{-3} Å^{-1}. The red lines show fits of eq. (5.4) to the data.

Table 5.4.: Hydrodynamic radius R_H, geometrical radius R_0 extracted by a fit of a sphere form factor to the time-averaged scattering intensity of a dilute sample (table 5.2) and free diffusion coefficient D_0 of the investigated systems.

System	Hydrodynamic radius R_H [Å]	Geometrical radius R_0 [Å]	D_0 [$\mathrm{m^2/s}$]
PMMA$_{542}$	614	542	$3.49 \cdot 10^{-12}$
PMMA$_{1117}$	1128	1117	$1.90 \cdot 10^{-12}$

calculated using eq. (2.10) assuming a dynamic viscosity of $1.002 \cdot 10^{-3}\,\mathrm{kg/ms}$ for the dispersion medium water at a temperature of 293.15 K.

The hydrodynamic radius is 614 Å and 1128 Å for system PMMA$_{542}$ and PMMA$_{1117}$ respectively. For both samples, the hydrodynamic radius is bigger than the geometrical radius R_0 derived from the particle form factor model fit to the static scattering data. This can be partially attributed to a layer of solvent molecules and counter ions which move together with the colloidal particles in the suspension (Pecora, 2000).

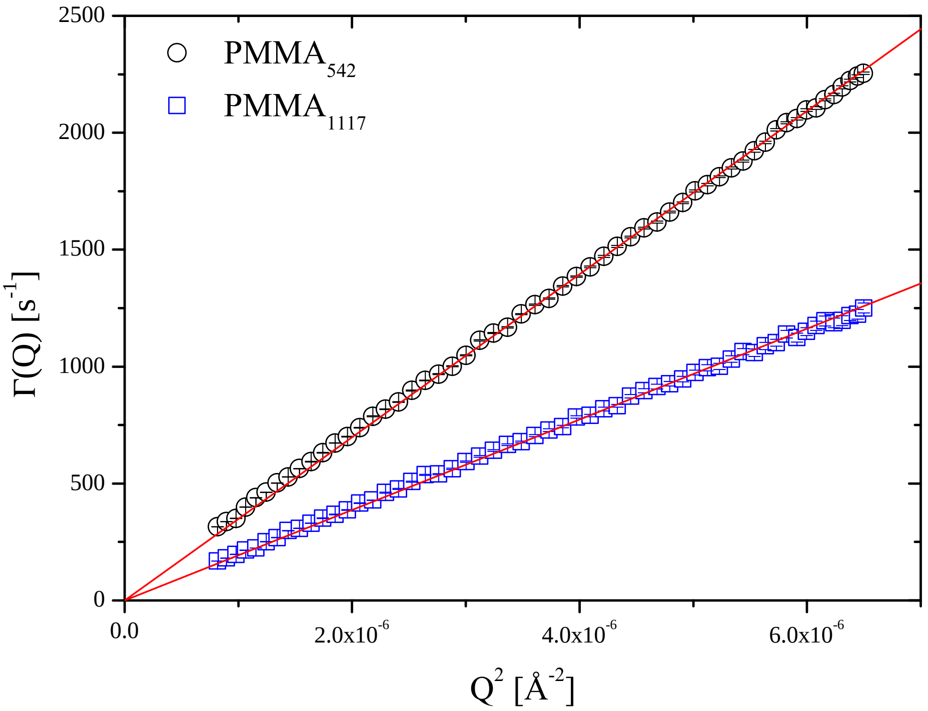

Figure 5.17.: Relaxation rate $\Gamma(Q)$ as a function of the squared momentum transfer Q^2 for two samples of systems PMMA$_{542}$ and PMMA$_{1117}$ respectively. The direct particle interactions of the samples are completely screened. The red lines show fits to the data yielding the free diffusion coefficient D_0.

5.2.2. Dynamics of interacting colloidal suspensions

If colloidal particles in a suspension are interacting with each other, the diffusion of the particles is influenced by the interactions and thus $D(Q) \neq D_0$. In fig. 5.18 the relaxation rates $\Gamma(Q)$ of two samples with interparticle interactions are shown. While for one sample no electrolyte was added (0 µM), for the other sample the direct interparticle interactions were screened by the addition of 10 µM electrolyte. The resulting different strengths of interparticle interactions are reflected by the values of the static structure peaks of $S(Q_{max}) = 2.09$ and $S(Q_{max}) = 1.26$, respectively. The static structure peak can be found for both samples at the position $Q_{max} = 1.12 \times 10^{-3}$ Å^{-1}. The dashed line illustrates the calculated relaxation rates $\Gamma(Q)$ for a sample without particle interactions and thus free diffusing particles.

In both cases deviations from the dynamics of a dilute system can be seen. The relaxation rates are oscillating around the ones of a dilute system. At the position of the first maximum of the static structure factor $S(Q)$ the dynamics are slowed down, compared to the free particle dynamics, a phenomenon known as the de Gennes narrowing (De Gennes, 1959), $D(Q) = D_0/S(Q)$ predicting a momentum transfer Q

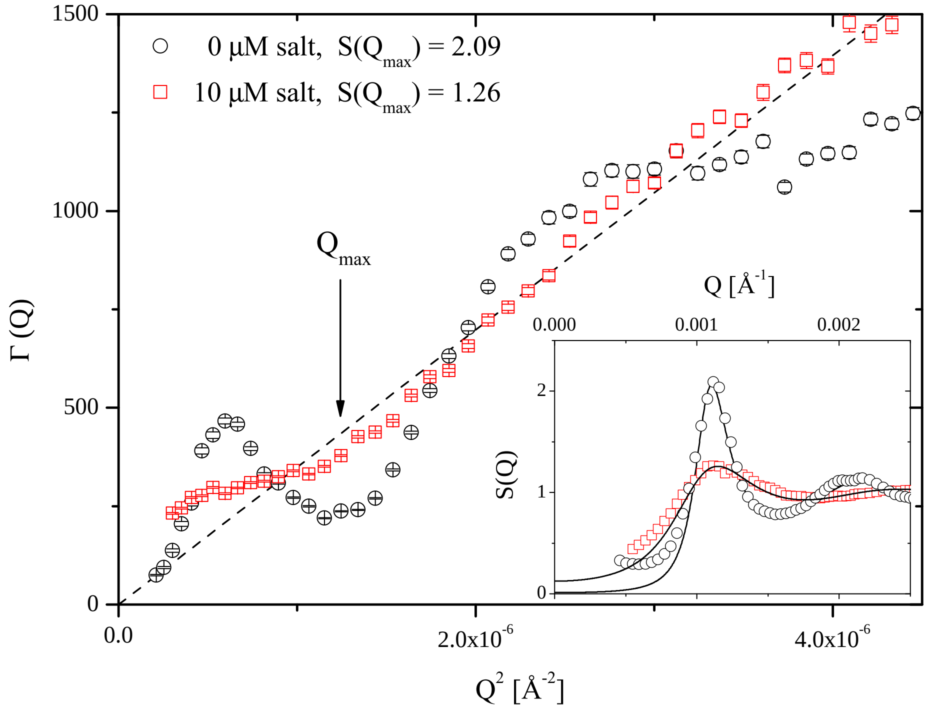

Figure 5.18.: Relaxation rates $\Gamma(Q)$ of two samples of volume fraction $\phi \approx 0.002$ as a function of the square of the momentum transfer Q^2. Both samples exhibit interparticle interactions. The dashed line shows the calculated relaxation rates $\Gamma(Q)$ of a sample without particle interactions. The arrow indicates the position of the first maximum of the static structure factors $S(Q_{max})$ at $Q^2 = 1.25 \cdot 10^{-6}$ Å^{-2}, which is at the same position for both samples. The inset shows the corresponding static structure factors were the solid lines display a fit of the RMSA model.

dependence in interacting systems when $S(Q) \neq 1$. This description is not taking into account hydrodynamic interactions. The slowing down effect is more pronounced for the sample exhibiting strong interparticle interactions, manifested in a larger peak value of the static structure factor.

In order to quantify the deviations from the dilute case, the normalized inverse diffusion coefficient or dynamic structure factor $D_0/D(Q)$ is calculated. Fig. 5.19 to fig. 5.21 show the normalized inverse effective diffusion coefficients for the samples of system PMMA$_{542}$ at five different nominal volume fractions ϕ_{nom} of 0.001, 0.002, 0.004, 0.008 and 0.012. For comparison the measured static structure factors are also displayed by solid lines.

The normalized effective diffusion coefficients follow the shape of the static structure factors for all samples. They show a maximum at approximately the same position as the peak of the static structure factor, indicating a slowing down of the system at these length scales. The peak is shifting to higher wave vectors Q with

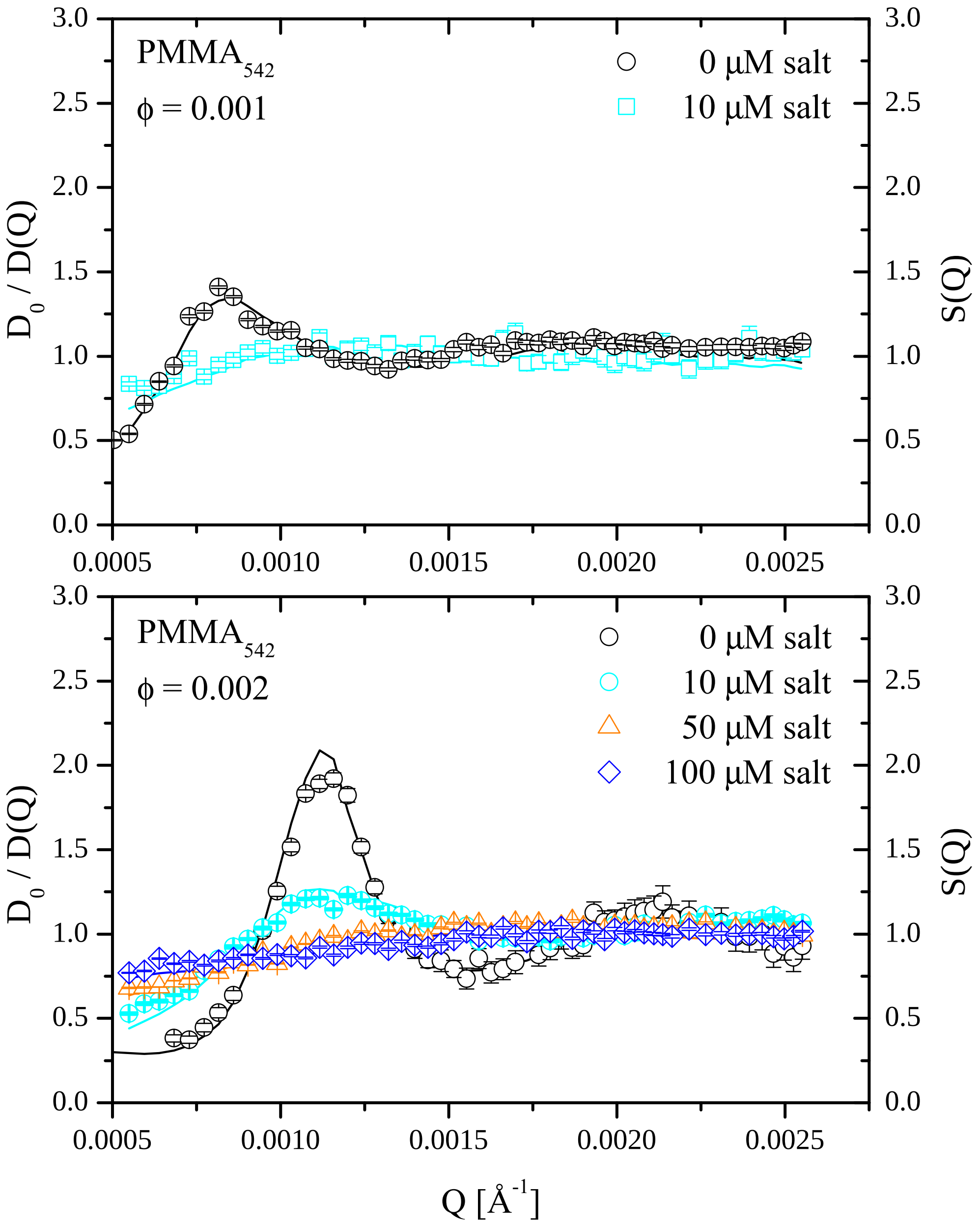

Figure 5.19.: Static structure factor $S(Q)$ (solid lines) and normalized inverse diffusion coefficient $D_0/D(Q)$ (symbols) of system PMMA$_{542}$ for two different nominal volume fractions ϕ_{nom} of 0.001 (top) and 0.002 (bottom). Lines and symbols of the same color belong to the same sample system.

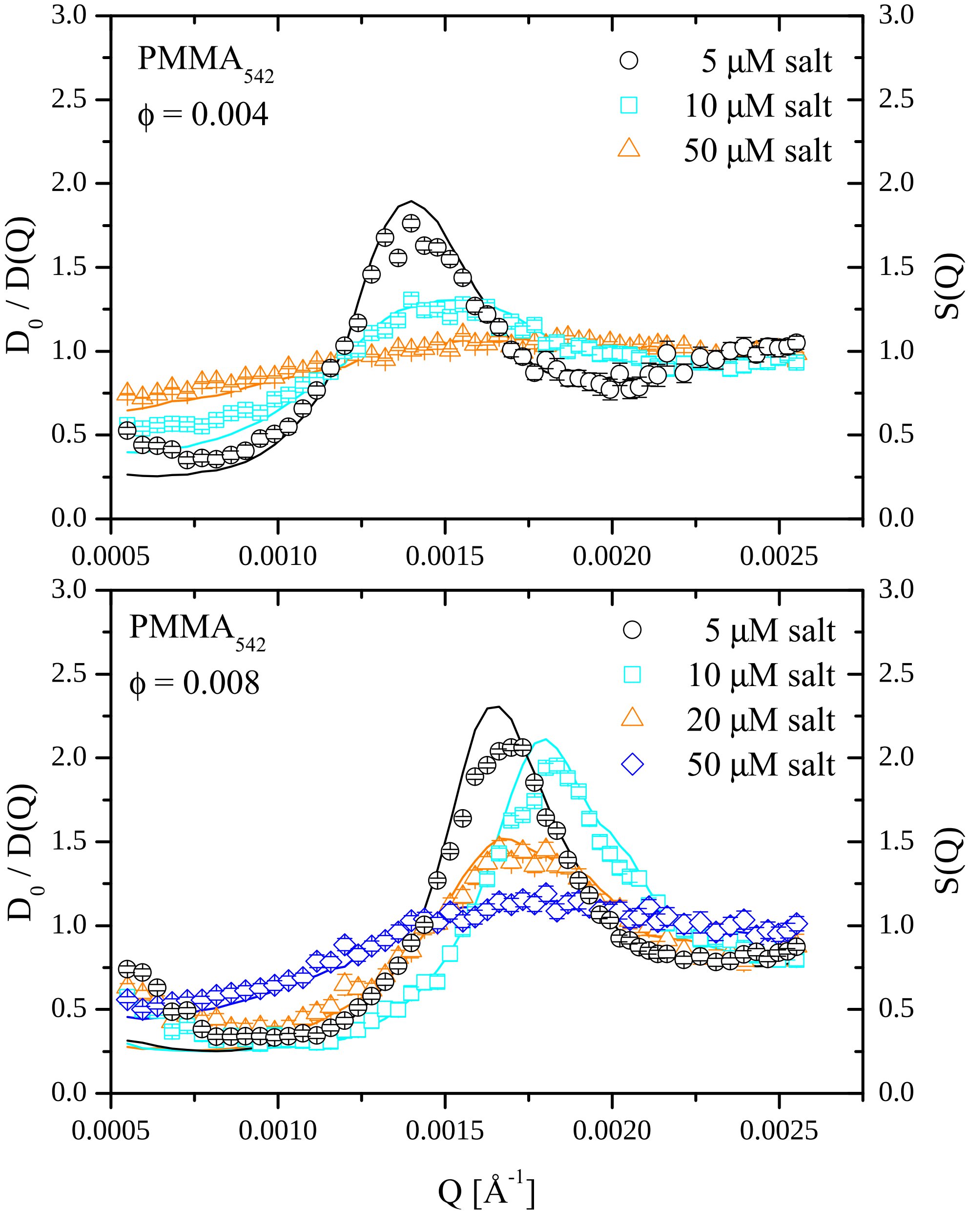

Figure 5.20.: Static structure factor $S(Q)$ (solid lines) and normalized inverse diffusion coefficient $D_0/D(Q)$ (symbols) of system PMMA$_{542}$ for two different volume fractions ϕ_{nom} of 0.004 (top) and 0.008 (bottom). Lines and symbols of the same color belong to the same sample system.

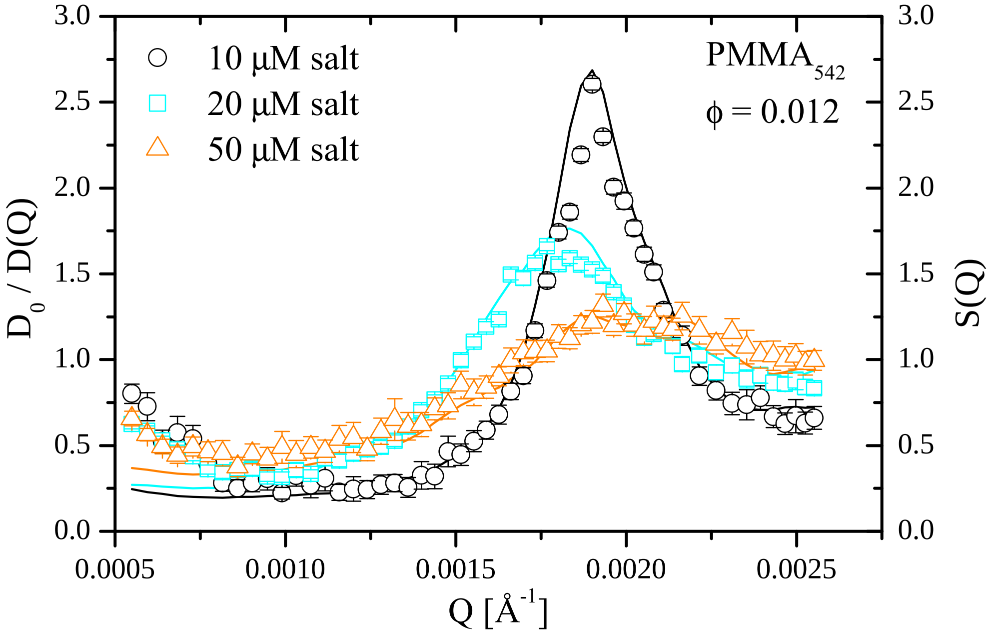

Figure 5.21.: Static structure factor $S(Q)$ (solid lines) and normalized effective diffusion coefficient $D_0/D(Q)$ (symbols) of system PMMA$_{542}$ for a volume fraction ϕ_{nom} of 0.012. Lines and symbols of the same color belong to the same sample system.

increasing volume fraction. The peaking behavior is more pronounced in samples of higher volume fraction, and is decreasing with increasing electrolyte concentration at a given volume fraction. In general, the values of the normalized effective diffusion coefficients are close to the values of the static structure factors. For samples showing static structure factor peak values $S(Q_{max}) < 1.5$ the values of the normalized inverse diffusion coefficient $D_0/D(Q)$ around the peak position are close to the values of the static structure factor. For samples exhibiting stronger direct particle interactions and thus a peak value $S(Q_{max}) > 1.5$, the values of the normalized inverse diffusion coefficients are slightly smaller than the values of the static structure factor. At higher volume fractions ϕ_{nom} from 0.004 to 0.012, a deviation towards higher values for the normalized effective diffusion coefficient can be seen for small momentum transfers.

The normalized inverse diffusion coefficients $D_0/D(Q)$ of system PMMA$_{1117}$ at nominal volume fractions $\phi_{\mathrm{nom}} = 0.08$, 0.16 and 0.33 are shown in fig. 5.22 and fig. 5.23. The solid lines display the corresponding static structure factors. The dynamic structure factor peaks around the maximum of the static structure factor similar to system PMMA$_{542}$. Contrary to system PMMA$_{542}$, we note that for the high volume fractions studied here, the normalized inverse diffusion coefficients show values higher as compared to the static structure factors $S(Q)$. With decreasing

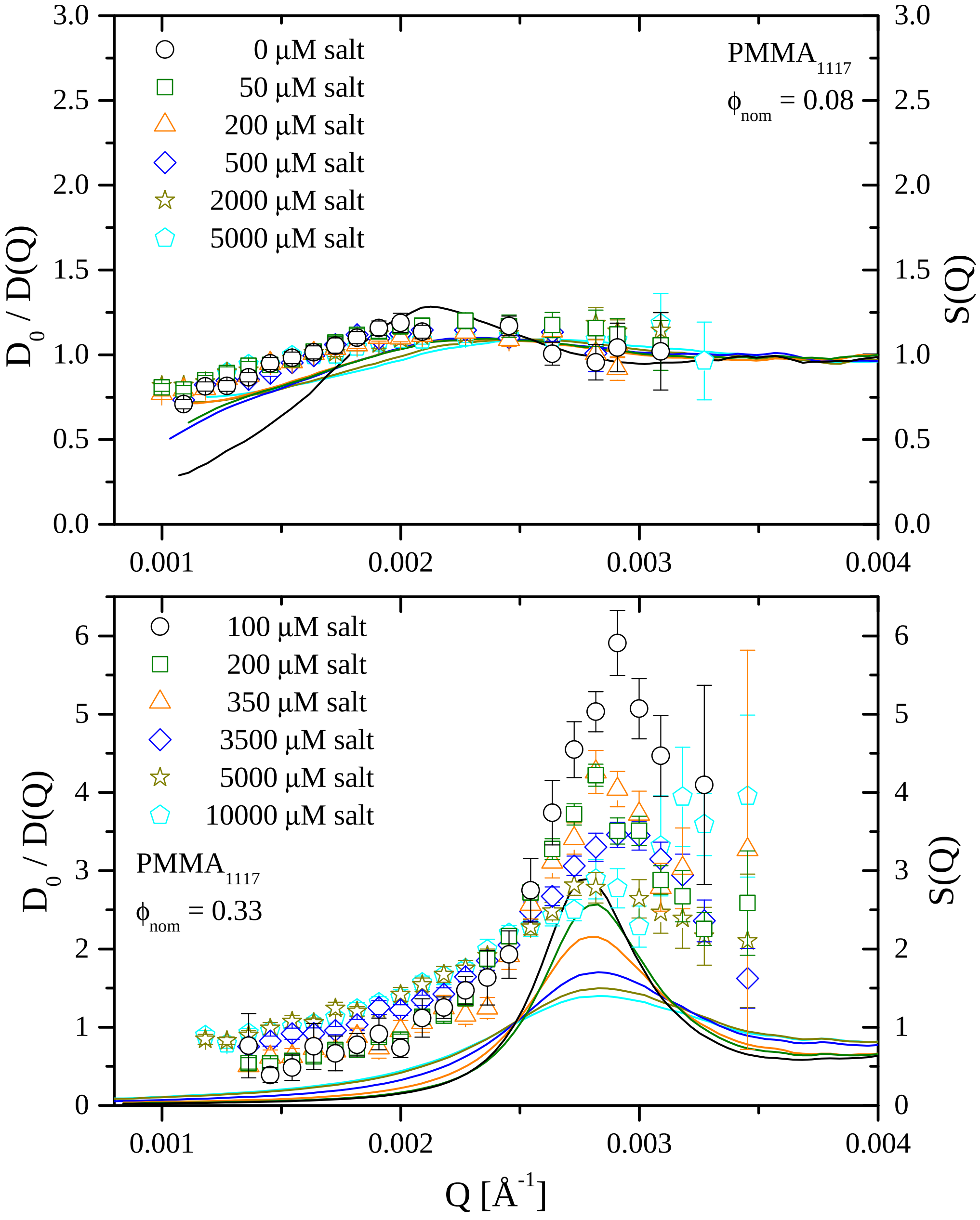

Figure 5.22.: Static structure factor $S(Q)$ (solid lines) and normalized inverse diffusion coefficient $D_0/D(Q)$ (symbols) of system PMMA$_{1117}$ for two different nominal volume fractions ϕ_{nom} of 0.08 (top) and 0.33 (bottom). Please note the different vertical scale for the bottom graph. Lines and symbols of the same color belong to the same sample system.

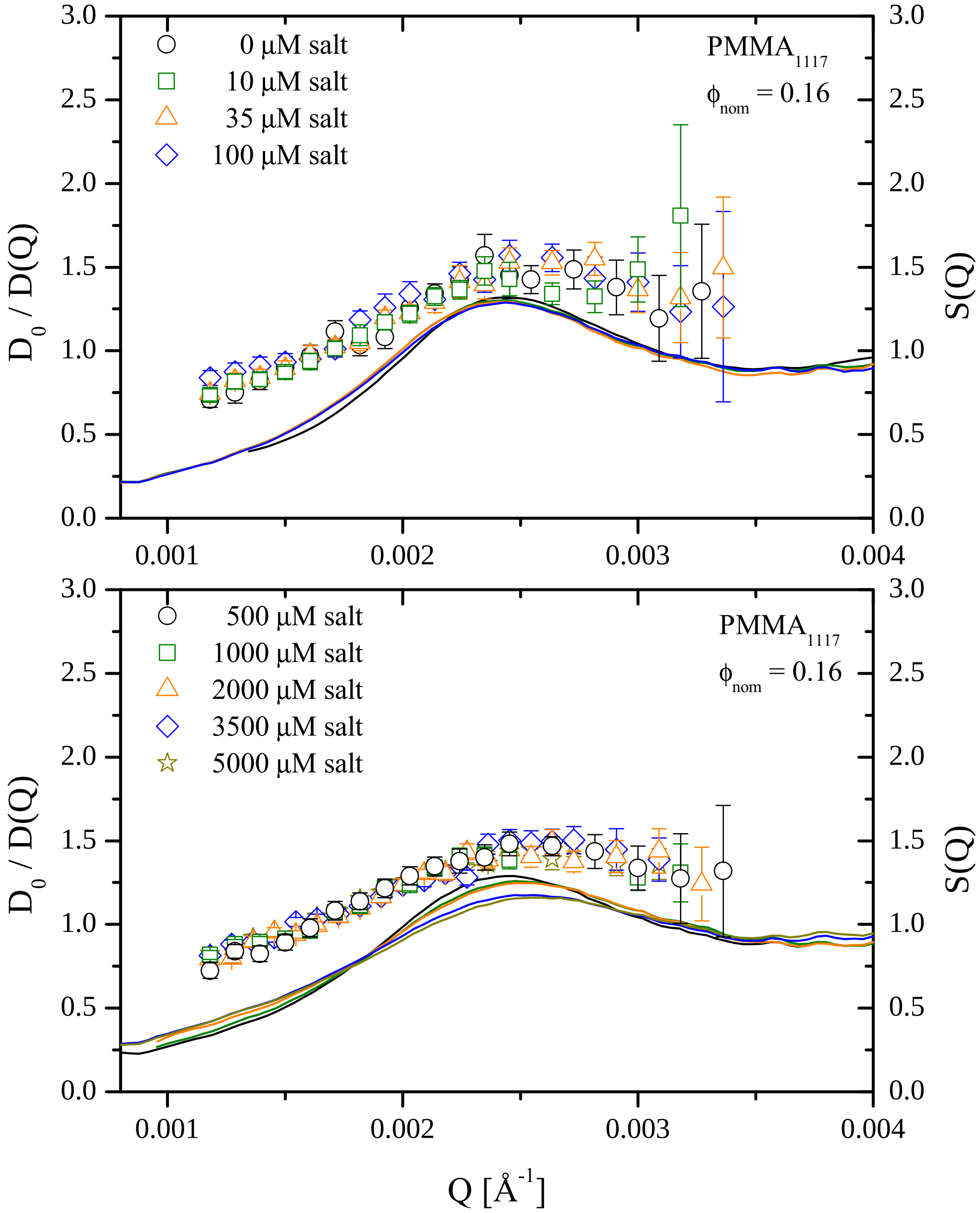

Figure 5.23.: Static structure factor $S(Q)$ (solid lines) and normalized inverse diffusion coefficient $D_0/D(Q)$ (symbols) of system PMMA$_{1117}$ for a nominal volume fraction ϕ_{nom} of 0.16. Lines and symbols of the same color belong to the same sample system.

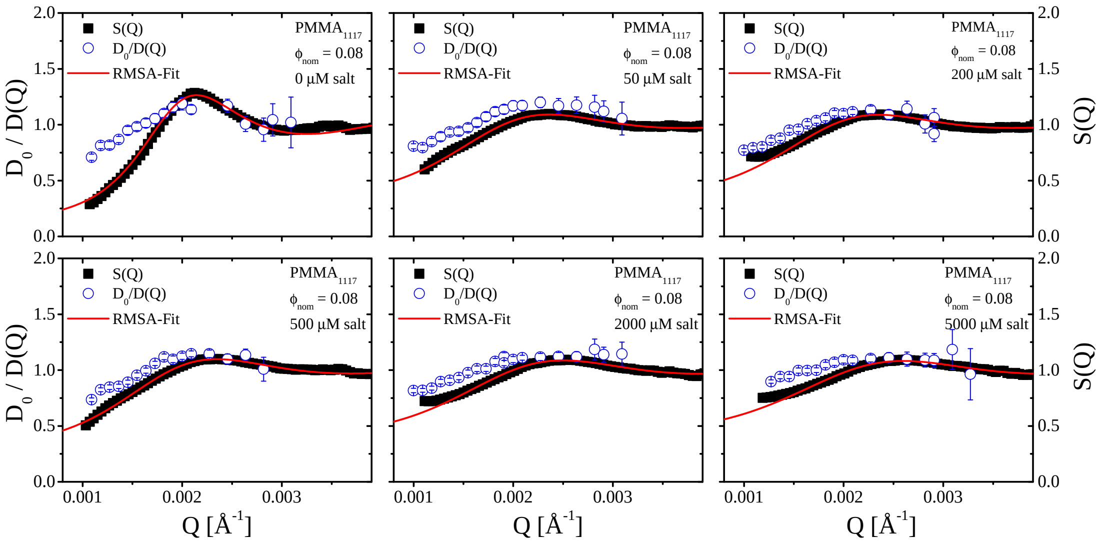

Figure 5.24.: Static structure factor $S(Q)$ and normalized inverse diffusion coefficient $D_0/D(Q)$ of system PMMA$_{1117}$ for a nominal volume fraction ϕ_{nom} of 0.08. The electrolyte concentrations of the samples are 0 µM, 50 µM, 200 µM, 500 µM, 2000 µM and 5000 µM. The red lines are fits of the RMSA model to the static structure factor.

strength of the interparticle interactions and subsequently lower values for the maximum of the static structure factor $S(Q_{max})$, the height of the normalized inverse diffusion coefficients $D_0/D(Q)$ is also decreasing.

In fig. 5.24 to fig. 5.26 the results for system PMMA$_{1117}$ are shown individually. For $\phi_{\text{nom}} = 0.08$ the normalized inverse diffusion coefficients have approximately the same values as the static structure factors of the corresponding sample. The dynamic structure factors of the more concentrated sample ($\phi_{\text{nom}} = 0.16$) display higher values than the corresponding static structure factors. In addition the peak height of $D_0/D(Q)$ decreases for the samples with increasing salt concentration. The same trend is clearly visible for the samples of the highest concentration of colloidal particles $\phi_{\text{nom}} = 0.33$: The samples show a strong decrease of the dynamic structure factor with increasing electrolyte concentration. Furthermore, it can be seen that the normalized inverse diffusion coefficients at this nominal volume fraction show the highest values of all samples investigated, indicating a strong slowing down of the system at this high concentration.

5.2.3. Discussion of the dynamic behavior

Free diffusion of colloidal particles was studied by dynamic light scattering showing Stokes-Einstein diffusion for the two systems. The hydrodynamic radius was slightly bigger than the geometrical radius as extracted by a fit of a polydisperse spherical form factor to the static data. This is usually interpreted by the presence

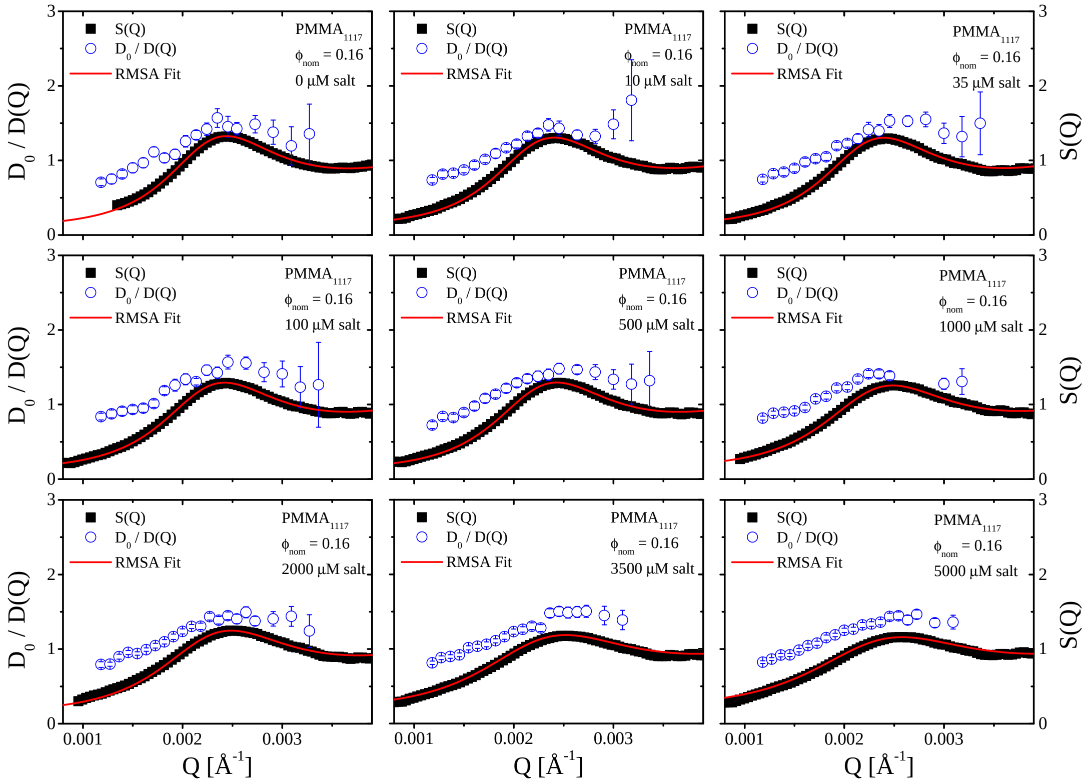

Figure 5.25.: Static structure factor $S(Q)$ and normalized inverse diffusion coefficient $D_0/D(Q)$ of system PMMA$_{1117}$ for a nominal volume fraction ϕ_{nom} of 0.16. The electrolyte concentrations of the samples are 0 µM, 10 µM, 35 µM, 100 µM, 500 µM, 1000 µM, 2000 µM, 3500 µM and 5000 µM. The red lines are fits of the RMSA model to the static structure factor.

of temporarily attached solvent molecules to the surface of the colloidal particles. This enlargement effect of the hydrodynamic radius is more pronounced for system PMMA$_{542}$, which might be explained by a higher charge per particle. The higher particle charge of system PMMA$_{542}$ is consistent with the observation that the onset of crystallization in a deionised suspension of particles occurs at lower concentrations as compared to system PMMA$_{1117}$. It is furthermore reflected by the fact that RMSA modeling assuming a constant effective charge yields $Z_{\text{eff}}(\text{PMMA}_{542}) = 496\,\text{e}^-$ and $Z_{\text{eff}}(\text{PMMA}_{1117}) = 221\,\text{e}^-$ respectively.

The dynamics characterization of the samples with direct interparticle interactions allowed the determination of the Q dependent effective diffusion coefficient $D(Q)$. The limiting values of the effective diffusion coefficient give access to the collective diffusion coefficient D_C in the $\lim_{Q\to 0}$ and to the short-time self diffusion coefficient $D^{\text{s,short}}$ in the $\lim_{Q\to\infty}$. For large wavevector transfers Q, the dynamics are probed on length scales smaller than the particle size, yielding the short-time diffusion coefficient $D^{\text{s,short}}$. For the dynamic light scattering experiments performed on

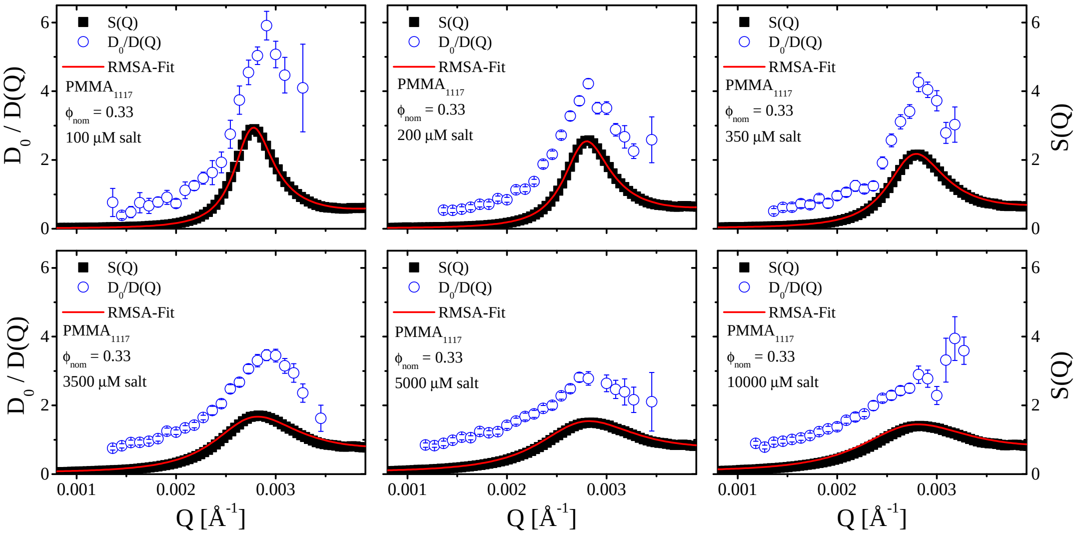

Figure 5.26.: Static structure factor $S(Q)$ and normalized inverse diffusion coefficient $D_0/D(Q)$ of system PMMA$_{1117}$ for a nominal volume fraction ϕ_{nom} of 0.33. The electrolyte concentrations of the samples are 100 µM, 200 µM, 350 µM, 3500 µM, 5000 µM and 10 000 µM. The red lines are fits of the RMSA model to the static structure factor.

system PMMA$_{542}$, the biggest attainable momentum transfer $Q \approx 0.00255\,\text{Å}^{-1}$ was far below the Q-values corresponding to the diameter of a single spherical particle $Q \approx 0.0058\,\text{Å}^{-1}$. The effective diffusion coefficient at the largest Q-values is therefore still influenced by the motions and interactions of an ensemble of colloidal particles, displayed in modulations of the dynamic structure factor (e.g. fig. 5.19, sample $\phi_{\text{nom}} = 0.002$ and 0 µM electrolyte). For system PMMA$_{1117}$ measured with X-rays, the largest momentum transfers investigated ($Q \approx 0.0035\,\text{Å}^{-1}$) are only slightly bigger than the Q-values corresponding to the diameter of a single colloidal particle $Q \approx 0.0028\,\text{Å}^{-1}$. As the mean particle spacing of system PMMA$_{1117}$ is small, the short-time self diffusion coefficient extracted at the highest probed momentum transfers can only provide a qualitative description of the self diffusion. The normalized short-time self diffusion coefficients $D(Q \to \infty)/D_0$, which have been extracted from the highest Q-values investigated for the corresponding sample, are displayed in fig. 5.27.

For system PMMA$_{542}$, $D(Q \to \infty)/D_0$, is close to unity for the samples with the highest electrolyte concentrations and slightly above the hard sphere values. At lower salt concentrations, the values of $D^{\text{s,short}}/D_0$ are randomly oscillating around unity. This is due to the strong influence of the shape of the dynamic structure factor at the largest investigated Q-values (see for example fig. 5.21 on page 71: The samples at salt concentrations of 10 µM and 20 µM). The short-time self diffusion coefficients of system PMMA$_{1117}$ decrease with increasing volume fraction ϕ without displaying a clear dependence on the electrolyte concentration, showing the same

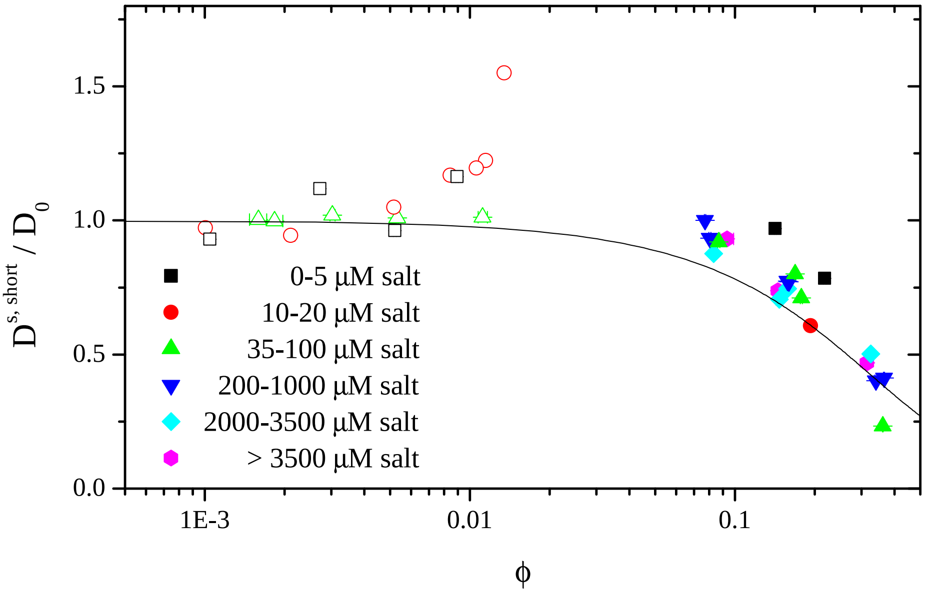

Figure 5.27.: Normalized short-time self diffusion coefficient $D(Q \to \infty)/D_0$ as a function of the volume fraction ϕ. The solid line displays the short-time self diffusion coefficient of a hard sphere system calculated within the $\delta\gamma$-approximation. Filled symbols refer to system PMMA_{1117}, open symbols refer to system PMMA_{542}.

qualitative behavior as predicted for deionised charge stabilized systems (Banchio *et al.*, 2008). This is in agreement with experimental results (Horn *et al.*, 2000). While the $D^{s,short}/D_0$ values are close to unity or smaller, they are, except for one sample, higher than the corresponding hard sphere value. These low values of $D^{s,short}$ compared to D_0 can be attributed to the presence of indirect hydrodynamic interactions mediated by the dispersion medium.

At small wavevector transfers ($Q \to 0$), corresponding to length scales of several diameters of the particles, the collective motions of the colloids are probed. The normalized effective diffusion coefficients $D(Q \to 0)/D_0$ are shown in fig. 5.28.

The collective short-time diffusion coefficient D_C is always above unity indicative of faster dynamics compared to free diffusion. For both systems $D(Q \to 0)$ increases with increasing volume fraction (and thus increasing direct particle interactions) and decreases with increasing concentration of additional salt ions at a given volume fraction (and thus decreasing direct particle interactions). The collective diffusion coefficient describes the initial decay of long-wavelength density fluctuations. For systems of strong repulsive interactions D_C/D_0 is found to be substantially larger than unity (Nägele, 1996), and has also been found to increase with increasing volume fraction and increasing strength of the interaction potential (Tirado-Miranda *et al.*, 2003) in agreement with our findings. Moreover, the observed effect of an enhancement of the collective diffusion in moderately concentrated suspensions ($\phi =$

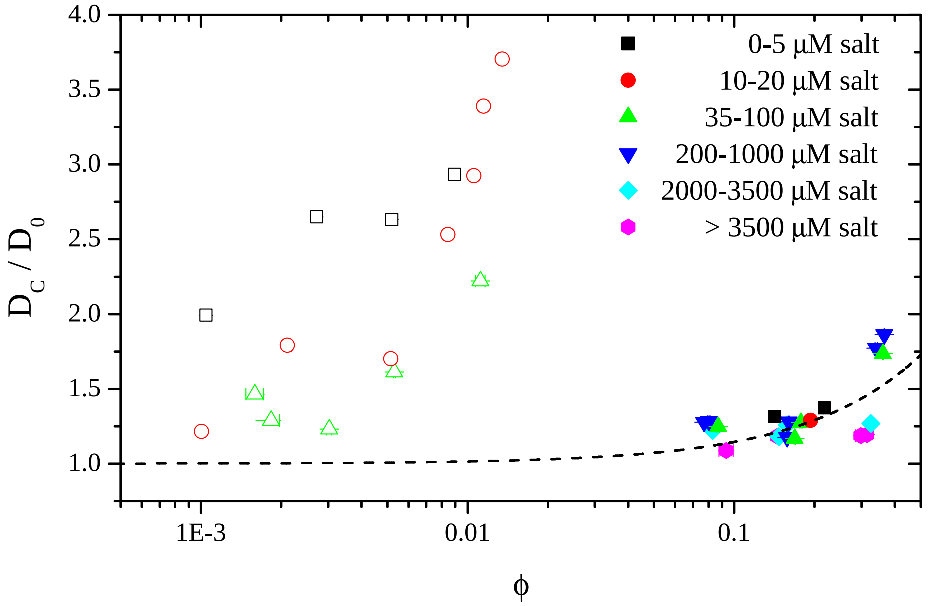

Figure 5.28.: Normalized collective short-time self diffusion coefficient $D(Q \to 0)/D_0$ as a function of the volume fraction ϕ. The solid line displays the short-time collective diffusion coefficient of a hard sphere system. Filled symbols refer to system PMMA_{1117}, open symbols refer to system PMMA_{542}.

0.01 – 0.04) of charged spheres with weakly screened particle interactions has been calculated theoretically (Daguanno *et al.*, 1990) and found experimentally (Chatenay *et al.*, 1987). For hard-sphere systems, the normalized short-time collective diffusion coefficient can be approximated by $D_C/D_0 = 1 + 1.454\phi$ (Cichocki and Felderhof, 1988), as displayed by the dashed line in fig. 5.28. While the values of system PMMA_{542} are substantially higher than the calculated hard sphere behavior, the normalized collective diffusion coefficients of system PMMA_{1117} follows qualitatively the hard sphere behavior.

The $D_0/D(Q)$ values are relatively close to the static structure factor $S(Q)$ for volume fractions $\phi < 0.02$ and peak values of the static structure factor $S(Q_{max}) < 1.5$. $D_0/D(Q)$ displays stronger deviations from the static structure factor at higher volume fractions or stronger interparticle interactions with a higher peak value $S(Q_{max})$. Since the dynamics and the static structure factor are similar without considering hydrodynamic interactions (see eq. (3.41)), this observation points to the presence of hydrodynamic interactions in the probed samples. We note further that for dilute to moderate concentrated systems $\phi < 0.2$ the peak values of $D_0/D(Q)$ are smaller than the corresponding maximum of the static structure factor $S(Q_{max})$, indicating an increase of the particles' mobility due to hydrodynamic interactions. At higher volume fractions, the peak values of $D_0/D(Q)$ are smaller than $S(Q_{max})$, denoting a slowing down of the dynamics as a result of the hydrodynamic

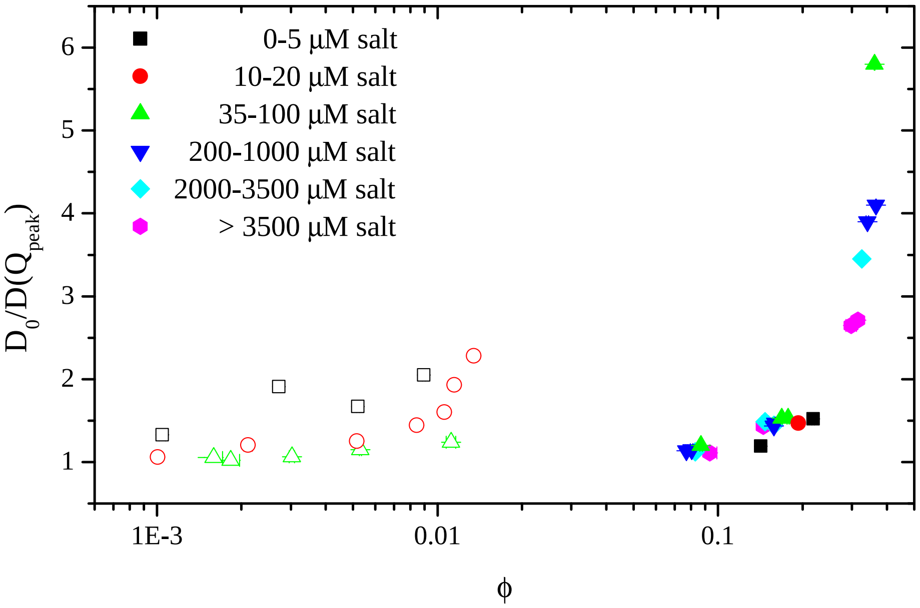

Figure 5.29.: Peak values of the normalized inverse effective diffusion coefficient $D_0/D(Q_{peak})$ as a function of the volume fraction ϕ. Filled symbols refer to system PMMA$_{1117}$, open symbols refer to system PMMA$_{542}$.

interactions. Fig. 5.29 displays the evolution of the peak values $D_0/D(Q_{peak})$ as a function of the volume fraction.

Both systems show an increase of the dynamic structure factor maximum with increasing volume fraction. While the increase is moderate for system PMMA$_{542}$, the steepness of the increase is higher for system PMMA$_{1117}$. Subsequently, the highest peak values are measured at the highest investigated volume fraction $\phi_{\text{nom}} = 0.33$. Moreover, the peak values are decreasing with increasing salt concentration. Fig. 5.30 shows the evolution of the peak values as a function of the concentration of added ions.

The peak values $D_0/D(Q_{peak})$ decrease with increasing salt concentration for the eight volume fractions investigated. This effect is more pronounced for samples with stronger particle interactions (higher value of $S(Q_{max})$, samples at a nominal volume fraction of 0.004, 0.008, 0.012 and 0.33). The same trend, an increase of the peak values $D_0/D(Q_{peak})$ with increasing volume fraction and decreasing salt concentration have been found by *Gapinski et al.* (Gapinski *et al.*, 2007, 2009). We note that the absolute peak values found by these authors are $D_0/D(Q_{peak}) < 3$. Peak values of the same magnitude have been found by *Robert et al.* (Robert *et al.*, 2008) for the highest volume fraction investigated, as it is the case in our experiments.

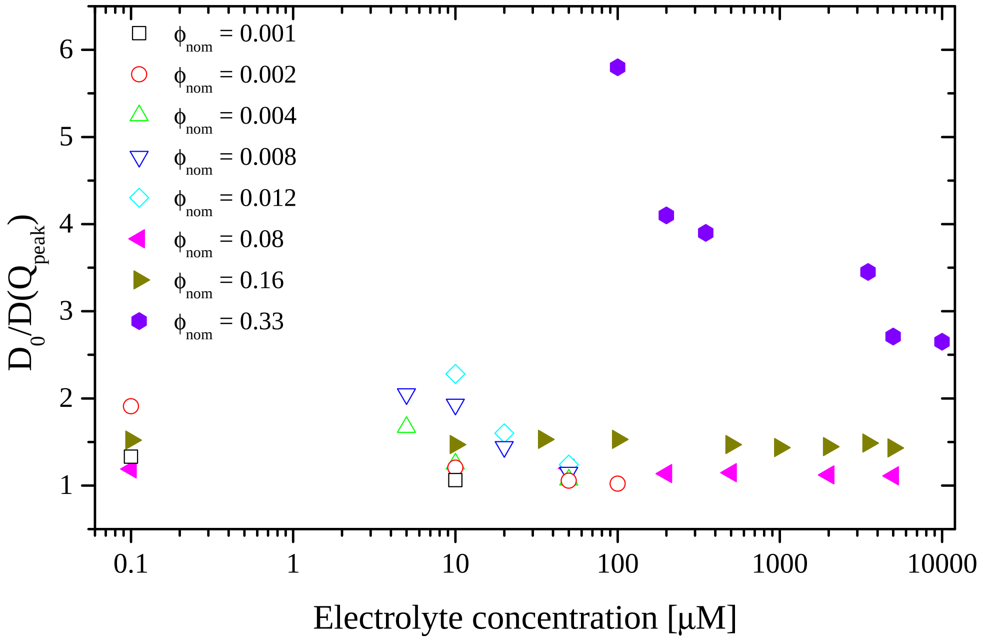

Figure 5.30.: Peak values of the normalized inverse effective diffusion coefficient $D_0/D(Q_{peak})$ as a function of the electrolyte concentration. Filled symbols refer to system PMMA_{1117}, open symbols refer to system PMMA_{542}.

5.3. Hydrodynamic interactions of colloidal suspensions

The differences between the measured static structure factor and the dynamic structure factor already point towards the presence of hydrodynamic interactions. This indirect, hydrodynamic interactions between the colloidal particles in a suspension are interactions which are mediated by the dispersion medium. The hydrodynamic behavior of a colloidal suspension can be quantified in the short-time limit by calculating the hydrodynamic function, using as input the measured static and dynamic properties of a sample

$$H(Q) = \frac{D(Q)}{D_0} \cdot S(Q). \tag{5.6}$$

It is thus possible to extract the hydrodynamic functions from the measured static and dynamic behavior of a sample without referring to a theoretical model, as shown exemplary in fig. 5.31.

The hydrodynamic function $H(Q)$ of a sample of system PMMA_{1117} at $\phi_{\mathrm{nom}} = 0.33$ and 200 µM of added salt is at all momentum transfers below unity, since the normalized inverse diffusion coefficient lies always above the static structure factor.

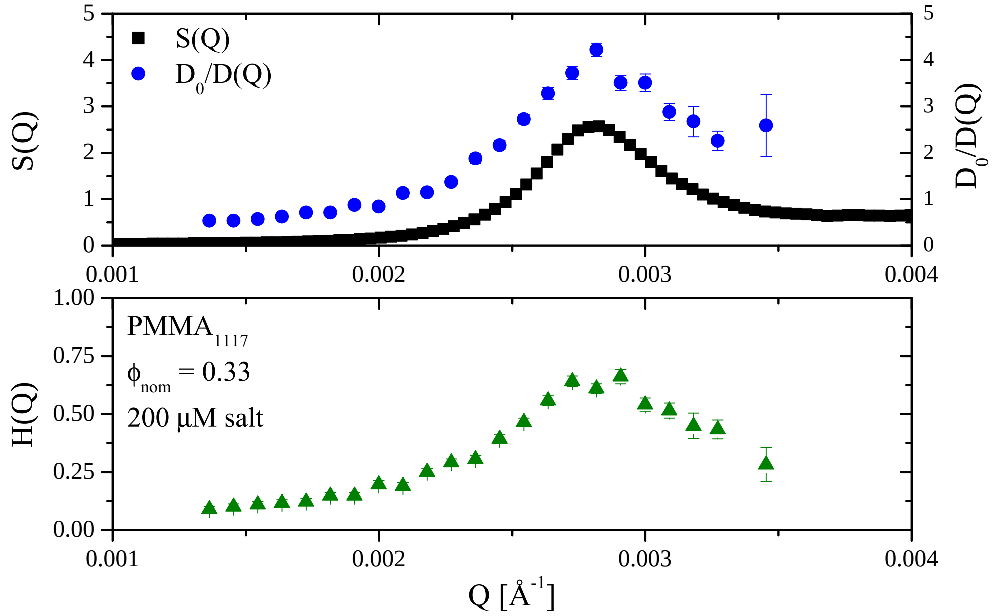

Figure 5.31.: Top: Static structure factor and normalized inverse diffusion coefficient of a PMMA$_{1117}$ ($\phi_{nom} = 0.33$, 200 µM salt) sample as a function of wavevector transfer Q. Bottom: Hydrodynamic function of the same sample as a function of wavevector transfer Q.

Similar to the static and dynamic behavior, the hydrodynamic function shows a pronounced peak at Q-values around the mean interparticle spacing.

Subsequently, the hydrodynamic functions of all samples were extracted. The hydrodynamic functions of system PMMA$_{542}$ are shown in fig. 5.32, fig. 5.33, fig. 5.34, fig. 5.35 and fig. 5.36 while the hydrodynamic functions of system PMMA$_{1117}$ are shown in fig. 5.37, fig. 5.38 and fig. 5.39.

Similar to the static structure factor $S(Q)$ and the normalized inverse diffusion coefficient $D_0/D(Q)$, all extracted hydrodynamic functions show a maximum. This behavior is always more pronounced for samples of low electrolyte concentration. Moreover, the peak position shifts to higher momentum transfers with increasing volume fraction and is thus located at momentum transfers around the peak position of the static structure factor $S(Q_{max})$, which corresponds to the mean interparticle spacing of particles in the sample.

The peak values of the hydrodynamic functions $H(Q_{max})$ are above unity for the samples of system PMMA$_{542}$, indicating for volume fractions ϕ smaller than 0.015 an increased particle mobility caused by hydrodynamic interactions. For samples of higher direct particle interactions, characterized by a more pronounced first maximum of the static structure factor, the peak of the hydrodynamic functions displays also a higher value, as summarized in table 5.5.

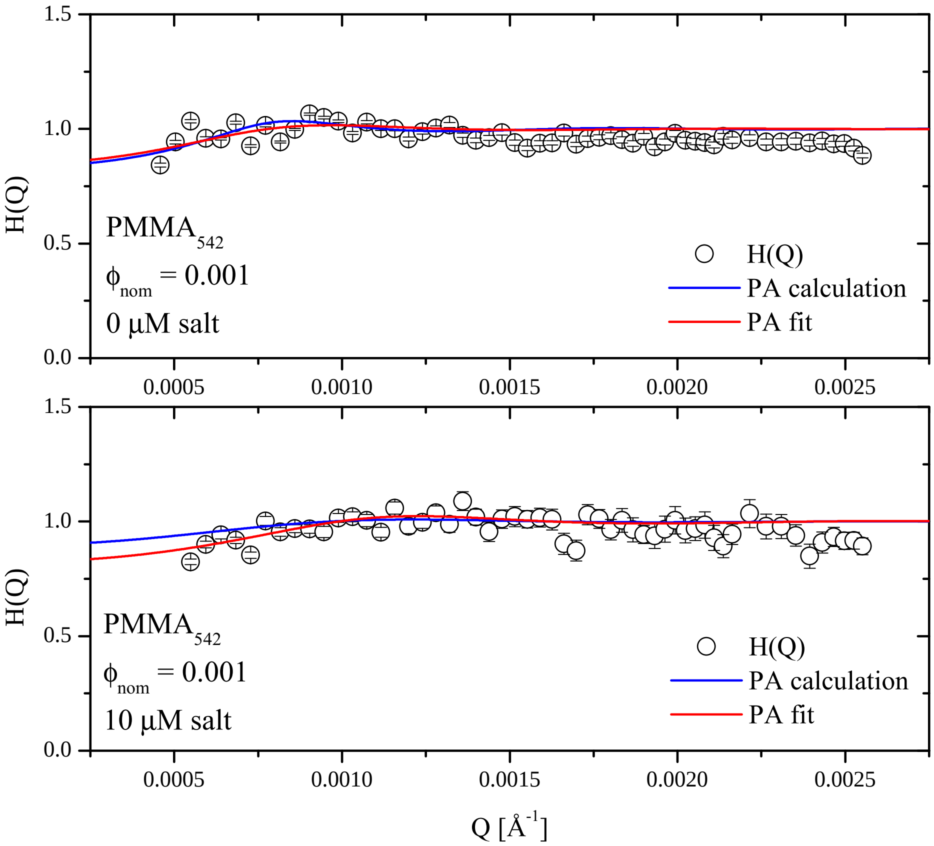

Figure 5.32.: Hydrodynamic functions $H(Q)$ as a function of momentum transfer Q of system PMMA$_{542}$ for a nominal volume fraction ϕ_{nom} of 0.001. The electrolyte concentrations of the samples are 0 µM and 10 µM. The blue lines show the predictions of the pairwise additive approximation using the measured static structure as input. The red lines are fits of the pairwise additive approximation with fit parameters ϕ and Z_{eff} to the data.

For high volume fractions ($\phi > 0.06$), investigated with samples of system PMMA$_{1117}$, the peak values of the hydrodynamic function are smaller than unity, indicating a slowing down of the system due to the hydrodynamic interactions. The only exception from this behavior is the deionised sample (salt concentration 0 µM) with a nominal volume fraction $\phi_{\text{nom}} = 0.08$. The peak values of the hydrodynamic functions decrease with increasing volume fractions, the lowest peak value can be observed at the highest nominal volume fraction of $\phi = 0.33$, as displayed in table 5.5.

For the further analysis of the hydrodynamic interactions, the hydrodynamic functions have been compared with theoretical models, the pairwise additive approximation (PA) and the $\delta\gamma$-expansion.

Table 5.5.: System, salt concentration, nominal volume fraction ϕ_{nom}, peak value of the static structure factor $S(Q_{max})$, ϕ extracted by the RMSA fit to the static structure factors $S(Q)$ and peak value of the hydrodynamic function $H(Q_{max})$.

System	ϕ_{nom}	Salt_{nom} [µM]	$S(Q_{\text{max}})$	RMSA-ϕ	$H(Q_{\text{max}})$
$PMMA_{542}$	0.001	0	1.35	0.0010	1.05
$PMMA_{542}$	0.001	10	1.06	0.0010	1.02
$PMMA_{542}$	0.002	0	2.09	0.0027	1.11
$PMMA_{542}$	0.002	10	1.26	0.0021	1.04
$PMMA_{542}$	0.002	50	1.05	0.0016	1.02
$PMMA_{542}$	0.002	100	1.03	0.0018	1.01
$PMMA_{542}$	0.004	5	1.89	0.0052	1.12
$PMMA_{542}$	0.004	10	1.31	0.0052	1.05
$PMMA_{542}$	0.004	50	1.08	0.0030	1.02
$PMMA_{542}$	0.008	5	2.31	0.0089	1.15
$PMMA_{542}$	0.008	10	2.11	0.0115	1.14
$PMMA_{542}$	0.008	20	1.52	0.0084	1.10
$PMMA_{542}$	0.008	50	1.16	0.0053	1.03
$PMMA_{542}$	0.012	10	2.69	0.0135	1.19
$PMMA_{542}$	0.012	20	1.76	0.0106	1.12
$PMMA_{542}$	0.012	50	1.26	0.0112	1.05
$PMMA_{1117}$	0.08	0	1.28	0.142	1.03
$PMMA_{1117}$	0.08	50	1.10	0.087	0.93
$PMMA_{1117}$	0.08	200	1.09	0.077	0.97
$PMMA_{1117}$	0.08	500	1.10	0.080	0.97
$PMMA_{1117}$	0.08	2000	1.09	0.086	0.97
$PMMA_{1117}$	0.08	5000	1.09	0.093	0.97
$PMMA_{1117}$	0.16	0	1.32	0.218	0.91
$PMMA_{1117}$	0.16	10	1.30	0.193	0.91
$PMMA_{1117}$	0.16	35	1.29	0.178	0.90
$PMMA_{1117}$	0.16	100	1.29	0.169	0.87
$PMMA_{1117}$	0.16	500	1.29	0.160	0.88
$PMMA_{1117}$	0.16	1000	1.26	0.158	0.88
$PMMA_{1117}$	0.16	2000	1.25	0.158	0.87
$PMMA_{1117}$	0.16	3500	1.17	0.147	0.83
$PMMA_{1117}$	0.16	5000	1.16	0.145	0.82
$PMMA_{1117}$	0.33	100	2.89	0.360	0.61
$PMMA_{1117}$	0.33	200	2.57	0.365	0.61
$PMMA_{1117}$	0.33	350	2.15	0.341	0.59
$PMMA_{1117}$	0.33	3500	1.70	0.325	0.54
$PMMA_{1117}$	0.33	5000	1.50	0.315	0.54
$PMMA_{1117}$	0.33	10000	1.40	0.298	0.53

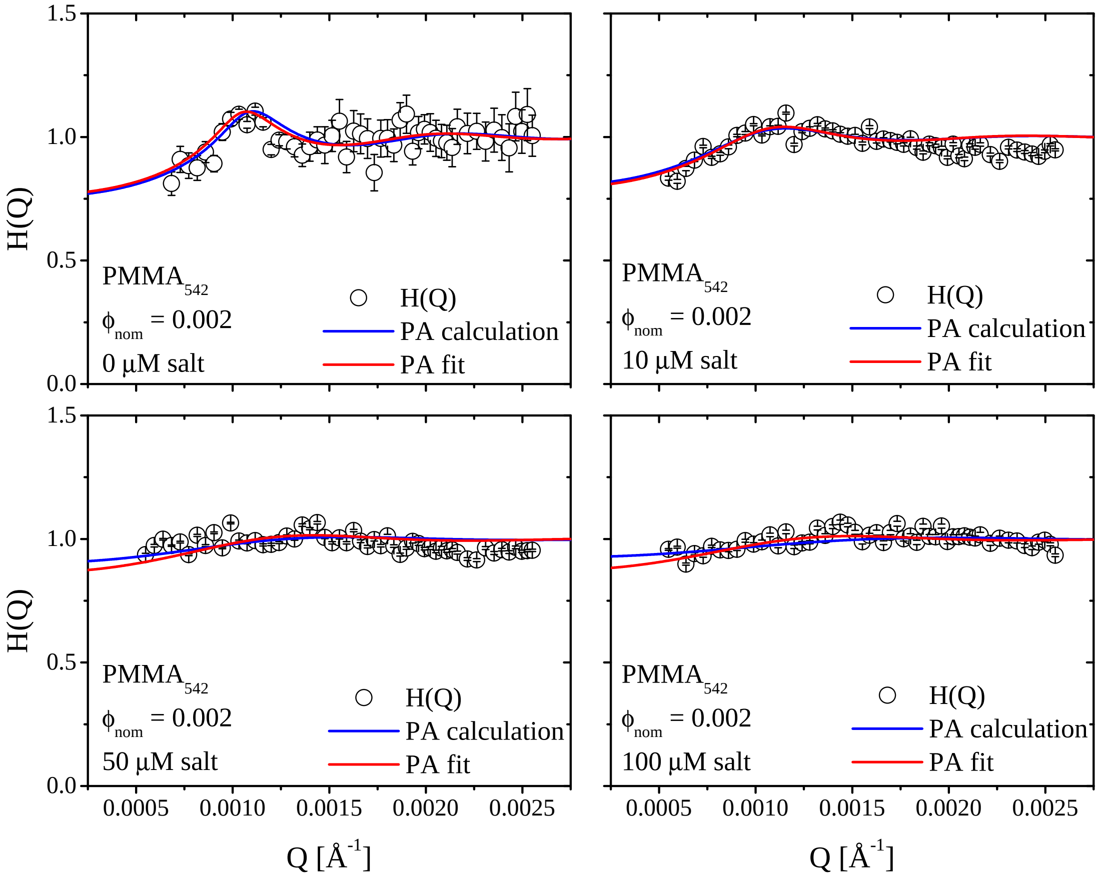

Figure 5.33.: Hydrodynamic functions $H(Q)$ as a function of momentum transfer Q of system PMMA$_{542}$ for a nominal volume fraction ϕ_{nom} of 0.002. The electrolyte concentrations of the samples are 0 µM, 10 µM, 50 µM and 100 µM. The blue lines show the predictions of the pairwise additive approximation using the measured static structure as input. The red lines are fits of the pairwise additive approximation with fit parameters ϕ and Z_{eff} to the data.

5.3.1. Pairwise additive approximation

A description of the hydrodynamic functions in dilute to moderately concentrated suspensions of electrostatically interacting colloidal particles is possible by the pairwise additive approximation (Nägele *et al.*, 1993; Nägele *et al.*, 1994; Nägele and Baur, 1997), which assumes pairwise additivity of the hydrodynamic interactions and expresses the mobility tensors in terms of an expansion in the inverse distance r^{-1} up to terms r^{-8}. The resulting hydrodynamic function is given by eq. (3.52) and eq. (3.53) and depends on the pair distribution function $g(r)$ and the volume fraction ϕ of the system.

The pair distribution function $g(r)$ of the analyzed systems was calculated from the measured static structure factors $S(Q)$, parametrized by the RMSA model. The

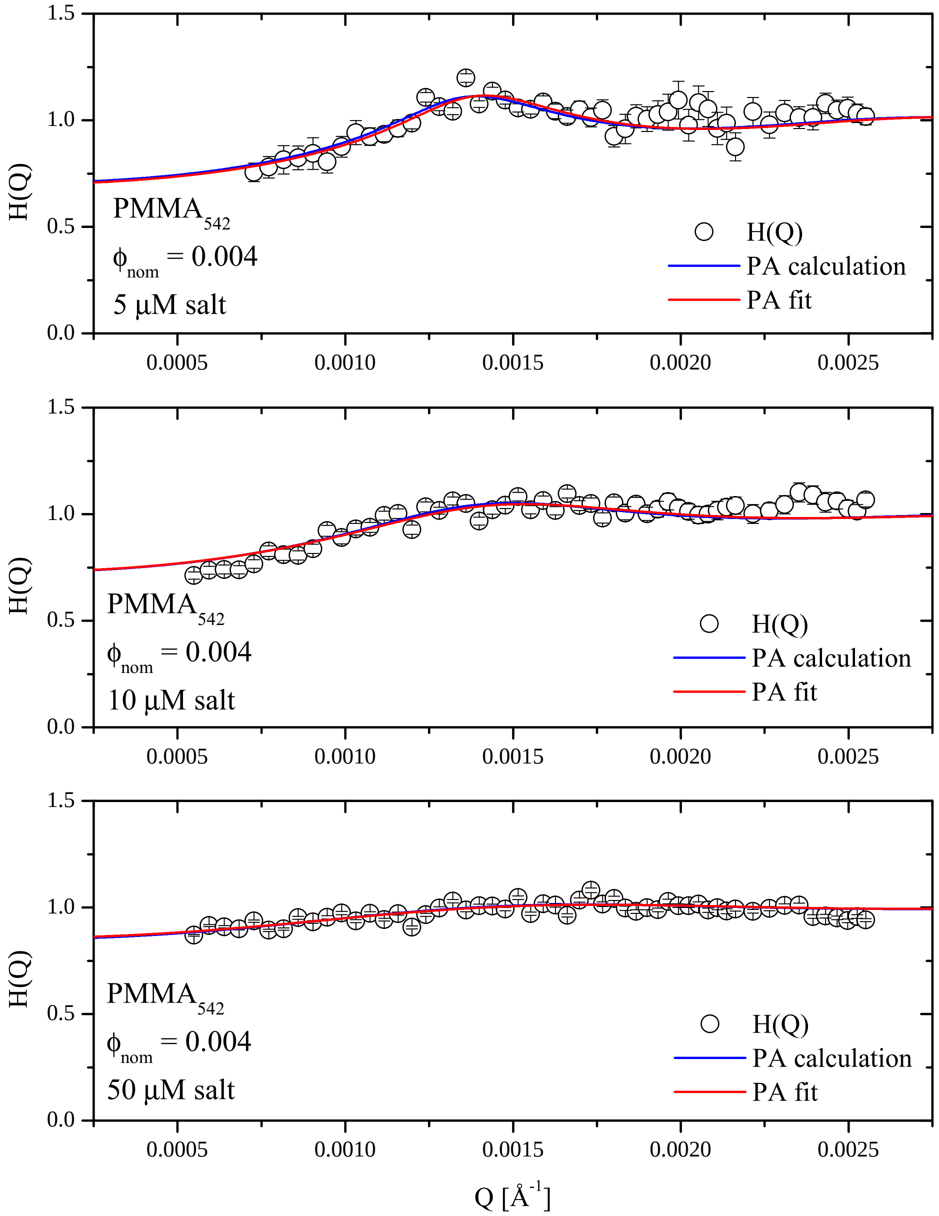

Figure 5.34.: Hydrodynamic functions $H(Q)$ as a function of momentum transfer Q of system PMMA$_{542}$ for a nominal volume fraction ϕ_{nom} of 0.004. The electrolyte concentrations of the samples are 5 µM, 10 µM and 50 µM. The blue lines show the predictions of the pairwise additive approximation using the measured static structure as input. The red lines are fits of the pairwise additive approximation with fit parameters ϕ and Z_{eff} to the data.

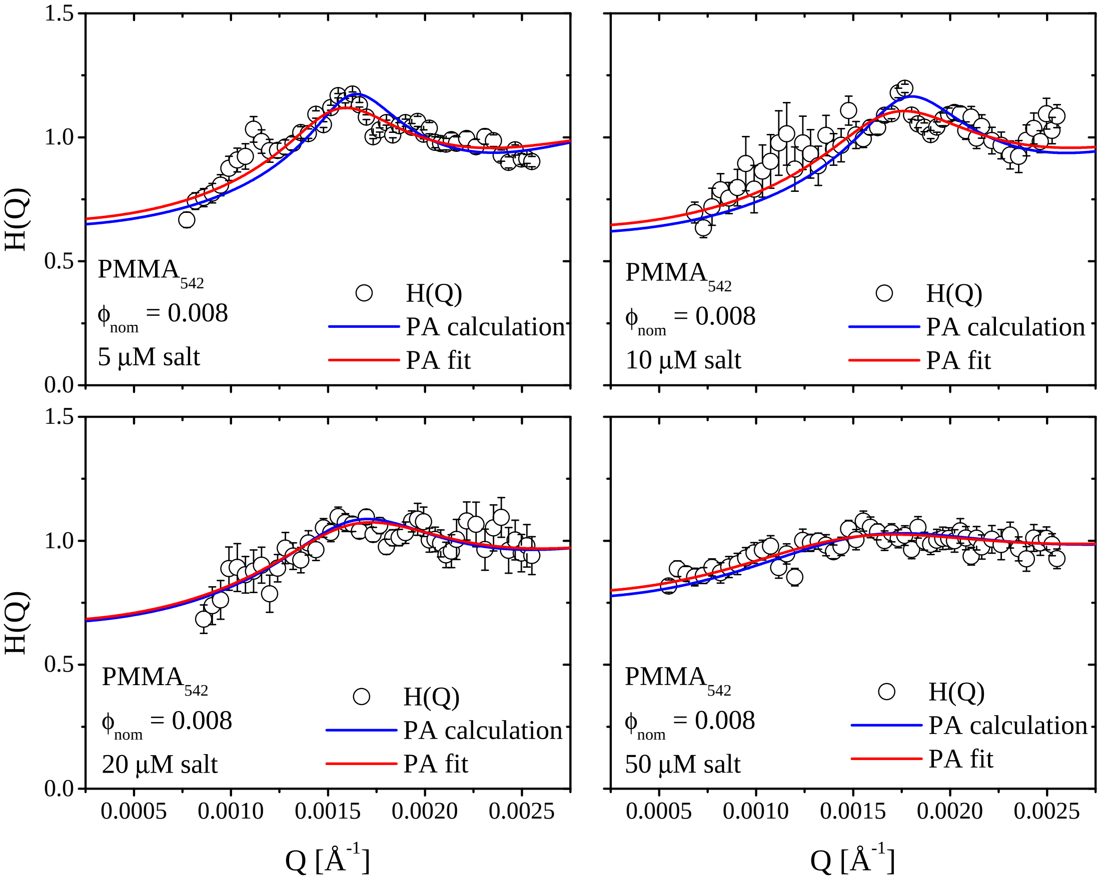

Figure 5.35.: Hydrodynamic functions $H(Q)$ as a function of momentum transfer Q of system PMMA$_{542}$ for a nominal volume fraction ϕ_{nom} of 0.008. The electrolyte concentrations of the samples are 5 µM, 10 µM, 20 µM and 50 µM. The blue lines show the predictions of the pairwise additive approximation using the measured static structure as input. The red lines are fits of the pairwise additive approximation with fit parameters ϕ and Z_{eff} to the data.

resulting hydrodynamic functions $H(Q)$ are shown as solid blue lines in fig. 5.32 to fig. 5.38. The red lines are fits of the PA approximation to the data as described later. As the assumption of pairwise additive hydrodynamic interactions restricts the analysis to systems of volume fractions $\phi < 0.1$, it is no surprise that the pairwise additive approximation fails to describe the extracted hydrodynamic functions at high volume fractions ($\phi_{\mathrm{nom}} = 0.16$, see fig. 5.38). For the highest nominal volume fraction investigated ($\phi_{\mathrm{nom}} = 0.33$), the pairwise additive approximation yields unphysical results with $H(Q) < 0$ and is thus not displayed.

The calculated pairwise additive approximation is in good agreement with the extracted hydrodynamic functions of system PMMA$_{542}$ (fig. 5.32 to fig. 5.36) at nominal volume fractions $0.001 \leq \phi_{\mathrm{nom}} \leq 0.012$. The position and height of the

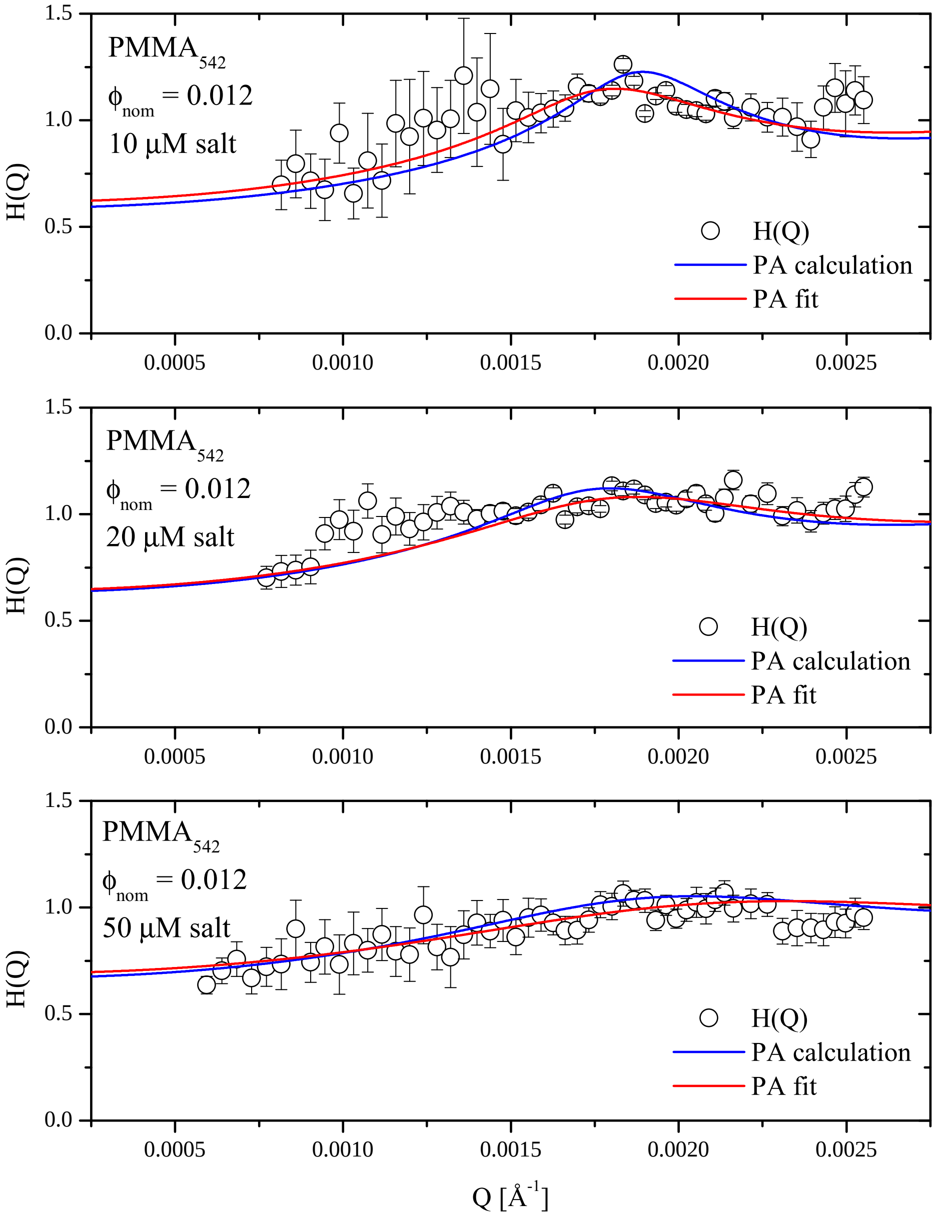

Figure 5.36.: Hydrodynamic functions $H(Q)$ as a function of momentum transfer Q of system PMMA$_{542}$ for a nominal volume fraction ϕ of 0.012. The electrolyte concentrations of the samples are 10 µM, 20 µM and 50 µM. The blue lines show the predictions of the pairwise additive approximation using the measured static structure as input. The red lines are fits of the pairwise additive approximation with fit parameters ϕ and Z_{eff} to the data.

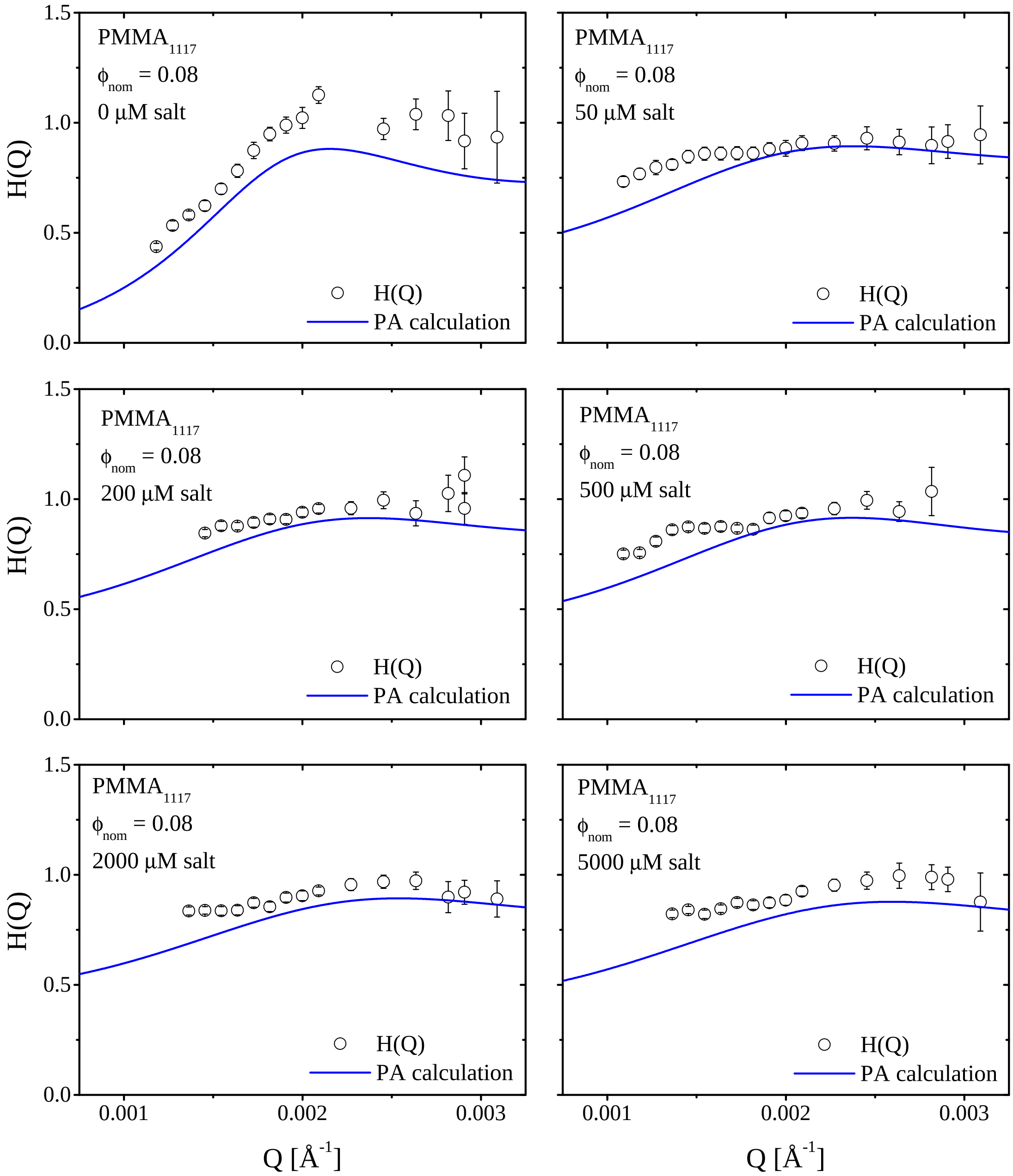

Figure 5.37.: Hydrodynamic functions $H(Q)$ as a function of momentum transfer Q of system PMMA$_{1117}$ for a nominal volume fraction ϕ_{nom} of 0.08. The electrolyte concentrations of the samples are 0 µM, 50 µM, 200 µM, 500 µM, 2000 µM and 5000 µM. The blue lines show the predictions of the pairwise additive approximation using the measured static structure as input.

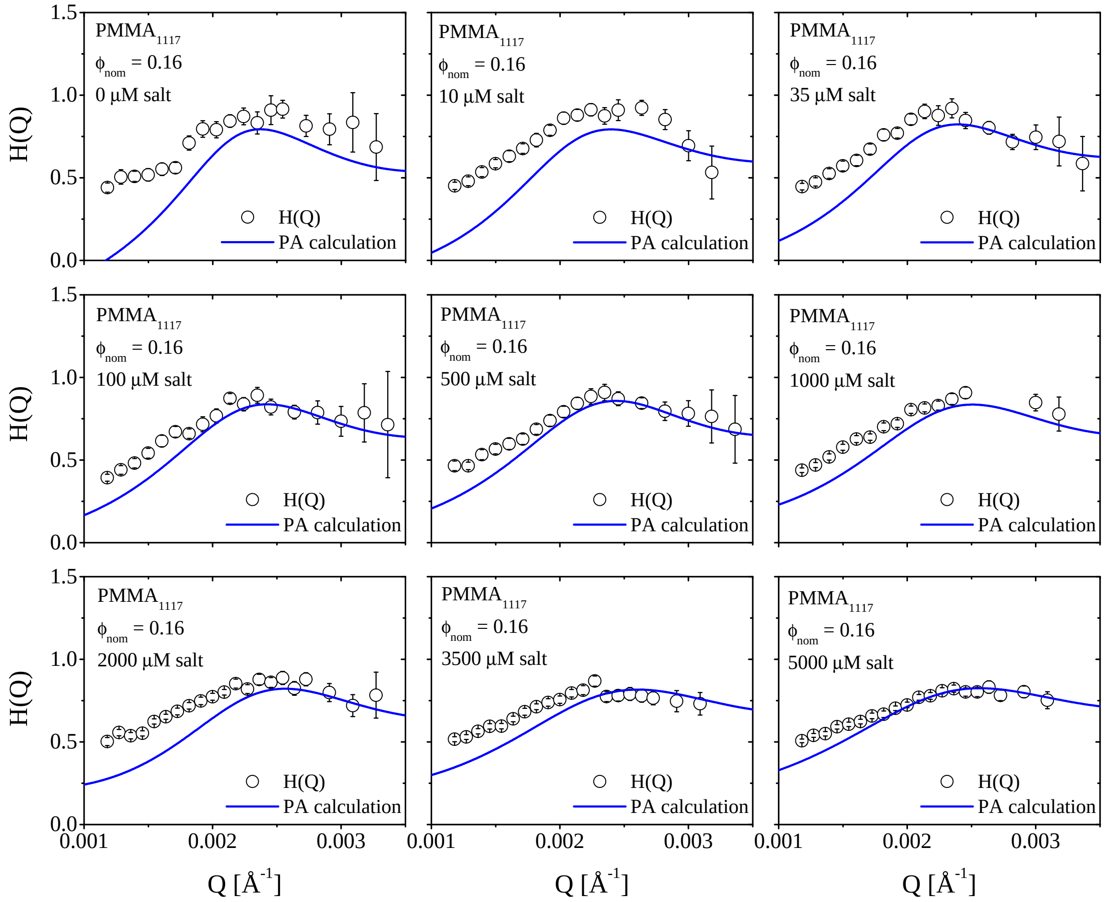

Figure 5.38.: Hydrodynamic functions $H(Q)$ as a function of momentum transfer Q of system PMMA$_{1117}$ for a nominal volume fraction ϕ_{nom} of 0.16. The electrolyte concentrations of the samples are 0 µM, 10 µM, 35 µM, 100 µM, 500 µM, 1000 µM, 2000 µM, 3500 µM and 5000 µM. The blue lines show the predictions of the pairwise additive approximation using the measured static structure as input.

maximum of the hydrodynamic functions as well as the overall shape of $H(Q)$ are well characterized.

With increasing volume fraction $\phi \geq 0.06$, the calculated pairwise additive approximation underestimates the height of the hydrodynamic function $H(Q)$, as depicted in fig. 5.37 for samples of system PMMA$_{1117}$. As the validity of the pairwise additive approximation is restricted for systems of volume fraction $\phi \lesssim 0.1$, it in fact starts to fail in describing the data at a nominal volume fraction $\phi_{\text{nom}} = 0.16$ (fig. 5.38), where it calculates unphysical negative values for the sample with an electrolyte concentration of 0 µM.

For samples of nominal volume fractions $0.001 \leq \phi_{\text{nom}} \leq 0.012$, the pairwise additive approximation has also been fitted to the data. The constant input parameters were the mean radius R_0 =542 Å, the temperature $T = 293.15$ K, the dielectric per-

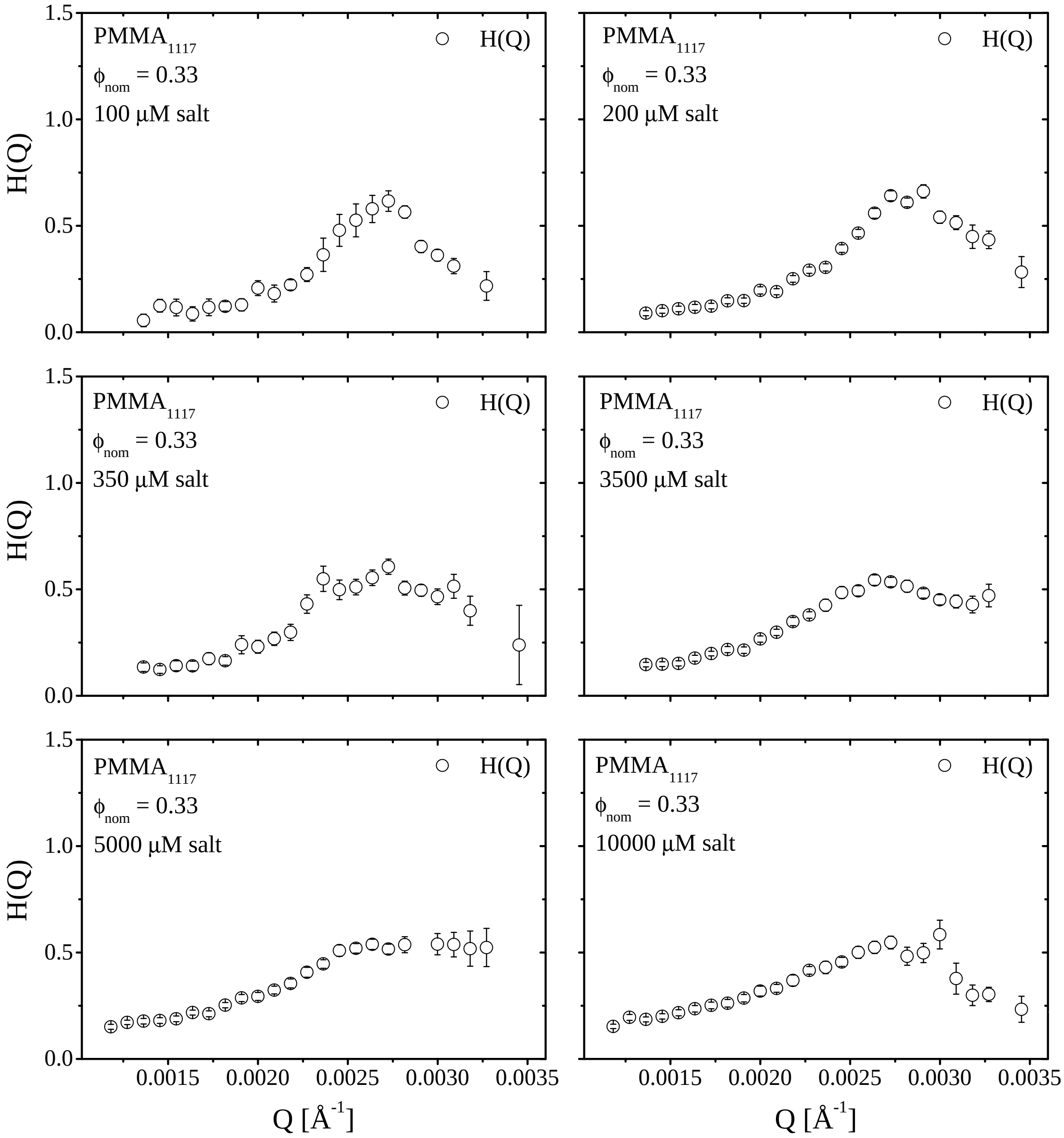

Figure 5.39.: Hydrodynamic functions $H(Q)$ as a function of momentum transfer Q of system PMMA$_{1117}$ for a nominal volume fraction ϕ_{nom} of 0.33. The electrolyte concentrations of the samples are 100 μM, 200 μM, 350 μM, 3500 μM, 5000 μM and 10 000 μM.

Table 5.6.: Nominal volume fraction ϕ, electrolyte concentration, height of the peak of the hydrodynamic function $H(Q_{max})$, parameters yielded by a fit of the RMSA model to the static structure factor $S(Q)$ of system PMMA$_{542}$ and parameters yielded by a fit of the pairwise-additive approximation to the extracted hydrodynamic function. The temperature $T = 293.15\,\mathrm{K}$, the dielectric permittivity of the dispersion medium $\epsilon_r = 80.1$, the mean radius of the particles $R_0 = 542\,\mathrm{Å}$ and the concentration of added electrolyte were kept constant.

ϕ_{nom}	Salt$_{\mathrm{nom}}$ [µM]	RMSA-ϕ	RMSA-Z_{eff}	PA-ϕ	PA-Z_{eff}	$H(Q_{max})$
0.001	0	0.0010	214	0.0011	110	1.05
0.001	10	0.0010	224	0.0020	301	1.02
0.002	0	0.0027	381	0.0025	399	1.11
0.002	10	0.0021	461	0.0022	530	1.04
0.002	50	0.0016	706	0.0019	1593	1.02
0.002	100	0.0018	747	0.0018	2158	1.01
0.004	5	0.0052	432	0.0055	423	1.12
0.004	10	0.0049	267	0.0053	234	1.05
0.004	50	0.0030	572	0.0030	501	1.02
0.008	5	0.0089	487	0.0078	325	1.15
0.008	10	0.0115	497	0.0101	315	1.14
0.008	20	0.0084	510	0.0083	420	1.10
0.008	50	0.0053	722	0.0045	729	1.03
0.012	10	0.0135	710	0.0115	424	1.19
0.012	20	0.0106	602	0.0110	336	1.12
0.012	50	0.0112	483	0.0126	224	1.05

mittivity of the dispersion medium water at 293.15 K $\epsilon_r = 80.1$ and the electrolyte concentration while the volume fraction ϕ and the effective charge Z_{eff} were varied during the fit procedure. The resulting hydrodynamic functions are shown in fig. 5.32 to fig. 5.36 by the solid red lines, the resulting parameters are listed in table 5.6 together with the values obtained by a fit of the rescaled mean spherical approximation to the static structure factor $S(Q)$.

The parameters are in good agreement with the values obtained by the RMSA model fits to the static structure factors of the samples. The obtained volume fractions were very close to the values obtained by the RMSA model fits to $S(Q)$ except for the sample at a nominal volume fraction ϕ of 0.001 and a nominal salt concentration of 10 µM. For this sample ϕ shows a strong deviation and overestimates the concentration of the colloidal particles by a factor of two, which might be explained by the fact that the extracted hydrodynamic function is close to unity for all momentum transfers as shown in fig. 5.32.

The values obtained for the effective charge Z_{eff} are also in reasonably good agreement with the values obtained by a fit to the static structure factor except for the high salt systems at $\phi_{\mathrm{nom}} = 0.002$ and for the samples of $\phi_{\mathrm{nom}} = 0.012$.

5.3.2. $\delta\gamma$-expansion

Since the pairwise-additive approximation, taking into account only two-body hydrodynamic interactions, is not able to describe the hydrodynamic behavior of the more concentrated colloidal systems, the fluctuation- or $\delta\gamma$-expansion was used. This theory, developed originally by *Beenakker* and *Mazur* for hard-sphere suspensions, takes into account many-body interactions between the colloidal particles (Beenakker and Mazur, 1983, 1984). The resulting hydrodynamic function depends on the radius R, volume fraction ϕ and the static structure factor of the sample and is given by eq. (3.46) and eq. (3.47).

To adopt the $\delta\gamma$-expansion for an electrostatically interacting system, the measured static structure factors $S(Q)$ were used as inputs for the $\delta\gamma$-expansion to zeroth order. The resulting hydrodynamic functions are shown in fig. 5.40 to fig. 5.44 for system PMMA_{542} and fig. 5.45 to fig. 5.47 for system PMMA_{1117}.

For nominal volume fractions $0.001 \leq \phi_{\mathrm{nom}} \leq 0.012$ of system PMMA_{542} the calculated hydrodynamic functions by the $\delta\gamma$-expansion coincide nicely with the extracted hydrodynamic functions of the system. The position and the magnitude of the peak of the hydrodynamic function $H(Q_{max})$ as well as the overall shape is well captured by the $\delta\gamma$-expansion.

The samples with higher nominal volume fractions $0.08 \leq \phi_{\mathrm{nom}} \leq 0.33$ show some discrepancies between the calculated model hydrodynamic functions of the $\delta\gamma$-expansion and the measured hydrodynamic functions. The overall shape and position of the peak of the hydrodynamic function is in reasonable agreement with the extracted experimental values. For the samples measured with a nominal volume fractions ϕ_{nom} of 0.08 to 0.16, (shown in fig. 5.45 and fig. 5.46) the measured hydrodynamic functions displays higher values as predicted by the $\delta\gamma$-expansion. Just for the nominal volume fraction $\phi_{\mathrm{nom}} = 0.33$ (fig. 5.47) the predicted and the measured hydrodynamic functions show approximately the same magnitude.

5.3.3. Small-Q approximation of the $\delta\gamma$-expansion

In order to describe the observed deviations of the measured hydrodynamic function $H(Q)$ from the $\delta\gamma$-expansion, the fluctuation-expansion is approximated for small momentum transfers Q yielding eq. (3.48) (Riese *et al.*, 2000b), where the prefactor $\tilde{D} = \mu^{*} 6\pi\eta R$ is depending on the viscosity η of the suspending medium and on the prefactor μ^{*} of the effective mobility tensor $\tilde{\mu}_{ij}^{eff}$ in the small-Q limit.

By using the small-Q approximation of the $\delta\gamma$-expansion it is possible to characterize the measured hydrodynamic functions using the prefactor $\tilde{D}$ as the only fit

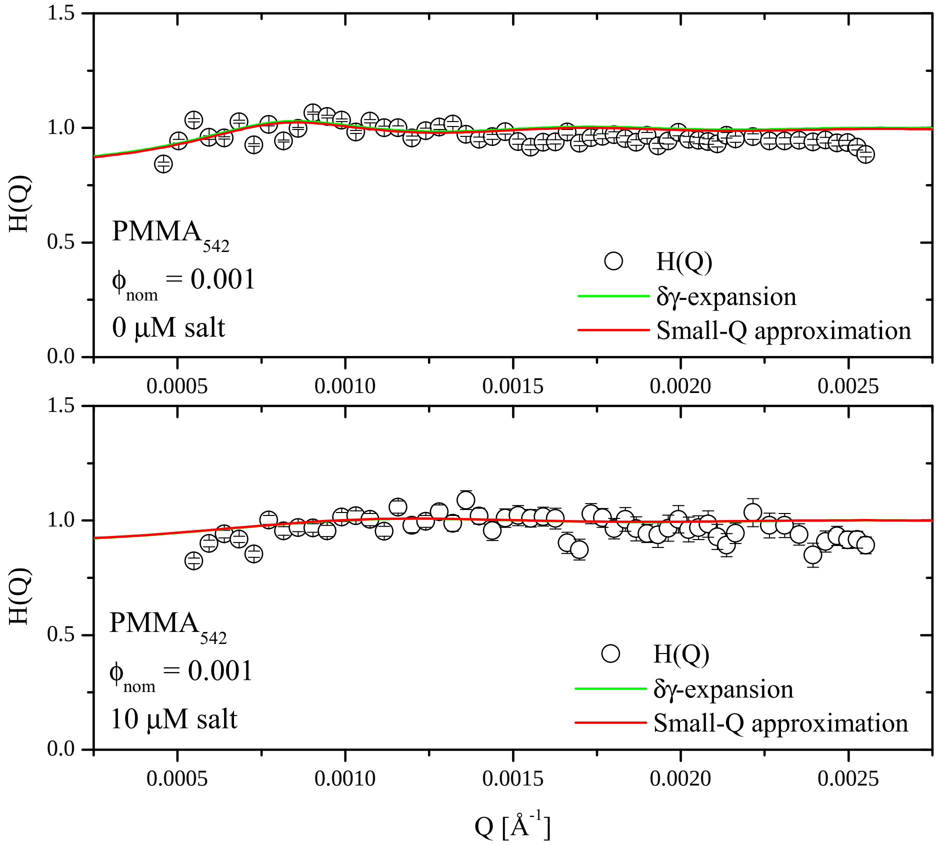

Figure 5.40.: Hydrodynamic functions $H(Q)$ as a function of momentum transfer Q of system PMMA$_{542}$ for a nominal volume fraction ϕ_{nom} of 0.001. The electrolyte concentrations of the samples are 0 μM and 10 μM. The solid green line shows the predicted $\delta\gamma$-expansion using the measured static structure factor $S(Q)$ as input, the red line shows a fit to the hydrodynamic function using the small-Q approximation of the $\delta\gamma$-expansion.

parameter. The results of a fit of eq. (3.48) to the extracted hydrodynamic functions is shown in fig. 5.40 to fig. 5.47 by the solid red lines.

For nominal volume fractions ranging from $0.001 \leq \phi_{\text{nom}} \leq 0.012$ the fits of the small-Q approximation are in good agreement with the hydrodynamic functions over the whole Q range.

The agreement of the small-Q approximation with the measured hydrodynamic functions is also good for the samples of nominal volume fractions $0.08 \leq \phi_{\text{nom}} \leq 0.33$. The magnitude as well as the position of the peak of the hydrodynamic functions is well described by the small-Q approximation of the $\delta\gamma$-expansion. At a nominal volume fraction $\phi_{\text{nom}} = 0.33$ deviations from the measured hydrodynamic functions can be seen for small Q-values.

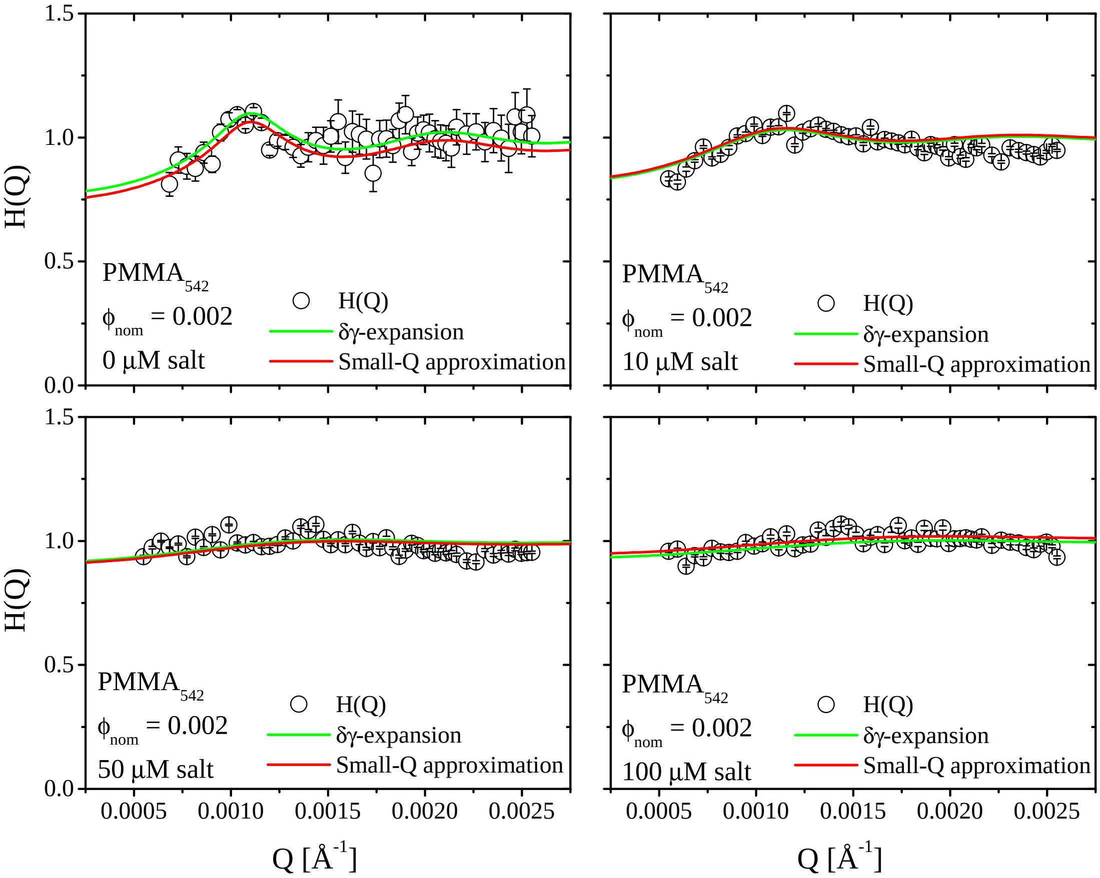

Figure 5.41.: Hydrodynamic functions $H(Q)$ as a function of momentum transfer Q of system PMMA$_{542}$ for a nominal volume fraction ϕ_{nom} of 0.002. The electrolyte concentrations of the samples are 0 µM, 10 µM, 50 µM and 100 µM. The solid green line shows the predicted $\delta\gamma$-expansion using the measured static structure factor $S(Q)$ as input, the red line shows a fit to the hydrodynamic function using the small-Q approximation of the $\delta\gamma$-expansion.

The $\tilde{D}_{HS}$ of a hard-sphere system with short-range interparticle interactions can be calculated using eq. (3.49) and is solely depending on the volume fraction of the colloidal particles. The resulting $\tilde{D}$ values and the ratio of $\tilde{D}_{HS}/\tilde{D}$ are given in table 5.7.

The results for $\tilde{D}$ display an decrease with increasing volume fraction ϕ over the whole range of samples, indicating thus a decrease of the particle mobility with increasing volume fraction.

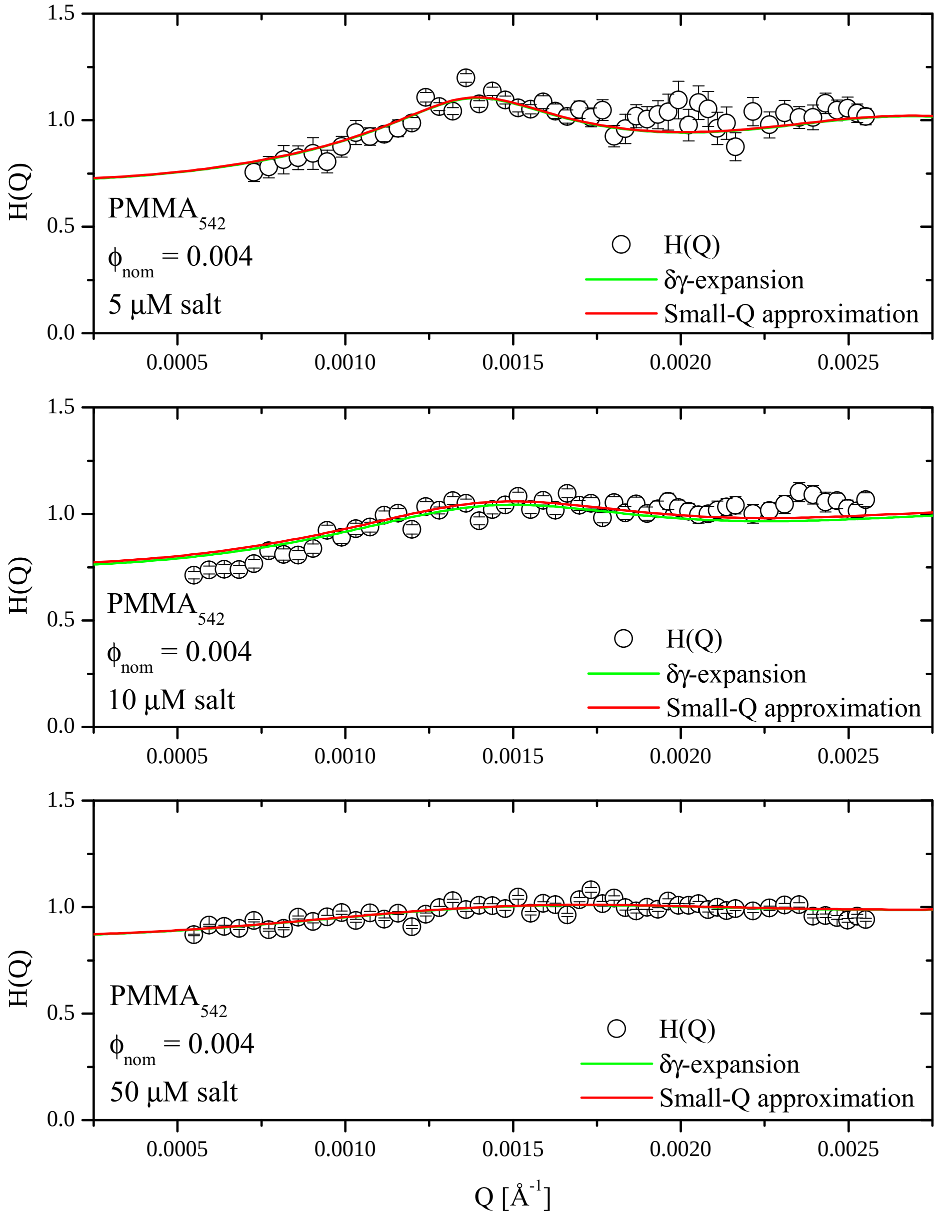

Figure 5.42.: Hydrodynamic functions $H(Q)$ as a function of momentum transfer Q of system PMMA$_{542}$ for a nominal volume fraction ϕ_{nom} of 0.004. The electrolyte concentrations of the samples are 5 µM, 10 µM and 50 µM. The solid green line shows the predicted $\delta\gamma$-expansion using the measured static structure factor $S(Q)$ as input, the red line shows a fit to the hydrodynamic function using the small-Q approximation of the $\delta\gamma$-expansion.

Table 5.7.: Nominal volume fraction ϕ_{nom}, electrolyte concentration, peak value of the hydrodynamic function $H(Q_{max})$, volume fraction determined by the RMSA fit to the static structure factors $S(Q)$, $\tilde{D}$ from a fit of the small-Q approximation to the data and ratio $\tilde{D}_{HS}/\tilde{D}$.

ϕ_{nom}	Salt [µM]	ϕ	$H(Q_{max})$	$\tilde{D}$	$\tilde{D}_{HS}/\tilde{D}$
0.001	0	0.0010	1.05	0.99	1.01
0.001	10	0.0009	1.02	1.00	1.00
0.002	0	0.0027	1.11	0.96	1.03
0.002	10	0.0021	1.04	1.00	0.99
0.002	50	0.0016	1.02	0.99	1.01
0.002	100	0.0019	1.01	1.01	0.98
0.004	5	0.0052	1.12	0.99	1.00
0.004	10	0.0049	1.05	1.00	0.98
0.004	50	0.0031	1.02	0.99	1.00
0.008	5	0.0089	1.15	0.98	0.99
0.008	10	0.0115	1.14	0.98	1.00
0.008	20	0.0084	1.10	0.98	1.00
0.008	50	0.0055	1.03	0.99	0.99
0.012	10	0.0137	1.19	0.97	1.00
0.012	20	0.0107	1.12	0.97	1.00
0.012	50	0.0118	1.05	0.94	1.03
0.08	0	0.113	1.03	0.91	0.81
0.08	50	0.078	0.93	0.87	0.92
0.08	200	0.075	0.97	0.93	0.87
0.08	500	0.081	0.97	0.91	0.87
0.08	2000	0.094	0.97	0.90	0.88
0.08	5000	0.090	0.97	0.92	0.85
0.16	0	0.174	0.91	0.77	0.80
0.16	10	0.163	0.91	0.77	0.83
0.16	35	0.161	0.90	0.77	0.84
0.16	100	0.163	0.87	0.74	0.86
0.16	500	0.165	0.88	0.76	0.83
0.16	1000	0.164	0.88	0.78	0.82
0.16	2000	0.162	0.87	0.77	0.83
0.16	3500	0.144	0.83	0.74	0.90
0.16	5000	0.141	0.82	0.75	0.91
0.33	100	0.376	0.61	0.32	1.09
0.33	200	0.376	0.61	0.37	0.88
0.33	350	0.356	0.59	0.39	0.90
0.33	3500	0.324	0.54	0.39	1.03
0.33	5000	0.326	0.54	0.44	0.97
0.33	10000	0.285	0.53	0.39	1.09

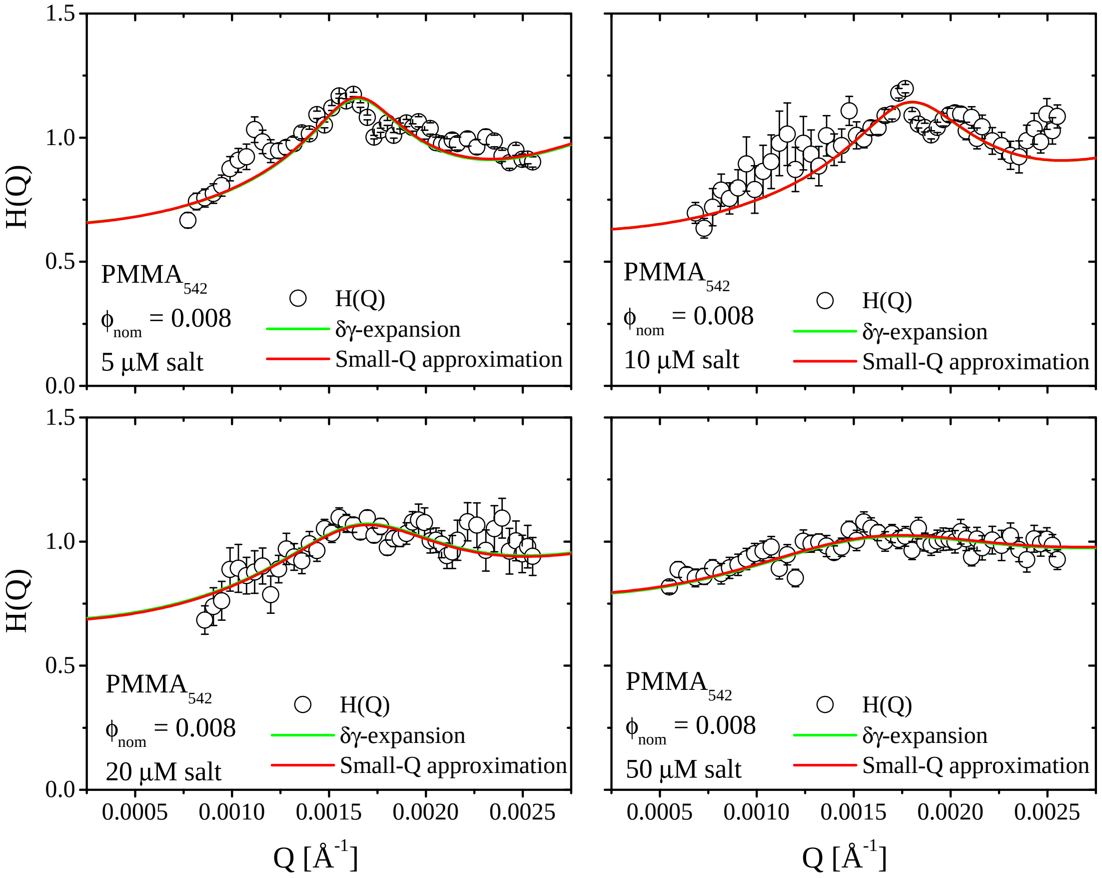

Figure 5.43.: Hydrodynamic functions $H(Q)$ as a function of momentum transfer Q of system PMMA$_{542}$ for a nominal volume fraction ϕ_{nom} of 0.008. The electrolyte concentrations of the samples are 5 µM, 10 µM, 20 µM and 50 µM. The solid green line shows the predicted $\delta\gamma$-expansion using the measured static structure factor $S(Q)$ as input, the red line shows a fit to the hydrodynamic function using the small-Q approximation of the $\delta\gamma$-expansion.

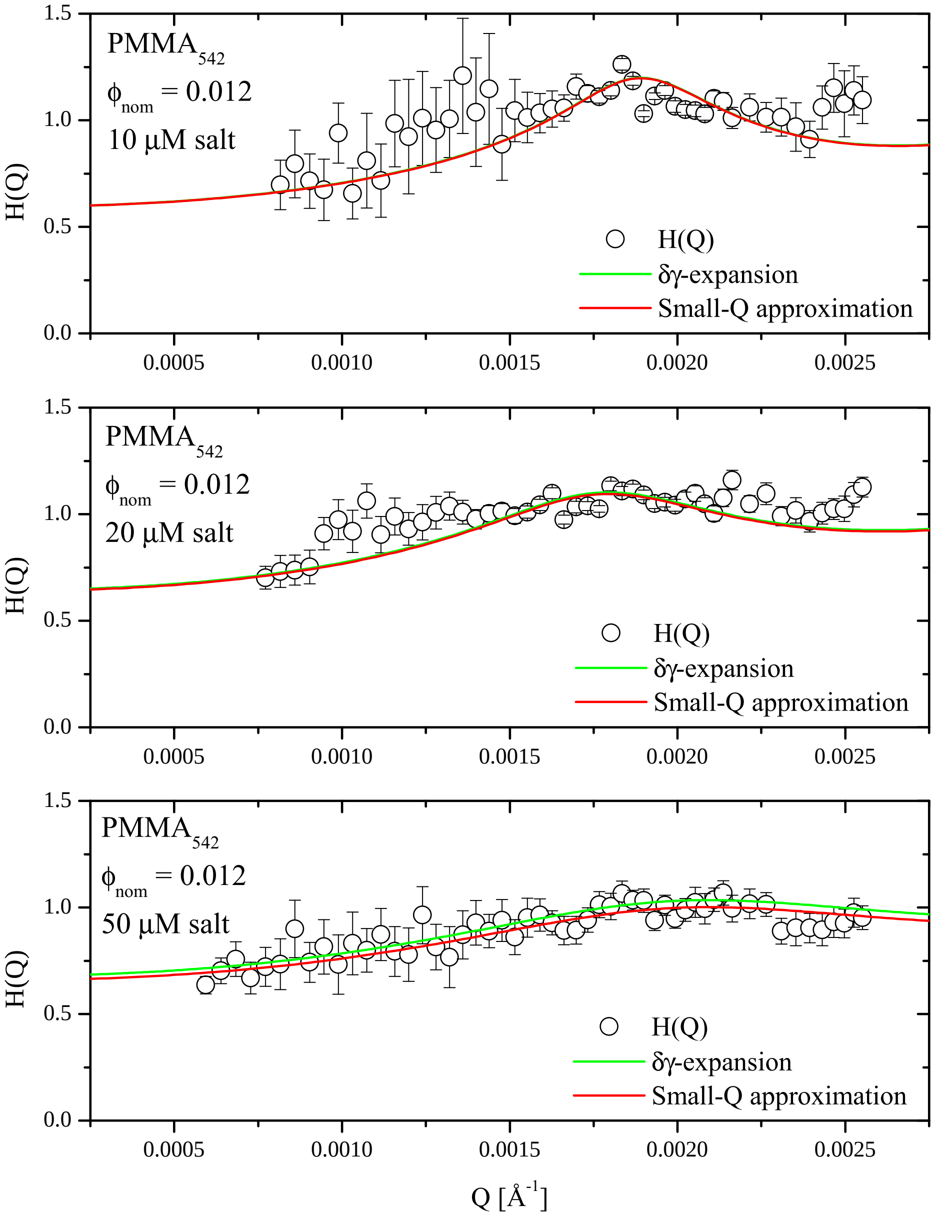

Figure 5.44.: Hydrodynamic functions $H(Q)$ as a function of momentum transfer Q of system PMMA$_{542}$ for a nominal volume fraction ϕ_{nom} of 0.012. The electrolyte concentrations of the samples are 10 µM, 20 µM and 50 µM. The solid green line shows the predicted $\delta\gamma$-expansion using the measured static structure factor $S(Q)$ as input, the red line shows a fit to the hydrodynamic function using the small-Q approximation of the $\delta\gamma$-expansion.

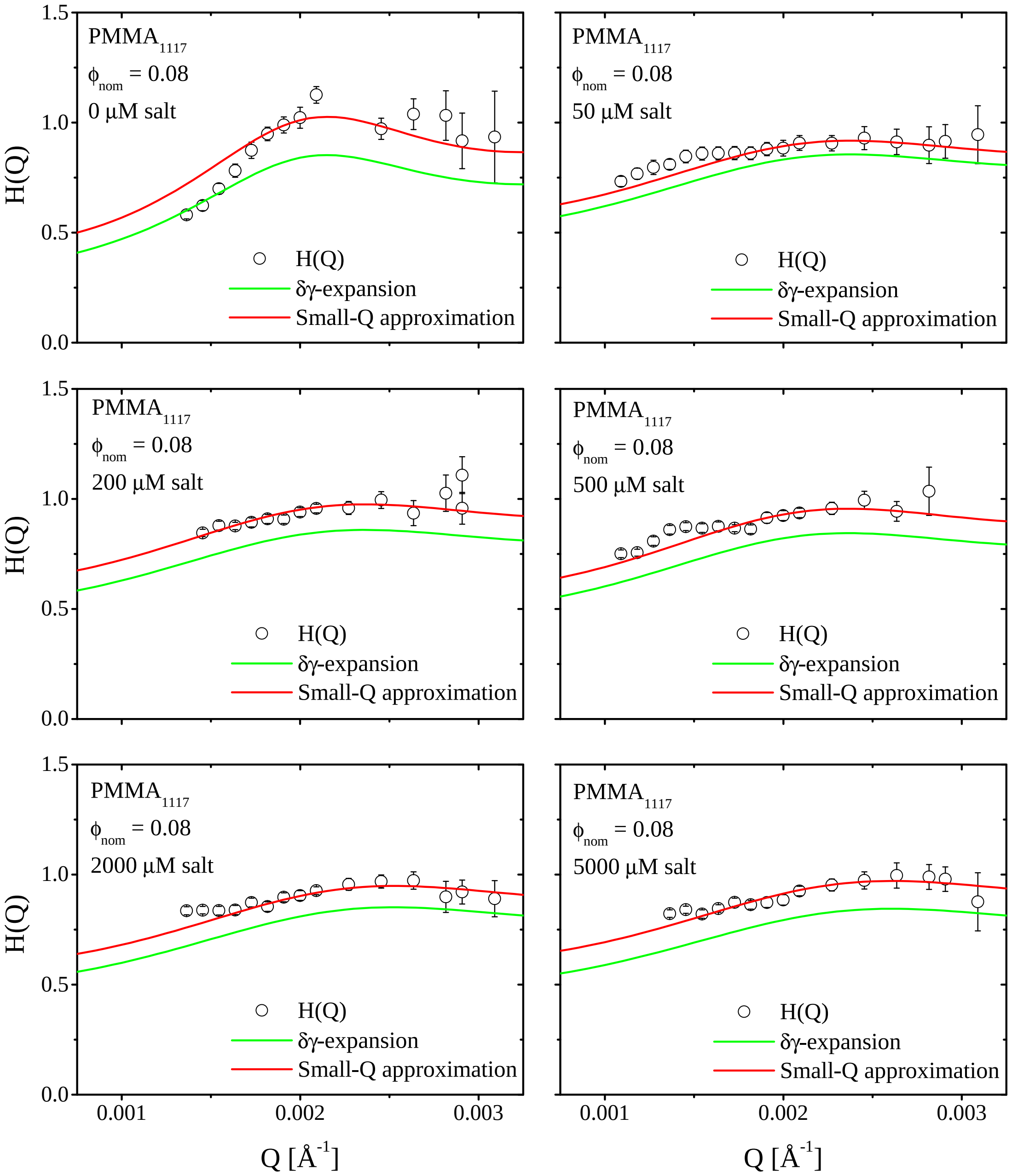

Figure 5.45.: Hydrodynamic functions $H(Q)$ as a function of momentum transfer Q of system PMMA$_{1117}$ for a nominal volume fraction ϕ_{nom} of 0.08. The electrolyte concentrations of the samples are 0 µM, 50 µM, 200 µM, 500 µM, 2000 µM and 5000 µM. The solid green line shows the predicted $\delta\gamma$-expansion using the measured static structure factor $S(Q)$ as input, the red line shows a fit to the hydrodynamic function using the small-Q approximation of the $\delta\gamma$-expansion.

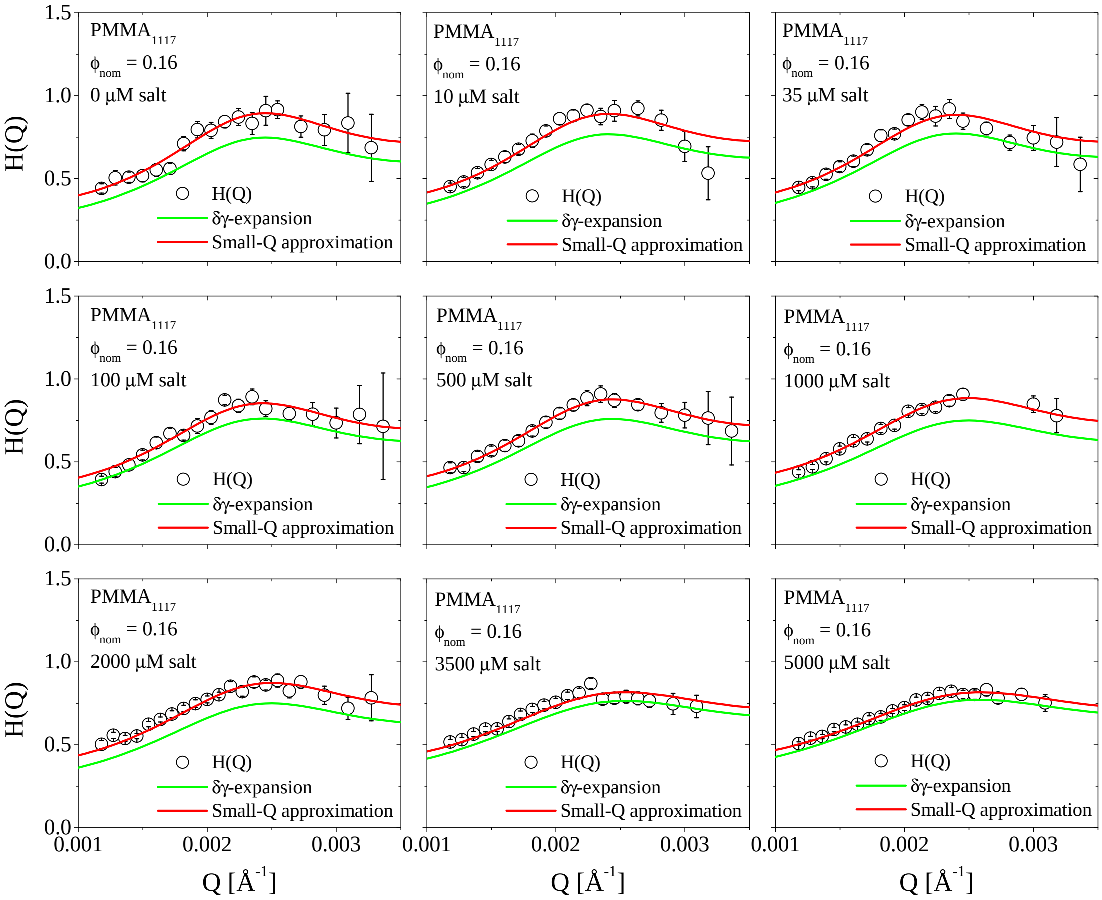

Figure 5.46.: Hydrodynamic functions $H(Q)$ as a function of momentum transfer Q of system PMMA$_{1117}$ for a nominal volume fraction ϕ_{nom} of 0.16. The electrolyte concentrations of the samples are 0 µM, 10 µM, 35 µM, 100 µM, 500 µM, 1000 µM, 2000 µM, 3500 µM and 5000 µM. The solid green line shows the predicted $\delta\gamma$-expansion using the measured static structure factor $S(Q)$ as input, the red line shows a fit to the hydrodynamic function using the small-Q approximation of the $\delta\gamma$-expansion.

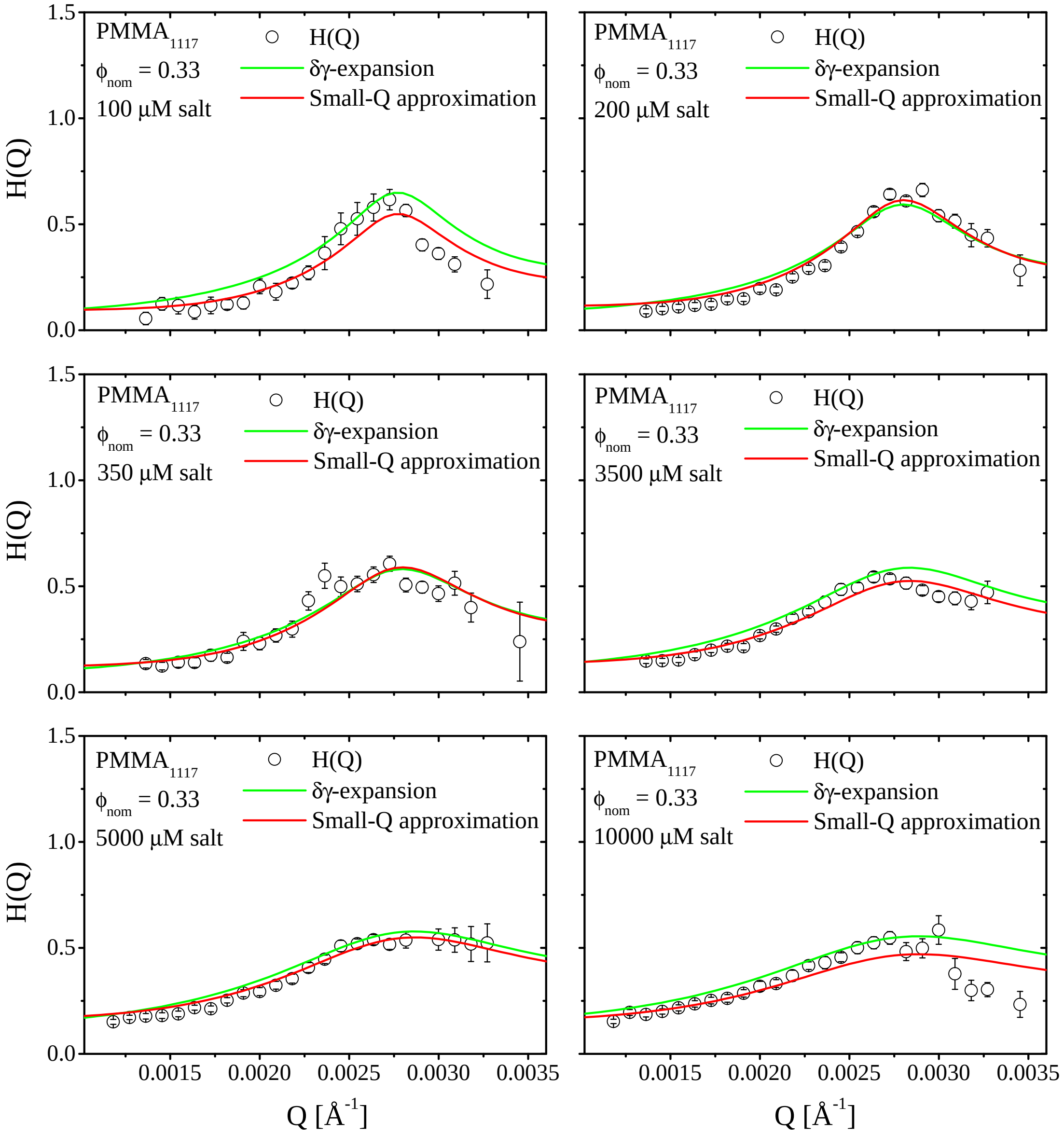

Figure 5.47.: Hydrodynamic functions $H(Q)$ as a function of momentum transfer Q of system PMMA$_{1117}$ for a nominal volume fraction ϕ_{nom} of 0.33. The electrolyte concentrations of the samples are 100 µM, 200 µM, 350 µM, 3500 µM, 5000 µM and 10 000 µM. The solid green line shows the predicted $\delta\gamma$-expansion using the measured static structure factor $S(Q)$ as input, the red line shows a fit to the hydrodynamic function using the small-Q approximation of the $\delta\gamma$-expansion.

5.3.4. Discussion of the hydrodynamic behavior

The extracted hydrodynamic functions are all peaked functions which display maxima $H(Q_{max})$ at the position of the mean particle distance. This feature is more pronounced for stronger direct particle interactions corresponding to higher peak values of the static structure factor. The maximum of the extracted hydrodynamic functions $H(Q_{max})$ as a function of the volume fraction ϕ is plotted in fig. 5.48.
The behavior of a hard-sphere case is well approximated by (Banchio *et al.*, 1999)

$$H(Q_{max}) = 1 - 1.35\phi. \tag{5.7}$$

This expression was derived using a *Verlet-Weiss* correction to the static structure factor of a hard-sphere system. An upper limit for the peak value of the hydrodynamic function $H(Q_{max})$ was obtained by using the $\delta\gamma$-expansion with help of a RMSA static structure factor $S(Q)$ as input as proposed by *Gapinski et al.* (Gapinski *et al.*, 2010). The static structure factors $S(Q)$ were calculated for different volume fractions ϕ using the respective parameters for the two systems assuming a deionized solution of colloidal particles (added electrolyte concentration = 0 µM). The effective charge was varied until a peak value of the static structure factor $S(Q_{max}) \approx 2.85$ was found, the cutoff value for the onset of crystallization. The resulting upper limits for both systems are very similar for all volume fractions so that just the average upper limit for both systems is displayed in fig. 5.48.

The peak values of the hydrodynamic functions $H(Q_{max})$ are within the limits of the theoretical maxima of the hydrodynamic functions given by the two limiting cases. Just for the highest nominal volume fraction $\phi_{\text{nom}} = 0.33$ one sample with an electrolyte concentration of 10 000 µM is below the theoretically expected value of a hard sphere system. A strong slowing down of the colloidal systems below the hard sphere behavior, as previously found by *Robert et al.* (Robert *et al.*, 2008) and *Grübel et al.* (Grübel *et al.*, 2000), is not observed for the samples probed here.

The peak value of the hydrodynamic function $H(Q_{max})$ depends on the volume fraction. $H(Q_{max})$ is larger than unity for small volume fractions ($\phi < 0.02$) indicating an increase of the particle mobility due to the indirect hydrodynamic interactions. For samples with a volume fraction $\phi > 0.06$ the maximum of the hydrodynamic function is smaller than unity, indicative of a slowing down of the system. This holds except for one deionised sample at a nominal volume fraction $\phi_{\text{nom}} = 0.08$.

In order to illustrate the $H(Q_{max})$ dependence on the electrolyte concentration, the results for both systems PMMA_{542} and PMMA_{1117} have been sorted according to the salt concentration as shown in fig. 5.49.

The volume fractions ϕ have been binned for this figure: All samples of one nominal volume fraction have been set to the mean volume fraction ϕ_{mean} of this set of samples, the error bars were calculated using the difference between this new ϕ_{mean} and the volume fraction ϕ given by the RMSA model fit to the static structure factor.

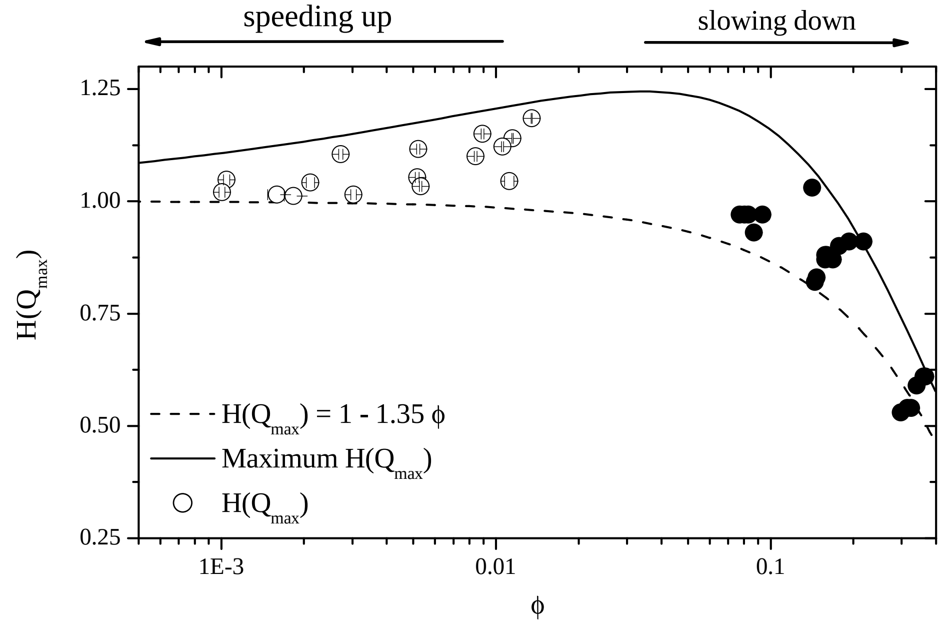

Figure 5.48.: Peak value of the hydrodynamic function $H(Q_{max})$ as a function of the volume fraction ϕ. Filled symbols refer to system PMMA$_{1117}$, open symbols refer to system PMMA$_{542}$. The solid line indicates the maximum peak value of $H(Q_{max})$ calculated with the $\delta\gamma$-expansion using a calculated RMSA structure factor as input, the dashed line is the predicted behavior of a hard sphere system (eq. (5.7)).

A clear dependence on the electrolyte concentration in the suspension can be seen for the whole range of concentrations The maximum of the hydrodynamic function $H(Q_{max})$ decreases with increasing electrolyte concentration which is the result of the enhanced screening of the direct particle interactions. The samples (for a given mean volume fraction ϕ_{mean}) which have the lowest concentration of electrolyte are closest to the theoretical maximum peak values of $H(Q)$: The samples with the highest salt concentration are closest to the hard-sphere prediction. Just in one case for a nominal volume fraction of $\phi = 0.08$ one sample shows a lower peak value $H(Q_{max})$ than samples at the same nominal volume fraction and higher salt concentration.

The trend towards hard sphere behavior for increased screening of the electrostatical interactions is expected by accelerated Stokesian dynamics simulations (Banchio *et al.*, 2006) and has been also found experimentally by *Gapinski et al* (Gapinski *et al.*, 2009) for a volume fraction range $0.07 \leq \phi \leq 0.14$. The evolution of the peak value of the hydrodynamic function as a function of the electrolyte concentration is further illustrated in fig. 5.50.

By comparing the sample series of the two systems PMMA$_{1117}$ and PMMA$_{542}$ individually, the decrease of the peak values $H(Q_{max})$ seems to be more pronounced

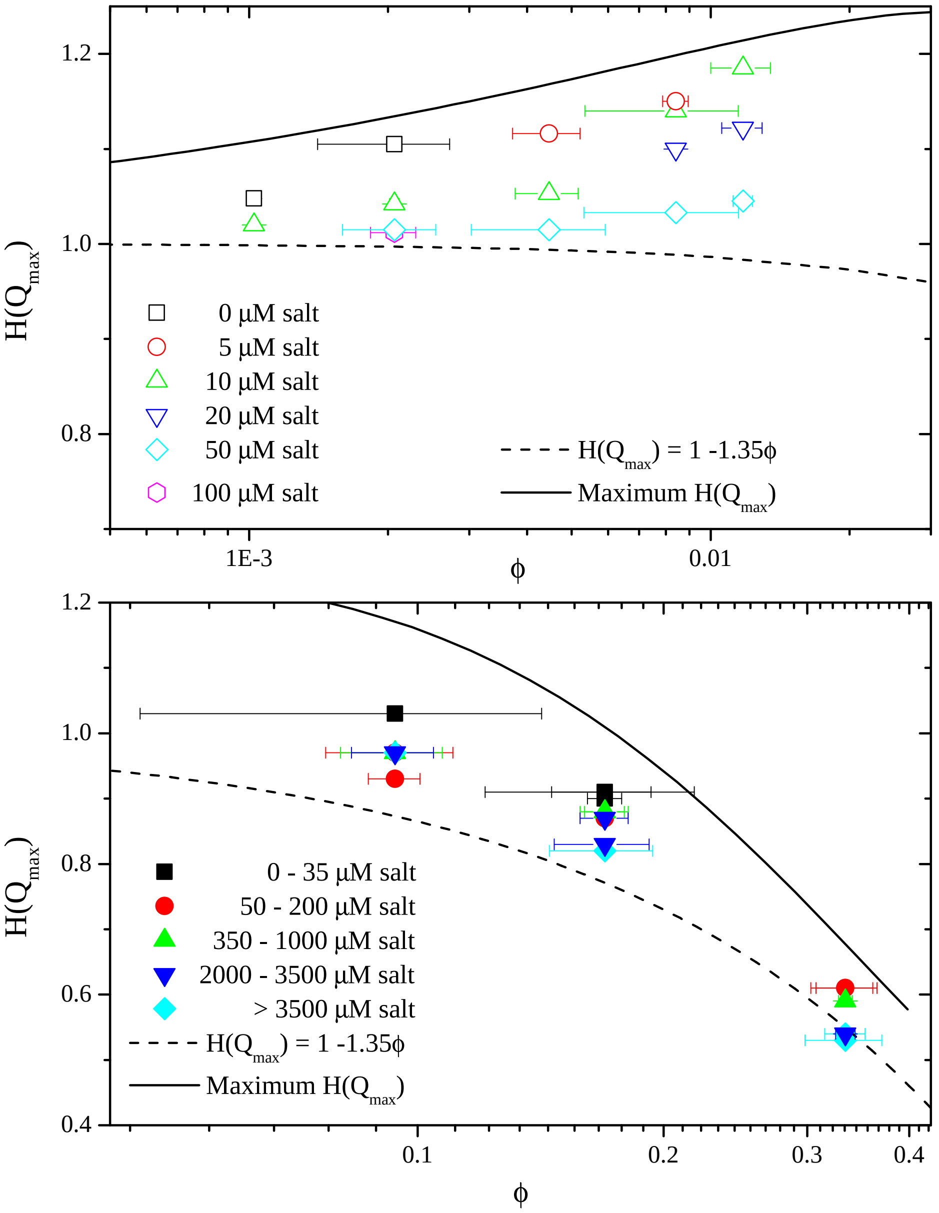

Figure 5.49.: Peak value of the hydrodynamic functions $H(Q_{max})$ as a function of the volume fraction ϕ. The different colors and symbols indicate the amount of electrolyte. Top: Samples of a nominal volume fraction $0.001 \leq \phi_{\text{nom}} \leq 0.012$. Bottom: Samples of a nominal volume fraction $0.08 \leq \phi_{\text{nom}} \leq 0.33$. Filled symbols refer to system PMMA_{1117}, open symbols refer to system PMMA_{542}. The solid lines are the maximum peak values of $H(Q_{max})$, the dashed line is the predicted behavior of a hard sphere system (eq. (5.7)).

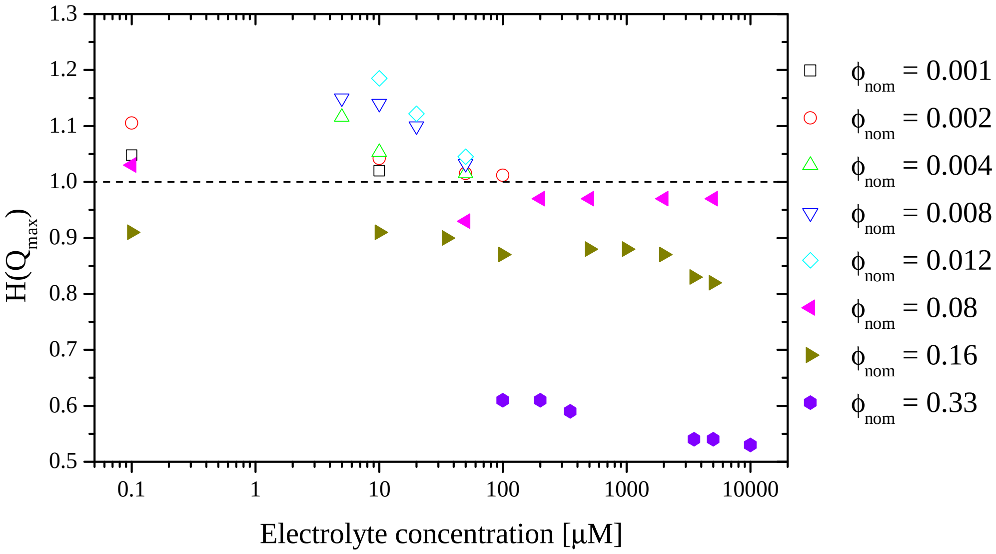

Figure 5.50.: Peak value of the hydrodynamic functions $H(Q_{max})$ as a function of the electrolyte concentration for eight volume fractions. Filled symbols refer to system PMMA$_{1117}$, open symbols refer to system PMMA$_{542}$. The dashed lines indicates $H(Q_{max}) = 1$. The samples at a nominal salt concentration of 0 µM have been plotted at 0.1 µM, corresponding to the self dissociation of the dispersion medium water at a neutral pH-value of 7.

for sample series with higher volume fractions exhibiting stronger direct interparticle interactions when compared to less concentrated sample series of the same system. This effect has also been reported by *Gapinski et al.* (Gapinski *et al.*, 2009).

The hydrodynamic functions $H(Q)$ for $\phi < 0.02$ could be modeled quantitatively within the pairwise-additive approximation (see fig. 5.32 to fig. 5.39). Already the calculated hydrodynamic functions showed a good agreement with the data, a fit of the pairwise-additive approximation to the data gave only minor deviations from the system parameters. This model, which takes into account only two body-interactions, fails however for samples of higher volume fractions, where many-body interactions play a significant role in the hydrodynamic behavior of the colloidal systems.

To model these many-body interactions the $\delta\gamma$-expansion to zeroth order (Beenakker and Mazur, 1983, 1984) using the static parameters of the samples as input parameters were calculated, which resulted in a good agreement of the model with the hydrodynamic functions $H(Q)$ for $\phi < 0.02$ (displayed in fig. 5.40 to fig. 5.44). However, at intermediate volume fractions $0.05 < \phi < 0.2$ the $\delta\gamma$-expansion, while qualitatively reflecting the shape and the peak position of the measured hydrodynamic functions, underestimates the values of $H(Q)$ (fig. 5.45 and fig. 5.46). Only for the highest volume fraction ($\phi_{\text{nom}} = 0.33$), displayed in fig. 5.47, the deviations of the calculated $\delta\gamma$-expansion from the measured $H(Q)$ are decreasing again.

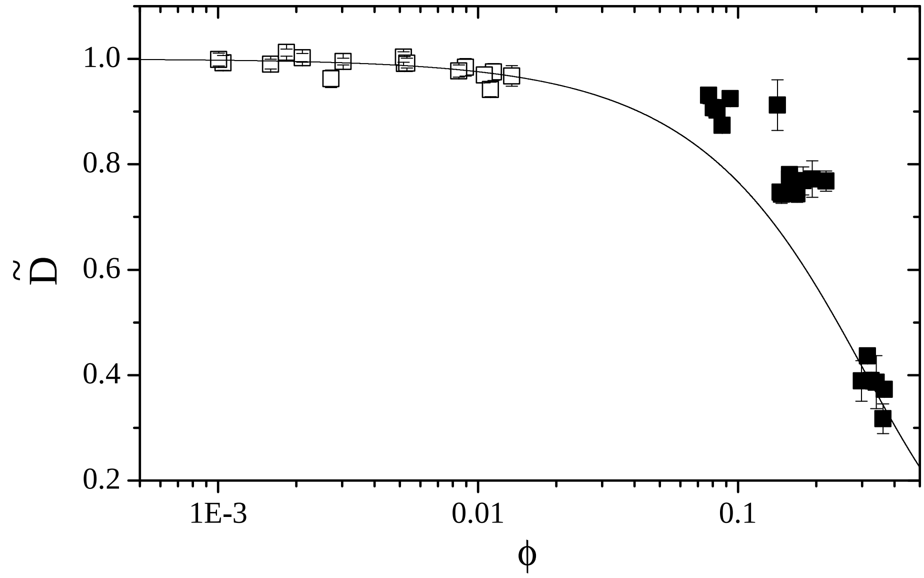

Figure 5.51.: $\tilde{D}$ as a function of the volume fraction ϕ. The solid line is the prediction for a hard sphere system. Filled symbols refer to system PMMA_{1117}, open symbols refer to system PMMA_{542}.

A quantitative description of the samples at higher volume fractions was achieved with the $\delta\gamma$-expansion in the small-Q approximation resulting in a prefactor $\tilde{D}$ which depends on the mobility tensors of the colloidal particles (the fits are displayed in fig. 5.40 to fig. 5.47). The $\tilde{D}$ values for the measured samples and $\tilde{D}_{HS}$ corresponding to the calculated prefactor of a hard sphere system are shown in fig. 5.51 as a function of the volume fraction ϕ .

As can be seen in fig. 5.51, $\tilde{D}$ is decreasing with increasing volume fraction ϕ for all sample concentrations. The $\tilde{D}$ values for the samples with a volume fraction $\phi < 0.02$ and $\phi > 0.25$ are consistent with the theoretical values for a hard sphere system. For the intermediate volume fractions from $0.05 < \phi < 0.2$, the values of $\tilde{D}$ are higher than expected for a hard sphere system, indicating thus an increased short-time self-diffusion due to hydrodynamic interactions. For the most concentrated samples $\phi_{\text{nom}} = 0.33$ the ratio $\tilde{D}_{HS}/\tilde{D}$ is again close to unity.

The enhanced mobility in the volume fraction range of $0.05 < \phi < 0.2$ might be interpreted as a coexistence of far-field and near-field effects. In a hard sphere system, where the hydrodynamic interactions lead to a hindrance of the dynamics, near-field hydrodynamic interactions acting as lubrication forces are of great importance due to the high probability of pairs of nearly touching particles. In contrast, near-field effects are relatively unimportant in dilute systems of electrostatically interacting particles. In these systems, the probability to find two spheres in close proximity is close to zero due to the strong interaction potential. In these systems far-field effects play a dominant role - at a length scale of $2\pi/Q_{max}$ the motion of neighboring particles leads to backflow effect of displaced fluid, leading to an enhancement of the motion of the particles at Q_{max} (Nägele and Baur, 1997; Banchio *et al.*, 1999). While the far-field effects dominate the hydrodynamic behavior of the systems of volume fractions $\phi < 0.02$, the near-field effects are prominent at high volume fractions $\phi = 0.3 - 0.35$. In the intermediate volume fraction range both effects play a role and the extracted hydrodynamic functions show a slowing down ($H(Q) < 1$) while the motions of the system are still considerably faster than the hard sphere behavior.

In general, the peak values of the hydrodynamic functions $H(Q_{max})$ fall into the theoretical range spanned by the hydrodynamic behavior of hard spheres on the one hand and the theoretical maximum of the hydrodynamic functions calculated by the $\delta\gamma$-expansion with an RMSA input on the other hand.

6. Summary and Outlook

Highly-charged poly-acrylate nano-particles have been synthesized using emulsion polymerization and two sample series PMMA_{542} and PMMA_{1117} with different particle radii were studied. These systems interact via long-range electrostatic interactions, which can be screened by the addition of salt to the suspensions. The static and dynamic behavior of these colloidal samples was studied by scattering methods using either visible light or X-rays. Ultra-dilute samples as well as eight different concentrations with different amounts of electrolyte were further investigated at nominal volume fractions ranging from $0.001 \leq \phi_{\text{nom}} \leq 0.33$.

Static small angle X-ray scattering (SAXS) data on ultra-dilute samples were analyzed yielding a mean radius of 542 Å and 1117 Å respectively with a low polydispersity $\Delta R/R_0$ of 0.12 and 0.07 for system PMMA_{542} and PMMA_{1117}, respectively.

At higher concentrations interparticle interactions were observed showing an ordering of the particles for volume fractions from 0.001 to 0.33. The peak of the static structure factor shifted with increasing volume fraction to higher wavevector transfers Q, corresponding to a smaller interparticle spacing. With increasing electrolyte concentration (for the same nominal volume fraction), the position of the $S(Q)$-peak shifted to higher momentum transfers Q, indicating a relative relaxation of the particle positions. The same trend was observed for the extrapolated values of $S(0)$, which can be related to the isothermal compressibility of the samples: $S(0)$ is decreasing with increasing volume fraction for both systems PMMA_{542} and PMMA_{1117} and increasing with increasing salt concentration, displaying thus a higher compressibility of the interparticle spacing at lower volume fractions and higher salt concentrations. This observation was further confirmed by the peak values of the static structure factor $S(Q_{max})$, which increased with increasing volume fraction. In addition, $S(Q_{max})$ displayed a clear decrease with increasing salt concentration (for samples of the same nominal volume fraction), as expected for an enhanced screening of the direct particle interactions with increasing salt concentration.

The extracted static structure factors $S(Q)$ were modeled using the rescaled mean spherical approximation (RMSA) giving information on the volume fraction and the effective charge Z_{eff} of the colloidal particles. The calculated RMSA models agree well with the measured static structure factors, characterizing not only the first peak of $S(Q)$ but also the subsequent maxima. The obtained values for the particle concentration were in good agreement with the nominal volume fractions of the samples. The resulting effective charges of the samples increased with increasing electrolyte concentrations. This effect is more pronounced for higher salt concentrations. This observation may be interpreted as the transition from a counterion dominated screening towards a salt ion dominated screening.

Free diffusion of the colloidal particles was studied by dynamic light scattering and X-ray photon correlation spectroscopy yielding Stokes-Einstein diffusion for the two systems. The hydrodynamic radius was slightly bigger than the geometrical radius as extracted by a fit of a polydisperse sphere form factor to the static data. This is usually interpreted by the presence of (temporarily) attached solvent molecules to the surface of the colloidal particles. The effect is more pronounced for system PMMA_{542}. The characterization of the dynamics of samples with direct interparticle interactions allowed the determination of the Q dependent diffusion coefficient $D(Q)$. The normalized inverse diffusion coefficient $D_0/D(Q)$ displays a maximum at momentum transfers Q corresponding to the position of $S(Q_{max})$. This peak indicates a slowing down of the sample dynamics on length scales corresponding to the mean particle spacing as expected by theory. The observation that the dynamic structure factor $D_0/D(Q) \neq S(Q)$ already points out the presence of indirect hydrodynamic interactions in addition to direct particle interactions.

At high momentum transfers Q and thus small length scales, the short-time self diffusion coefficient $D(Q \to \infty) = D^{\mathrm{s,short}}$ was measured. The normalized short-time self diffusion coefficients $D^{\mathrm{s,short}}/D_0$ displays a decrease with increasing particle concentration, giving additional evidence of the presence of hydrodynamic interactions in the samples. The collective short-time diffusion coefficients $D_C = D(Q \to 0)$ normalized to the free diffusion coefficient D_0 was always found to be greater than unity, indicating enhanced collective dynamics as expected by theory. The collective dynamics were furthermore more enhanced in samples with higher direct interparticle interactions, since D_C increased with increasing volume fraction and decreasing salt concentration.

The peak values of the dynamic structure factor increased with increasing volume fraction and decreasing salt concentration and displayed thus also a strong dependence on the strength of the direct interparticle interactions manifested in higher values of $S(Q_{max})$. The highest peak values were measured at the highest nominal volume fraction $\phi_{\mathrm{nom}} = 0.33$.

The extracted hydrodynamic functions are peaked functions and showed thus a dependence on the length scale. The maxima of the hydrodynamic functions $H(Q_{max})$ were located at momentum transfers corresponding to the average particle spacing and were more pronounced in the case of stronger direct particle interactions (larger peak values of the static structure factor). The maximum of the hydrodynamic function $H(Q_{max})$ was depending on the volume fraction. $H(Q_{max})$ is larger than unity for small volume fractions ($\phi < 0.02$) indicating an increase of the mobility of the colloidal particles due to the indirect hydrodynamic interactions on these length scales. For samples of volume fraction $\phi > 0.06$ the maximum of the hydrodynamic function was smaller than unity. This slowing down of the particle dynamics was more pronounced in more concentrated systems. In addition, the extracted hydrodynamic functions showed a clear dependence on the electrolyte concentration in the suspension. With increasing salt concentration, accompanied by an enhanced screening of the direct particle interactions, $H(Q_{max})$ decreased. This evolution towards hard sphere behavior for increased screening of the electrostatical interactions is expected by theory. In general, the peak values of the hydrodynamic functions $H(Q_{max})$ fall between the theoretical limits given by the hydrodynamic behavior of a hard sphere system on the one hand and the theoretical maximum expected for a low salt system of highly charged spherical particles on the other hand.

The hydrodynamic functions for samples with a volume fraction $\phi < 0.02$ (displaying $H(Q_{max}) > 1$) could be described within the truncated pairwise additive approximation, which takes into account only two body-interactions terms. The speeding up of the particles mobility at momentum transfers corresponding to the mean interparticle spacing can be attributed to the dominant role of far-field effects in the hydrodynamic interactions. These are usually interpreted as a backflow of displaced solvent by the motions of neighboring particles on length scales of the mean interparticle spacing which leads to the observed increased mobility of the particles.

The pairwise additive approximation failed to describe the measured hydrodynamic functions $H(Q)$ at higher volume fractions, $\phi > 0.06$, where many-body interactions play a significant role for the hydrodynamic behavior of the colloidal systems. A quantitative description of the samples at these higher volume fractions was achieved by using the $\delta\gamma$-expansion in the small-Q approximation, yielding a mobility that is slightly higher than expected for a pure hard-sphere system in the volume fraction range $0.06 \leq \phi \leq 0.18$. This might be an indication for the coexistence of far-field and near-field effects of the hydrodynamic interactions. For the most concentrated analyzed samples $\phi_{\mathrm{nom}} = 0.33$, the $\delta\gamma$-expansion yields a good description of the data. At elevated volume fractions it is thus possible to screen direct long-range interparticle interaction via the addition of electrolyte and the resulting hydrodynamics is the one of a hard-sphere system, where near-field effects of the hydrodynamic interactions acting as lubrication forces are dominant.

The possibility to tune the direct particle interactions offers the potential to investigate the transition to the glassy or crystalline state. While colloidal systems of high monodispersity often evolve into a crystalline state with strong direct particle interactions, more polydisperse systems can evolve into a glassy state, where the dynamics of the systems are strongly slowed down. These quasi-static samples offer the opportunity to investigate the eventual existence of local symmetries in such disordered systems via the analysis of higher order correlation functions as proposed in the X-ray cross correlation analysis concept (Wochner *et al.*, 2009). A Free Electron Laser (FEL) would offer the possibility to investigate these local symmetries not only in the glassy, but also in the fluid phase over the whole range of colloidal concentrations.

A. $\delta\gamma$-expansion

A theoretical description of the hydrodynamic functions has been derived by *Beenaker* and *Mazur* (Beenakker and Mazur, 1983, 1984) who followed an approach were the mobility tensors $\boldsymbol{\mu}_{ij}(\boldsymbol{r}^N)$, which depend on the configuration of all particles $\boldsymbol{r}^N$, were calculated – the $\delta\gamma$-expansion. The mobility tensors $\boldsymbol{\mu}_{ij}(\boldsymbol{r}^N)$ relate the velocity $\boldsymbol{v}_i$ of a particle to the forces $\boldsymbol{F}_j$ exerted on each particle by the suspending fluid

$$\boldsymbol{v}_i = -\sum_{j=1}^{N} \boldsymbol{\mu}_{ij} \boldsymbol{F}_j. \tag{A.1}$$

While in the case of a dilute suspension the problem can be approximated by only taking into account two-particle hydrodynamic interactions, for concentrated suspensions also many-body interactions have to be taken into account. By a resummation of all hydrodynamic contributions through an expansion of correlation functions of increasing order, *Beenaker* and *Mazur* derived an expression in terms of an ensemble average of the spatial configurations of the particles.

The resulting hydrodynamic function depends on the radius R, the volume fraction ϕ and the static structure factor $S(Q)$ of the sample and is given by

$$\begin{aligned} H(Q) = \frac{D_s(\phi)}{D_0} + \frac{3}{2\pi} \int_0^\infty \mathrm{d}(RQ') \left(\frac{\sin(RQ')}{RQ'} \right)^2 [1 + \phi S_{\gamma 0}(RQ')]^{-1} \\ \times \int_{-1}^{1} \mathrm{d}x \, (1 - x^2)(S|\boldsymbol{Q} - \boldsymbol{Q}'| - 1) \end{aligned} \tag{A.2}$$

where the integration variable x is defined as $x = \cos(\widehat{\boldsymbol{Q}, \boldsymbol{Q}'})$.

The function $S_{\gamma 0}$ depends on the volume fraction via the scalars $\gamma_0^{(l)}$ and is given by

$$S_{\gamma 0}(x) = C(x) + \sum_{p=2}^{\infty} \frac{9}{4} \pi \epsilon_p \left(\frac{\gamma_0^{(p)}}{n/V} - 1 \right) (2p-1)^2 x^{-3} J_{p-1/2}^2(x) \tag{A.3}$$

where J_n is the Bessel function of order n and ϵ_p is

$$\epsilon_p = \begin{cases} 5/9 & p = 2 \\ 1 & p > 2. \end{cases} \tag{A.4}$$

The function $C(x)$ is given by

$$C(x) = \frac{9}{2}\left(\frac{Si(2x)}{x} + \frac{\cos(2x)}{2x^2} + \frac{\sin(2x)}{4x^3} - \frac{\sin^2(x)}{x^4} - \frac{4[\sin(x) - x\cos(x)]^2}{x^6}\right) \tag{A.5}$$

where $Si(x)$ is the sine integral

$$Si(x) = \int_0^x \mathrm{d}t \frac{\sin(t)}{t}. \tag{A.6}$$

The quantities $\gamma_0^{(l)}$ can be calculated from

$$\gamma_0^{(m)} - \gamma_0^{(m)}\phi(2m-1)\int_0^\infty \frac{\mathrm{d}k}{k} J^2_{m-1/2}(k) S_{\gamma 0}(k)[1 + \phi S_{\gamma 0}(k)]^{-1} = \frac{n}{V} \qquad m = 2, 3, \ldots \tag{A.7}$$

To obtain a closed set of equations, the difference $\gamma_0^{(l)} - n/V$ is negelcted for $l > 5$.

The first part of eq. (A.2) is the normalized short-time self diffusion coefficient $D_s(\phi)/D_0$, which is the Q-independent self-part of the hydrodynamic function and is given by

$$\frac{D_s(\phi)}{D_0} = \frac{2}{\pi}\int_0^\infty \mathrm{d}x \left(\frac{\sin(x)}{x}\right)^2 [1 + \phi S_{\gamma 0}(x)]^{-1}. \tag{A.8}$$

B. RMSA results assuming a constant effective charge

The rescaled mean spherical approximation was fitted to the static structure factors assuming a constant effective charge Z_{eff} of $496\,\text{e}^-$ and $221\,\text{e}^-$ per colloid for system PMMA_{542} and PMMA_{1117} respectively. The other input parameters for the model were the temperature $T = 293.15\,\text{K}$, the dielectric permittivity of the dispersion medium $\epsilon_r = 80.1$ and the mean radius of the particles with 542 Å and 1117 Å for system PMMA_{542} and PMMA_{1117} respectively. By keeping the effective charge of the colloidal particles constant, the RMSA model yields the strength of the interaction potential depending on the amount of added ions screening the interparticle interactions. The obtained parameters by the model fits are displayed in table B.1.

The obtained volume fractions ϕ are in good agreement with the nominal values for all volume fractions.

For the smaller volume fractions $\phi < 0.02$ the extracted salt concentrations are in good agreement with the nominal salt values. For the samples at higher volume fractions $\phi > 0.06$, the salt concentrations obtained by the RMSA model show discrepancies to the nominal concentrations of monovalent salt ions. While the fits display the overall feature of an increasing salt concentration in all of the three concentration series, the absolute values differ. While the model overestimates the electrolyte concentration at small nominal salt concentrations, it underestimates the salt concentration at high nominal concentrations of added electrolyte ($> 500\,\mu$M).

Table B.1.: System, nominal salt concentration, nominal volume fraction ϕ_{nom}, position Q_{max} and height of the peak of the static structure factor $S(Q_{max})$ and parameters yielded by a fit of the RMSA model to the static structure factors $S(Q)$. Model parameters were the temperature $T = 293.15\,\text{K}$ and the dielectric permittivity of the dispersion medium $\epsilon_r = 80.1$. For system PMMA$_{542}$ the mean radius of the particles was $R_0 = 542\,\text{Å}$ and the effective charge $Z_{\text{eff}} = 496\,\text{e}^-$, for system PMMA$_{1117}$ the mean radius of the particles was $R_0 = 1117\,\text{Å}$ and the effective charge $Z_{\text{eff}} = 221\,\text{e}^-$.

System	ϕ_{nom}	Salt$_{\text{nom}}$ [μM]	Q$_{\text{max}}$ [Å^{-1}]	S(Q$_{\text{max}}$)	ϕ	Salt [μM]
PMMA$_{542}$	0.001	0	0.0009	1.35	0.0010	4.1
PMMA$_{542}$	0.001	10	0.0012	1.06	0.0009	18.6
PMMA$_{542}$	0.002	0	0.0011	2.09	0.0027	2.4
PMMA$_{542}$	0.002	10	0.0011	1.26	0.0021	10.6
PMMA$_{542}$	0.002	50	0.0015	1.05	0.0016	40.6
PMMA$_{542}$	0.002	100	0.0019	1.03	0.0019	78.7
PMMA$_{542}$	0.004	5	0.0014	1.89	0.0052	6.3
PMMA$_{542}$	0.004	10	0.0016	1.31	0.0049	18.9
PMMA$_{542}$	0.004	50	0.0017	1.08	0.0031	45.7
PMMA$_{542}$	0.008	5	0.0017	2.31	0.0089	5.2
PMMA$_{542}$	0.008	10	0.0018	2.11	0.0115	10.0
PMMA$_{542}$	0.008	20	0.0017	1.52	0.0084	19.5
PMMA$_{542}$	0.008	50	0.0017	1.16	0.0055	39.3
PMMA$_{542}$	0.012	10	0.0019	2.69	0.0137	4.7
PMMA$_{542}$	0.012	20	0.0018	1.76	0.0107	16.4
PMMA$_{542}$	0.012	50	0.0021	1.26	0.0118	54.4
PMMA$_{1117}$	0.08	0	0.00213	1.28	0.113	89
PMMA$_{1117}$	0.08	50	0.00236	1.10	0.078	343
PMMA$_{1117}$	0.08	200	0.00236	1.09	0.075	332
PMMA$_{1117}$	0.08	500	0.00236	1.10	0.081	356
PMMA$_{1117}$	0.08	2000	0.00252	1.09	0.094	617
PMMA$_{1117}$	0.08	5000	0.00263	1.09	0.090	1400
PMMA$_{1117}$	0.16	0	0.00244	1.32	0.174	202
PMMA$_{1117}$	0.16	10	0.00244	1.30	0.163	185
PMMA$_{1117}$	0.16	35	0.00244	1.29	0.161	180
PMMA$_{1117}$	0.16	100	0.00244	1.29	0.163	207
PMMA$_{1117}$	0.16	500	0.00244	1.29	0.165	213
PMMA$_{1117}$	0.16	1000	0.00248	1.26	0.164	301
PMMA$_{1117}$	0.16	2000	0.00248	1.25	0.162	313
PMMA$_{1117}$	0.16	3500	0.00255	1.17	0.144	457
PMMA$_{1117}$	0.16	5000	0.00255	1.16	0.141	555
PMMA$_{1117}$	0.33	100	0.00276	2.89	0.376	19
PMMA$_{1117}$	0.33	200	0.00280	2.57	0.376	62
PMMA$_{1117}$	0.33	350	0.00280	2.15	0.356	143
PMMA$_{1117}$	0.33	3500	0.00280	1.70	0.324	399
PMMA$_{1117}$	0.33	5000	0.00280	1.50	0.326	354
PMMA$_{1117}$	0.33	10000	0.00280	1.40	0.285	1030

List of Figures

List of Tables

Bibliography

Abernathy, D., Grübel, G., Brauer, S., McNulty, I., Stephenson, G., Mochrie, S., Sandy, A., Mulders, N. and Sutton, M. (1998). Small-angle x-ray scattering using coherent undulator radiation at the esrf. *Journal of Synchrotron Radiation*, **5** (1), 37–47.

Ackerson, B. and Clark, N. (1981). Dynamic light-scattering at low rates of shear. *Journal de physique*, **42** (7), 929–936.

Als-Nielsen, J. and McMorrows, D. (2001). *Elements of Modern X-ray Physics*. John Wiley and Sons, New Jersey.

Ashcroft, N.W. and Lekner, J. (1966). Structure and resistivity of liquid metals. *Phys. Rev.*, **145** (1), 83–90.

Banchio, A.J., McPhie, M.G. and Nägele, G. (2008). Hydrodynamic and electrokinetic effects on the dynamics of charged colloids and macromolecules. *Journal of Physics-Condensed Matter*, **20** (40), 404213.

Banchio, A., Gapinski, J., Patkowski, A., Haussler, W., Fluerasu, A., Sacanna, S., Holmqvist, P., Meier, G., Lettinga, M. and Nägele, G. (2006). Many-body hydrodynamic interactions in charge-stabilized suspensions. *Physical Review Letters*, **96** (13), 138303.

Banchio, A., Nägele, G. and Bergenholtz, J. (1999). Viscoelasticity and generalized stokes-einstein relations of colloidal dispersions. *Journal of Chemical Physics*, **111** (18), 8721–8740.

Beenakker, C.W.J. and Mazur, P. (1983). Self-diffusion of spheres in a concentrated suspension. *Physica A: Statistical and Theoretical Physics*, **120** (3), 388–410.

Beenakker, C.W.J. and Mazur, P. (1984). Diffusion of spheres in a concentrated suspension ii. *Physica A: Statistical and Theoretical Physics*, **126** (3), 349–370.

Beenakker, C. (1984). *On the transport Properties of Concentrated Suspensions*. Ph.D. thesis, Rijksuniversiteit te Leiden, Leiden.

Berne, B.J. and Pecora, R. (1976). *Dynamic Light Scattering*. Wiley, New York.

Brown, J.C., Pusey, P.N., Goodwin, J.W. and Ottewill, R.H. (1975). Light scattering study of dynamic and time-averaged correlations in dispersions of charged particles. *Journal of Physics A: Mathematical and General*, **8** (5), 664–682.

Busch, S., Jensen, T., Chushkin, Y. and Fluerasu, A. (2008). Dynamics in shear flow studied by x-ray photon correlation spectroscopy. *The European Physical Journal E: Soft Matter and Biological Physics*, **26** (1–2), 55–62.

Chatenay, D., Urbach, W., Messager, R. and Langevin, D. (1987). Self-diffusion of interacting micelles: Frapp study of micelles self-diffusion. *The Journal of Chemical Physics*, **86** (4), 2343–2351.

Cichocki, B. and Felderhof, B.U. (1988). Long-time self-diffusion coefficient and zero-frequency viscosity of dilute suspensions of spherical brownian particles. *The Journal of Chemical Physics*, **89** (6), 3705–3709.

Daguanno, B., Genz, U. and Klein, R. (1990). Structure and dynamics of colloidal systems. *Journal of physics - condensed matter*, **2** (Suppl. A), SA379–SA384.

De Gennes, P.G. (1959). Liquid dynamics and inelastic scattering of neutrons. *Physica*, **25** (7–12), 825–839.

Donev, A., Stillinger, F.H. and Torquato, S. (2005). Unexpected density fluctuations in jammed disordered sphere packings. *Phys. Rev. Lett.*, **95** (9), 090604.

Ermak, D.L. and McCammon, J.A. (1978). Brownian dynamics with hydrodynamic interactions. *The Journal of Chemical Physics*, **69** (4), 1352–1360.

Fijnaut, H.M., Pathmamanoharan, C., Nieuwenhuis, E.A. and Vrij, A. (1978). Dynamic light scattering from concentrated colloidal dispersions. *Chemical Physics Letters*, **59** (2), 351–355.

Gapinski, J., Patkowski, A., Banchio, A.J., Buitenhuis, J., Holmqvist, P., Lettinga, M.P., Meier, G. and Nägele, G. (2009). Structure and short-time dynamics in suspensions of charged silica spheres in the entire fluid regime. *The Journal of Chemical Physics*, **130** (8), 084503.

Gapinski, J., Patkowski, A., Banchio, A.J., Holmqvist, P., Meier, G., Lettinga, M.P. and Nägele, G. (2007). Collective diffusion in charge-stabilized suspensions: Concentration and salt effects. *Journal of Chemical Physics*, **126** (10), 104905.

Gapinski, J., Patkowski, A. and Nägele, G. (2010). Generic behavior of the hydrodynamic function of charged colloidal suspensions. *The Journal of Chemical Physics*, **132** (5), 054510.

de Gennes, P.G. (1979). *Scaling Concepts in Polymer Physics*. Cornell University Press, Cornell.

Grübel, G., Abernathy, D.L., Riese, D.O., Vos, W.L. and Wegdam, G.H. (2000). Dynamics of dense, charge-stabilized suspensions of colloidal silica studied by correlation spectroscopy with coherent x-rays. *Journal of Applied Crystallography*, **33** (3-1), 424–427.

Grübel, G., Als-Nielsen, J. and Freund, A. (1994). The troika beamline at esrf. *Journal de Physique IV*, **4** (C9), 27–34.

Hansen, J. and Hayter, J. (1982). A rescaled msa structure factor for dilute charged colloidal dispersions. *Molecular Physics*, **46** (3), 651–656.

Härtl, W., Beck, C. and Hempelmann, R. (1999). Determination of hydrodynamic properties in highly charged colloidal systems using static and dynamic light scattering. *Journal of Chemical Physics*, **110** (14), 7070–7072.

Härtl, W. and Zhang-Heider, X. (1997). The synthesis of a new class of polymer colloids with a low index of refraction. *Journal of Colloid and Interface Science*, **185** (2), 398–401.

Hayter, J. and Penfold, J. (1981). An analaytic structure factor for macroion solutions. *Molecular Physics*, **42** (1), 109–118.

Hergeth, W., Lebek, W., Stettin, E., Witkowski, K. and Schmutzler, K. (1992). Particle formation in emulsion polymerization. 2. aggregation of primary particles. *Makromelekulare Chemie-Macromelecular Chemistry and Physics*, **193** (7), 1607–1621.

Hoover, W.G. and Ree, F.H. (1968). Melting transition and communal entropy for hard spheres. *The Journal of Chemical Physics*, **49** (8), 3609–3617.

Horn, F., Richtering, W., Bergenholtz, J., Willenbacher, N. and Wagner, N. (2000). Hydrodynamic and colloidal interactions in concentrated charge-stabilized polymer dispersions. *Journal of Colloid and Interface Science*, **225** (1), 166–178.

Hückel, E. (1925). Zur theorie konzentrierter wässeriger lösungen starker elektrolyte. *Phys. Z.*, **26**, 93–204.

van de Hulst, H.C. (1981). *Light Scattering by Small Particles.* Dover, New York.

Kirkwood, J.G. and Buff, F.P. (1951). The statistical mechanical theory of solutions. i. *The Journal of Chemical Physics*, **19** (6), 774–777.

van Megen, W., Ottewill, R., Owens, S. and Pusey, P.N. (1985). Measurement of the wave-vector dependent diffusion coefficient in concentrated particle dispersions. *The Journal of Chemical Physics*, **82** (1), 508–515.

Nägele, G. and Baur, P. (1997). Long-time dynamics of charged colloidal suspensions: hydrodynamic interaction effects. *Physica A: Statistical and Theoretical Physics*, **245** (3–4), 297–336.

Nägele, G., Kellerbauer, O., Krause, R. and Klein, R. (1993). Hydrodynamic effects in polydisperse charged colloidal suspensions at short times. *Phys. Rev. E*, **47** (4), 2562–2574.

Nägele, G. (1996). On the dynamics and structure of charge-stabilized suspensions. *Physics Reports*, **272** (5-6), 215–372.

Nägele, G., Steininger, B., Genz, U. and Klein, R. (1994). Short-time dynamics of charge-stabilized colloidal suspensions. *Physica Scripta*, **T55** (T55), 119–126.

Narayanan, T., Cheung, C., Tong, P., Goldburg, W.I. and lun Wu, X. (1997). Measurement of the velocity difference by photon correlation spectroscopy: an improved scheme. *Appl. Opt.*, **36** (30), 7639–7644.

Pecora, R. (2000). Dynamic light scattering measurement of nanometer particles in liquids. *Journal of Nanoparticle Research*, **2**, 123–131.

Percus, J.K. and Yevick, G.J. (1958). Analysis of classical statistical mechanics by means of collective coordinates. *Phys. Rev.*, **110** (1), 1–13.

Philipse, A.P. and Vrij, A. (1988). Determination of static and dynamic interactions between monodisperse, charged silica spheres in an optically matching, organic solvent. *The Journal of Chemical Physics*, **88** (10), 6459–6470.

Priest, W. (1952). Particle growth in the aqueous polymerization of vinyl acetate. *Journal of Physical Chemistry*, **56** (9), 1077–1082.

Pusey, P.N. (1991). *Liquids, Freezing and Glass transition*, chap. Colloidal suspensions, 764–942. Elsevier Science, Amsterdam.

Pusey, P.N. and van Megen, W. (1986). Phase behaviour of concentrated suspensions of nearly hard colloidal spheres. *Nature*, **320** (6060), 340–342.

Riese, D.O. (2000). *Fluid Dynamics in Charge Stabilized Colloidal Suspensions*. Ph.D. thesis, Universiteit van Amsterdam, Amsterdam.

Riese, D.O., Vos, W.L., Wegdam, G.H., Poelwijk, F.J., Abernathy, D.L. and Grübel, G. (2000a). Photon correlation spectroscopy: X rays versus visible light. *Phys. Rev. E*, **61** (2), 1676–1680.

Riese, D.O., Wegdam, G.H., Vos, W.L., Sprik, R., Fenistein, D., Bongaerts, J.H.H. and Grübel, G. (2000b). Effective screening of hydrodynamic interactions in charged colloidal suspensions. *Phys. Rev. Lett.*, **85** (25), 5460–5463.

Robbins, M.O., Kremer, K. and Grest, G.S. (1988). Phase diagram and dynamics of yukawa systems. *The Journal of Chemical Physics*, **88** (5), 3286–3312.

Robert, A., Wagner, J., Härtl, W., Autenrieth, T. and Grübel, G. (2008). Dynamics in dense suspensions of charge-stabilized colloidal particles. *The European Physical Journal E: Soft Matter and Biological Physics*, **25** (1), 77–81.

Schätzel, K. (1991). Suppression of multiple scattering by photon cross-correlation techniques. *Journal of Modern Optics*, **38** (9), 1849–1865.

Segrè, P.N., Behrend, O.P. and Pusey, P.N. (1995). Short-time brownian motion in colloidal suspensions: Experiment and simulation. *Phys. Rev. E*, **52** (5), 5070–5083.

Snook, I., van Megen, W. and Tough, R. (1983). Diffusion in concentrated hard-sphere dispersions - effective 2 particle mobiliy tensors. *Journal of Chemical Physics*, **78** (9), 5825–5836.

Thickett, S.C. and Gilbert, R.G. (2007). Emulsion polymerization: State of the art in kinetics and mechanisms. *Polymer*, **48** (24), 6965–6991.

Tirado-Miranda, M., Haro-Perez, C., Quesada-Perez, M., Callejas-Fernandez, J. and Hidalgo-Alvarez, R. (2003). Effective charges of colloidal particles obtained from collective diffusion experiments. *Journal of Colloid and Interface Science*, **263** (1), 74–79.

Urban, C. (1999). *Development of Fiber Optic Based Dynamic Light Scattering for a Characterization of Turbid Suspensions*. Ph.D. thesis, Swiss Federal Institute of Technology Zürich.

Urban, C. and Schurtenberger, P. (1998). Characterization of turbid colloidal suspensions using light scattering techniques combined with cross-correlation methods. *Journal of Colloid and Interface Science*, **207** (1), 150—-158.

Verwey, E. and Overbeek, J. (1948). *Theory of the Stability of Lyophobic Colloids*. Elsevier, Amsterdam.

William G. McMillan, J. and Mayer, J.E. (1945). The statistical thermodynamics of multicomponent systems. *The Journal of Chemical Physics*, **13** (7), 276–305.

Wochner, P., Gutt, C., Autenrieth, T., Demmer, T., Bugaev, V., Ortiz, A.D., Duri, A., Zontone, F., Grübel, G. and Dosch, H. (2009). X-ray cross correlation analysis uncovers hidden local symmetries in disordered matter. *Proceedings of the National Acadamy of Sciences of the United States of America*, **106** (28), 11511–11514.

Acknowledgements

One of the real pleasures writing this thesis is the opportunity to thank all the people who have supported, advised and encouraged me during the last years - of course all of this work would never have been possible without their help.

First and foremost I would like to thank my supervisors Dr. Gerhard Grübel and Prof Dr. Wilfried Wurth. I am indebted and thankful to them for offering me the opportunity to work with them on this project. I especially would like to thank Dr. Gerhard Grübel to welcome me in his group, for his encouragement and expertise throughout the whole time of my thesis. I am especially thankful that he always took his time for me - for questions, discussions, encouragement and guidance throughout the whole time I spent here at Hasylab. I would also like to express my gratitude to Prof Dr. Wilfried Wurth for his supervision, and the possibility to discuss this project with him. I also would like to thank Prof. Dr. Gerhard Nägele for taking the time to act as a second referee for my thesis.

I am in great debt to Tina Autenrieth, who introduced my into the synthesis of colloidal systems and took care of my first steps into the world of X-rays. After she left, Birgit Fischer managed to fill the hole - thank you both for your impressive help, your encouragement and the invaluable advice I got from you especially for the chemistry related parts of my thesis.

I benefitted a lot of working together with all the people of the *Scattering with coherent X-rays* group: Olaf Leupold, who always took the time to explain any question and his amazing support and advice during various beamtimes. Christian Gutt, to whom I could always address any problem and question that occurred during my work, especially about anything concerning coherent scattering. Michael Sprung, who not only aided me during my experiments, but who also was a great help for the analysis of dynamics recorded in 2D. Wojtek Roseker, Heiko Conrad, Agnès Duri, Louisa Dahbi and Alexander Kadenkin, who helped me during various beamtimes. Leonard Müller, whose help and advice especially for any LaTeX related question was invaluable and my former office mates Simone Streit-Nierobisch and Kyu Hyun, who always had time for any question or coffee break.

I would especially like to thank Bernd Struth for his ideas, his encouragement and motivation and the possibility to learn from him during numerous beamtimes. Of course, I would also like to thank Thomas Pfohl and Eric Stellamanns for the warm welcome in Göttingen and the introduction into microfluidic devices.

I am greatly indebted to the whole crew of the Troïka beamline at the ESRF. A special thanks of course to Anders Madsen, who offered me the opportunity to spend four months in his group. In addition I would like to thank Yuriy Chushkin, Chiara

Caronna, Lutz Wiegart, Andrei Fluerasu and Federico Zontone, who welcomed me heartly and made my stay in Grenoble a memorable time. I am also indebted to Patrick Feder and Karim Lhoste for their fast technical help concerning the sample environment.

I would like to express my gratitude to Heiko Schulz-Ritter, who supported my in designing a flow through set-up, Milenko Prodan for his help in designing a modified sample environment and Jens Brehling and the whole Hasylab work shop for their help in finding easy solutions and their constructions.

Another big "thank you" for Klaudia Hagemann and Manfred Spiwek for their support around anything concerning missing chemicals or lab equipment. And of course to Karolin Darame, Christine Berber and especially to Sylke Strien, who revealed how fast and unproblematic a travel reimbursement can be.

My whole time here at Hasylab would not have been such a great experience without the wonderful atmosphere - and apart from the already mentioned I would like to especially thank Kai Schlage, Sebastien Couet, Bente Walz, Martin Tolkiehn, Sebastian Thieß, Torsten Laurus, Ulla Vainio, Matthias Kreuzeder, Torben Fischer, Antje Hansen and Lorenz Stadler - and everybody else who made my time here a memorable one.

Finally I would like to thank my family – Annemie and Franz, Monika, Regina, Päule and Gerd, Stefanie and Christoph, Anne, Hilde and my grandparents, for all their love and support during the last years – and of course Katja for her love and understanding especially during the last time-consuming weeks of finishing this work.